

Conceptual Design and Setup of a Fully Digital Recording Apparatus for the Application in Perturbed Angular Correlation Spectroscopy

Von der Fakultät für Lebenswissenschaften
der Technischen Universität Carolo-Wilhelmina
zu Braunschweig
zur Erlangung des Grades eines
Doktors der Naturwissenschaften
(Dr. rer. nat.)
genehmigte
D i s s e r t a t i o n

von Christian H. O. Herden
aus Ibbenbüren

1. Referentin oder Referent: Professor Dr. Klaus Dieter Becker
2. Referentin oder Referent: Professor Dr. Fred Jochen Litterst
eingereicht am: 12.12.2007
mündliche Prüfung (Disputation) am: 29.02.2008
Druckjahr 2008

Vorveröffentlichungen der Dissertation

Teilergebnisse aus dieser Arbeit wurden mit Genehmigung der Fakultät für Lebenswissenschaften, vertreten durch den Mentor/der Mentorin der Arbeit, in folgenden Beiträgen vorab veröffentlicht:

Publikationen

Jens Röder, Christian H. Herden, John. A. Gardner, and Klaus. D. Becker, “Fully Digital Time Differential Perturbed Angular Correlation (TDPAC) Spectrometer”, eingereicht 2007 an *Nuclear Instruments and Methods Section A* NIMA-S-07-00089.

Christian H. Herden, Mauro A. Alves, Klaus D. Becker, and John A. Gardner, “A New Generation TDPAC Spectrometer”, *Hyperfine Interactions* **159**(1-4) (2004): 379-383

Tagungsbeiträge

Christian H. Herden, Mauro A. Alves, Klaus D. Becker, and John A. Gardner, “A New Generation TDPAC Spectrometer”, (Poster), XIII. International Conference on Hyperfine Interactions & XVII International Symposium on Nuclear Quadrupole Interactions, Bonn, 23.-27. August 2004.

Jens Röder, Christian H. Herden, John A. Gardner, Klaus D. Becker, Micheal Uhrmacher, and Hans Hofsäss, “Actual Concepts of Digital PAC Spectroscopy”, (Poster), XIV. International Conference on Hyperfine Interactions & XVIII International Symposium on Nuclear Quadrupole Interactions, Cataratas del Iguazu, 5.-7. August 2007.

Abstract

Perturbed Angular Correlation spectroscopy is a hyperfine interaction method that gathers information regarding the environment of a radioactive probe. The method is based on the measurement of the anisotropic correlation between directions of emissions of two gamma rays during the decay of the radioactive nuclei. It utilizes the information collected by photomultiplier tubes which are placed around the sample. The life times of the intermediate nuclear states are in general very short. Therefore, the detection system is bound to observe coinciding occurrences preferably within fractions of a nanoseconds. In order to support the Perturbed Angular Correlation methods need for Time-of-arrival detection and energy discrimination a versatile system was built using Digital Signal Processing equipment. Each channel uses its own programmable signal processing board in an off-the-shelf computing unit. The peer design of the system allows the expansion to basically any number of channels. The photomultipliers output signal are being processed digitally and the energy and the Time-of-arrival information are placed on a storage medium for later evaluation. This fully digital recording system holds an average time resolution of about 400 picoseconds, thanks to the high-speed acquisition boards that are being utilized in this design. The new system provides advantages with respect to sample handling and spectrometer calibration with respect to conventional setups. It competes also well in performance and many experimental difficulties related to electronics have been eliminated. The spectrometers acquisition cycles are being controlled by software applications allowing a wide range of flexibility in an easy reconfigurable system.

Acknowledgements

I wish to take this opportunity to thank all the people who supported me in my work and foremost inspired me with their ideas and knowledge.

First of all I would like to thank Prof. Dr. John A. Gardner for leading me onto the path to PAC spectroscopy in the field of solid state physics and nuclear science. Also, for sharing his thoughts with me and being a steady source for terrific ideas, and not at last for reviewing my thesis towards the end.

Further I would like to thank Prof. Dr. Klaus D. Becker for giving me the opportunity to use my work on PAC spectroscopy as a subject for my doctoral dissertation, for the provision of lab space and equipment supporting my efforts at all times, and for enabling me to continue to work on the PAC project even from a remote distance.

Then I also would like to express my acknowledgements to the following people I worked with during the last couple of years.

Dipl.-Chem. Jens Röder for his engagement in this project and his help in promoting the work in Braunschweig even without my presence. For sharing his knowledge in chemistry science and being a resourceful partner in technical conversations. I appreciated the vivid discussions about security issues in modern information technology and conspiracy theories.

Dr. Mauro A. Alves for sharing his thoughts about PAC theory with me, performing some of the original PAC measurements with the new spectrometer setup, and for preparing and printing the conference materials.

Dr. Roland Platzer for introducing me to John Gardner in the first place, and also for his input and assistance on the issues regarding photomultiplier tubes.

Dr. Robert L. Rasera for discussing the issues about data reduction methods used in PAC spectroscopy, and suggestions for publishers.

Dr. Matthew O. Zacate for the preparation of the Tin sample and discussing the results.

Dr. Ken S. Krane for supplying the activated Hafnium sample.

I also acknowledge the DFG for financially supporting this work under the grant application SPP 1136 “Substitutionseffekte in ionischen Festkörpern”.

Finally, I want to thank my wife Gaby for her encouragement and support during the creation of this thesis, and for that she has endured her husband being in front of a computer screen many times. Thanks to my children Lara and Luke, which have bore a sometimes inadvertently behaving father during the first five months of their lives, my cousin Nehle for letting me stay at her apartment during my visits in Braunschweig, and my parents, family and friends for being so “challenging and teasing” about my profession.

Contents

1	Introduction	1
2	PAC theory	5
2.1	Theory of Angular Correlation	5
2.2	Perturbation of Angular Correlation	12
2.3	Absence of Perturbation	15
2.4	Polycrystalline Samples	16
2.5	Static Electric Quadrupole Interaction	18
2.6	Static Magnetic Dipole Interaction	26
3	Hardware	29
3.1	Overview of Setup and Operation	29
3.2	Handshake Bus	32
3.3	Standard parallel port	32
3.4	Digital Signal Processing Boards	33
3.4.1	Scope settings	36
3.5	Host computer	37
3.6	Slave computers	38
3.7	Analog multiplexer module	38
3.8	Reference clock distributor	39
3.9	Synchronization and Channel Select fanout module	40
3.10	Photomultipliers	40
4	Software	43
4.1	Parallel port device driver	43
4.1.1	Installing the device driver	43
4.1.2	Using the device driver from the console	44
4.1.3	Using the device driver in a C/C++ application	44
4.2	Slave applications	45
4.2.1	Pacslave	45
4.2.2	Pacslave options	50
4.2.3	Pacslave file format	50
4.3	Host applications	51
4.3.1	Pachost	51

4.3.2	Cocheck	53
4.3.3	Cocheck file format	55
4.4	Network File System	56
5	Experiments	57
5.1	Host and Slave Preparation	57
5.2	Data Processing	57
5.3	Timing Tests	63
5.4	PAC Sample Preparation	68
6	Results	71
6.1	Performance	71
6.2	PAC measurements	75
6.2.1	Sample <i>a.</i>) $^{111}\text{In}(\text{Cd})$ in $\beta\text{-Sn}$ metal	76
6.2.2	Sample <i>b.</i>) $^{111}\text{In}(\text{Cd})$ in Cadmium Silicon Phosphide	78
6.2.3	Sample <i>c.</i>) $^{111}\text{In}(\text{Cd})$ in Iron foil	80
6.2.4	Sample <i>d.</i>) $^{181}\text{Hf}(\text{Ta})$ in Hafnium metal	81
6.3	Detector Start-Stop Efficiencies	83
7	Conclusion	85
A	Appendix	87
A.1	Parallel port pin assignment	87
A.2	Parallel port I/O registers	88
A.3	Schematic diagrams	89
A.3.1	Wiring Plan	89
A.3.2	Analog Multiplexer Module	89
A.3.3	Synchronization and Channel Select Module	89
A.3.4	Reference clock module	89
A.4	Configuration files and Command line options	94
A.4.1	Pacslave	94
A.4.2	Pacslave.conf	97
A.4.3	Pachost	99
A.4.4	Pachost.conf	101
A.4.5	Cocheck	102
A.4.6	Cocheck.conf	104

References	105
Lebenslauf	109

List of Figures

1	Illustrations of angular anisotropy characteristics	8
2	Energy scheme for $I = 5/2$ intermediate state	27
3	Functional block diagram	31
4	Handshake bus timing diagram	33
5	Subsequent segments in memory	35
6	Block diagram of multiplexer circuit	39
7	Single transient pulse	41
8	Illustration of the CFD technique applied on transient waveform . . .	48
9	Time deviation results with CFD	49
10	Flow chart for PAC processes <i>Pachost</i> and <i>Pacslave</i>	52
11	Energy resolution of PMT detectors	55
12	Time spectrum of a detector pair	59
13	Conventional Start-Stop detector arrangements	60
14	Effective anisotropy $A_{22,eff}$ with respect to detector distance	64
15	Chronological resolution displayed in prompt peaks	65
16	Time deviation between six channel pairs	68
17	Sample activity over 456 hour experiment	72
18	Duty cycle with respect to sample activity	74
19	$A_{22,eff}G_{22}(t)$ for $^{111}\text{In}(\text{Cd})$ in β -Sn metal	77
20	$A_{22,eff}G_{22}(t)$ for $^{111}\text{In}(\text{Cd})$ in CdSiP_2	79
21	$A_{22,eff}G_{22}(t)$ for $^{111}\text{In}(\text{Cd})$ in α -iron metal	81
22	$A_{22,eff}G_{22}(t)$ for $^{181}\text{Hf}(\text{Ta})$ in Hf metal	82

List of Tables

1	Characteristics of isotope $^{111}\text{In}(\text{Cd})$	9
2	Characteristics of isotope $^{181}\text{Hf}(\text{Ta})$	10
3	List of command declarations in <i>pacmod</i>	46
4	<i>Pacslave</i> 's default settings	58
5	Parametric time deviation	67
6	Results for $^{111}\text{In}(\text{Cd})$ in Fe experiment	75
7	Pin assignment of the D-Type 25 pin standard parallel port connector.	87
8	SPP I/O register assignment	88

1 Introduction

Perturbed Angular Correlation spectroscopy (PAC) is one of the many hyperfine methods used in nuclear solid state physics research, and supplements methods such as Mössbauer spectroscopy and Nuclear Magnetic Resonance. They are all based on the interaction between the spin momentum of specific nuclei and electric and magnetic hyperfine fields caused by the condition of the immediate neighborhood. Such fields can be produced by the existence of valence electrons, electrons in the conduction band, and other defects caused by vacancies and dopants. PAC is used mainly in the research of solid state materials as a tool with high sensitivity to characterize local host properties, and thus relatively low numbers of radioactive probe atoms are necessary.

Conventional PAC equipment that is necessary to accomplish the detection of correlated events that are for the most only nano seconds apart is usually very complex and the setup is very time consuming. A PAC instrument is often tuned to accommodate experiments that use a specific isotope, to which the timing resolution and the energy window settings were calibrated before. Isotope exchanges are virtually not possible without recalibrating the whole instrument. Further, the tremendous amount of electronic circuits necessary for operation also limits the deployment of recording channels. So far it was not possible to add an arbitrary number of recording channels to conventional PAC instruments without gaining complexity in the electronics by orders of magnitude.

In conventional PAC spectrometers Time-to-Amplitude Converters measure the time interval between pulses to their start and stop inputs and generate an analog output pulse proportional to the measured time. This analog pulse is then converted into digital form so that a computer is able to process the information. One negative aspect of this quasi analog timing system is the requirement of timing calibration. Prudent adjustments are necessary that relate pulse height to timing resolution. Otherwise the acquisition would simply operate out of bounds and deliver unsatisfactory results. As a result, due to the large amount of maintainance that is needed to keep the PAC system going, only a limited group of scientists world wide are deploying this method in research labs. And for these reasons PAC spectroscopy is not as commonly used as other nuclear research methods.

The main objective of this work is to present a versatile time-of-flight acquisition system that enables its application in time-differential PAC (TDPAC), perturbed an-

gular distribution (PAD), and possibly positron annihilation spectroscopy (PAS). In principle, all of the named methods have the same requirements on the data collection equipment. This work presents the realization of a multi-channel acquisition system with the help of off-the-shelf, state-of-the-art, programmable fast Digital Signal Processing boards. Each channel utilizes its own DSP board mounted in a dedicated Personal Computer. The peer design of the electronic system allows the addition of any number of channels. The benefit of having a larger number of detectors is clearly the increment of statistical information and, in addition, shorter measuring times. This enhances the subsequent use of short-lived isotopes.

A simple electronic handshake bus is linked to each channel and the main controlling unit. As a very cost-effective solution, the relatively few handshake logic lines were established through the in- and output pins of the Standard Parallel Port that every PC mainboard is equipped with. While the hardware complexity and costs were kept to a minimum, the system on the other hand required the development of a vast amount of software applications. During the course of the development a framework was created that combines all vital applications and drivers. Among them are the low-level device driver *pacmod.o* and the manufacturer supplied driver *acqrs1.o* supporting the handshake bus and the digitizer hardware. The high-level applications such as *Pacslave*, *Pachost* were instantiated as part of the real-time inter-process acquisition framework. For a N -detector instrument there is one instance of *Pacslave* processes running on each of the N slave computers behind each detector. The main controlling process *Pachost* is running on the main host computer and is monitoring each one of the slave computers. All processes are connected through the fast handshake bus and the Ethernet network switch. The helper application *Cocheck* was developed for coincidence filtering and first-stage data reduction purposes. Filters for energy selection are applied also in this instance. These filters are customizable in configuration files at any time. All applications were written in plain C/C++ under the objective of portability to other systems.

A number of test measurements were performed to verify the proper operation of this new time-of-flight acquisition system. Some questions, that need to be answered are whether the new apparatus's timing resolution will be sufficient for short-lived intermediate states ($\tau_{\frac{1}{2}} \leq 10$ ns), and if the new system will at least reach the performance of conventional PAC spectrometers. Reset times in traditional Time-to-Amplitude Converters are typically between $1\ \mu\text{s}$ and $50\ \mu\text{s}$, which limits the detection of repetitive signals in the worst case to 25 kHz [27], [28]. The timing tests on the new PAC

setup will also show the achievable quality of the apparatus's timing resolution. These general test measurements were succeeded by real PAC measurements on compounds that have been studied previously. Their properties are well-known and understood. The isotopes $^{111}\text{In}(\text{Cd})$ and $^{181}\text{Hf}(\text{Ta})$ are the most popular radioactive probe atoms used in PAC spectroscopy, and therefore, a vast number of publications about compounds with these isotopes are available. The PAC samples were prepared according to the published methods to insure the repeatability of the previous results. The samples were picked under the aspect of that ease to identify spectra. If the acquisition system would not perform as expected the data would show evidence of misbehaviour immediately. For instance, attenuation effects can often be attributed to the acquisition systems limited timing resolution. If a spectrum taken with this new PAC spectrometer shows attenuation on a sample from which is known that damping effects do not exist, then it must be assumed that the apparatus does not work accordingly.

Measurements were performed on metallic alloys and insulators with $^{111}\text{In}(\text{Cd})$ and $^{181}\text{Hf}(\text{Ta})$ impurities. Non-cubic metals provide the most suitable environment for the observation of a quadrupole interaction. The reservoir of conduction electrons in the metal brings the recoil atom, produced by the nuclear reaction, quickly into its equilibrium charge state. A second advantage of metals over insulators is the tendency of the former to form alloys with impurities such that the impurity atom occupies a substitutional site in the lattice. The metal samples in this work were in the state of solid pieces. Impurities were introduced through melting and subsequent quenching, or ion implantation.

The metal samples investigated were $^{111}\text{In}(\text{Cd})$ in $\alpha\text{-Fe}$, $^{111}\text{In}(\text{Cd})$ in $\beta\text{-Sn}$, and $^{181}\text{Hf}(\text{Ta})$ in Hf metal. In the cubic *fcc* structure of $\alpha\text{-Fe}$ the electric field gradient is zero. In ferromagnetic materials, however, non-random Weiss domains produce intrinsic permanent magnetic fields at room temperature that produce a magnetic dipole interaction with the nucleus.

For the two non-cubic metal alloys $\beta\text{-Sn}$ and Hf the interaction with the nucleus is known to be of quadrupole nature. The quadrupole interaction is characterized solely by the strength of the third component V_{zz} of the electric field gradient tensor and the asymmetry parameter η . The lattice environment in both metal alloys produces an electric field gradient component V_{zz} that is non-zero. The asymmetry parameters can vary between $0 \leq \eta \leq 1$. For the above cases the magnetic domains and the domains with quadrupole interaction are assumed to be oriented randomly within the sample,

and therefore the perturbation function $W(\theta, t)$ can be treated with the approximation for polycrystalline samples. Due to possible non-random texture effects, however, hardcore parameters may not reflect their theoretical predicted values.

Additional measurements were performed on $^{111}\text{In}(\text{Cd})$ in CdSiP_2 , a semiconductor with chalcopyrite structure. The environment of the $^{111}\text{In}(\text{Cd})$ on substitutional Cd sites produces a symmetric electric field gradient ($V_{zz} \neq 0, \eta = 0$) at room temperature. Unlike the above-mentioned metal alloys, this sample in the state of tiny grains, represents a perfect polycrystalline sample. The hardcore parameters are expected to reflect the values predicted by the theory.

2 Introduction to Perturbed Angular Correlation Spectroscopy

2.1 Theory of Angular Correlation

Radiations from an atomic or nuclear system are not random in their directions. The method used in PAC spectroscopy works because a pattern in the decay of nuclear states over metastable to ground states can be observed. The nucleus decays from a single excited state $|I_i, M_i, \pi_i\rangle$ into the ground state $|I_f, M_f, \pi_f\rangle$. I , M and π are the quantum numbers of the quantum-mechanical states of the system. The decay process involves two successively occurring particles (γ_1, γ_2) denoted through the cascade $|I_i, M_i, \pi_i\rangle \xrightarrow{\gamma_1} |I, M, \pi\rangle \xrightarrow{\gamma_2} |I_f, M_f, \pi_f\rangle$. $|I, M, \pi\rangle$ is an intermediate level with a finite lifetime τ_N . In quantum-mechanical systems the characteristics of the levels are described by their well-defined angular momentum \vec{I} and parity π . Transitions are treated as changes in quantum numbers (l_1, m_1, π_1) for γ_1 and (l_2, m_2, π_2) for γ_2 . In this work only those transitions which result in the emission of γ radiation are of interest. During a transition from a higher state into lower state typically γ radiation is emitted with respect to the conservation of momentum and energy. Therefore the emitted γ radiation is classified according to the changes in nuclear parity and angular momentum. The parities $\pi_{1,2}$ of the γ -rays are related to the level parities by

$$\pi = \pi_i \pi_1 \quad , \quad \pi_f = \pi \pi_2. \quad (1)$$

The angular momentums $l_{1,2}$ can have a range of values given by

$$|I_f - I| \leq l_1 \leq I_f + I \quad , \quad |I - I_i| \leq l_2 \leq I + I_i. \quad (2)$$

The γ radiation is classified in E(l)-radiation by $\pi = (-1)^l$ and M(l)-radiation by $\pi = (-1)^{l+1}$. For different orders of the multipolarities $l_{1,2} = 1, 2, 3, \dots$ the lower modes of radiation can be summarized as

Parity change	$l = 1$	$l = 2$	$l = 3$...
yes	E(1)	M(2)	E(3)	...
no	M(1)	E(2)	M(3)	...

As an example we observe the decay scheme $\frac{7}{2}^+ \rightarrow \frac{5}{2}^+ \rightarrow \frac{1}{2}^+$ in $^{111}\text{In}(\text{Cd})$ as dis-

played in Table 1. For all transitions the parity never changes $\pi_1 = \pi_2 = 1$. The multipolarity order of the first transition is of order $l_1 = 1$ which accounts for pure dipole radiation character. In general $M(l+1)$ transitions versus $E(l)$ transitions can be neglected because transition probabilities are reduced by orders of magnitude [6]. Whereas $E(l+1)$ versus $M(l)$ are usually of comparable magnitude. Therefore the character for γ_1 in $^{111}\text{In}(\text{Cd})$ is predominantly $M(1)$, $E(2)$. The second transition of order $l_2 = 2$ has quadrupole character $E(2)$.

In the near vicinity around the nucleus the γ radiation is exposed to multipole fields. In the far-field a γ -ray's nature is an electromagnetic wave, and thus can be described by a set of coupled wave equations, which originate from a generalized vector potential \vec{A} that satisfy Maxwell's equations. The transverse electric and magnetic solutions of Maxwell's equations in regard to a general multipole vector potential can be expressed by [1]:

$$\begin{aligned} \vec{B}_l^m &= j_l(kr) \frac{1}{\sqrt{l(l+1)}} \vec{L} Y_l^m(\theta, \varphi) e^{-i\omega t}, & \vec{E}_l^m &= i \frac{c}{k} \vec{\nabla} \times \vec{B}_l^m, & (E) \\ \vec{E}_l^m &= j_l(kr) \frac{1}{\sqrt{l(l+1)}} \vec{L} Y_l^m(\theta, \varphi) e^{-i\omega t}, & \vec{B}_l^m &= -i \frac{1}{kc} \vec{\nabla} \times \vec{E}_l^m, & (M) \end{aligned} \quad (3)$$

where $j_l(kr)$ are spherical Bessel functions, $Y_l^m(\theta, \varphi)$ is the spherical harmonic function, and $\vec{L} = -i\hbar(\vec{r} \times \vec{\nabla})$ is the angular momentum operator. With help of the Maxwell solutions the angular distribution of the γ radiation can be calculated using the energy flux density, the Poynting-vector,

$$\vec{S} = \frac{1}{\mu_0} (\vec{E} \times \vec{B}). \quad (4)$$

\vec{E} and \vec{B} are perpendicular to each other and thus \vec{S} points into the direction of the γ radiation. In the far-field region the norm of the Poynting-vector follows from the Maxwell solutions (3) and (4)

$$|\vec{S}| = c\varepsilon_0 |\vec{E}|^2 = \frac{c}{\mu_0} |\vec{B}|^2 \propto |\vec{L} Y_l^m|^2. \quad (5)$$

The magnitude of the energy flux density, for both $E(l)$ - and $M(l)$ -radiation, is proportional to the expectation value of the spherical harmonic functions. Thus the radiation characteristic of the electro-magnetic wave is anisotropic with respect to θ

and φ . Therefore exists an angular correlation among the transitions which gives information about the nucleus. The spherical harmonic functions can be fully described in polar coordinates by the associated Legendre polynomials $P_l^m(\cos \theta)$, [9],

$$Y_l^m(\theta, \varphi) = (-)^m \sqrt{\frac{2l+1}{4\pi} \frac{(l-m)!}{(l+m)!}} P_l^m(\cos \theta) e^{im\varphi}, \quad (6)$$

The application of the angular momentum operator \vec{L} on the spherical harmonic functions Y_l^m addresses the various magnetic sublevels m for a specific spin state I . Multipole radiation originates from transitions between magnetic sublevels causing changes in angular momentum of a spin state. The expectation value is $|\vec{L}Y_l^m|^2$. The normalized angular distribution functions

$$F_{lm}(\theta) = \frac{|\vec{L}Y_l^m|^2}{\sum_m |\vec{L}Y_l^m|^2} \quad (7)$$

give a set of functions which are related to the radiation characteristics.

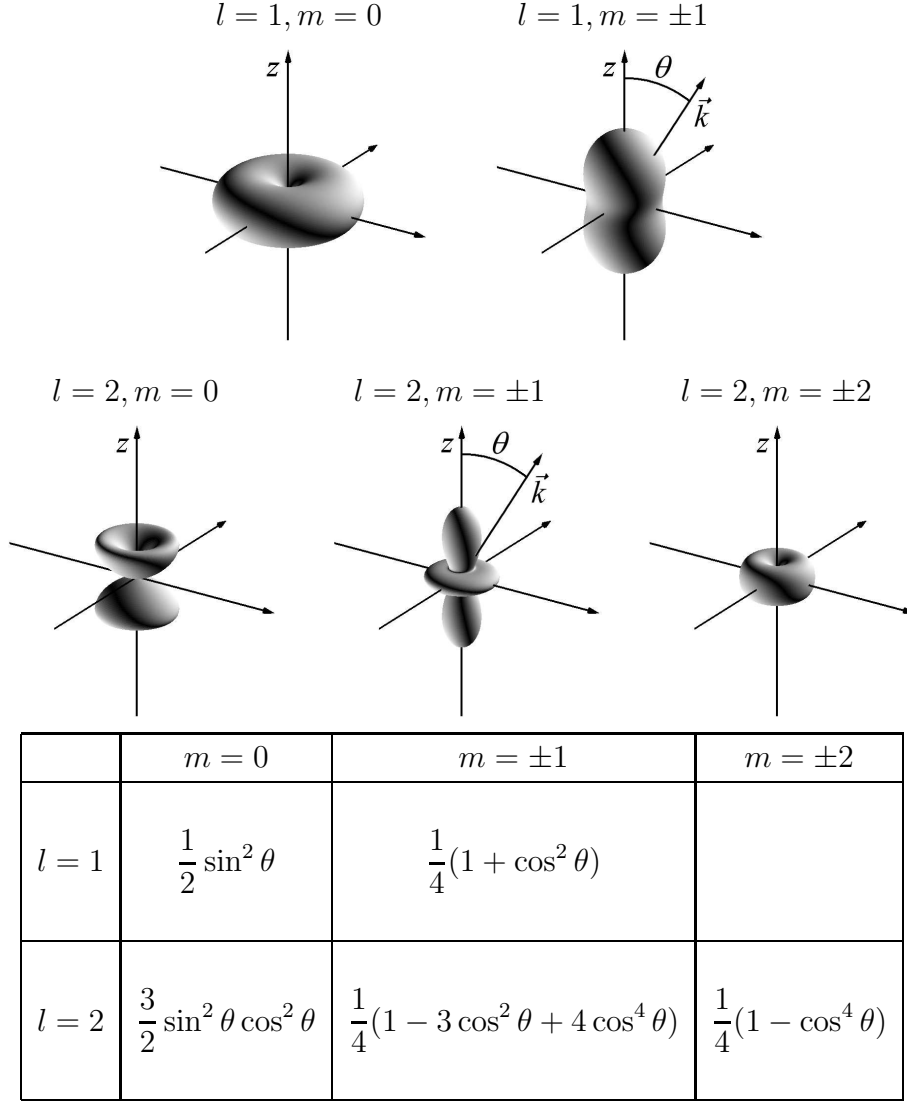
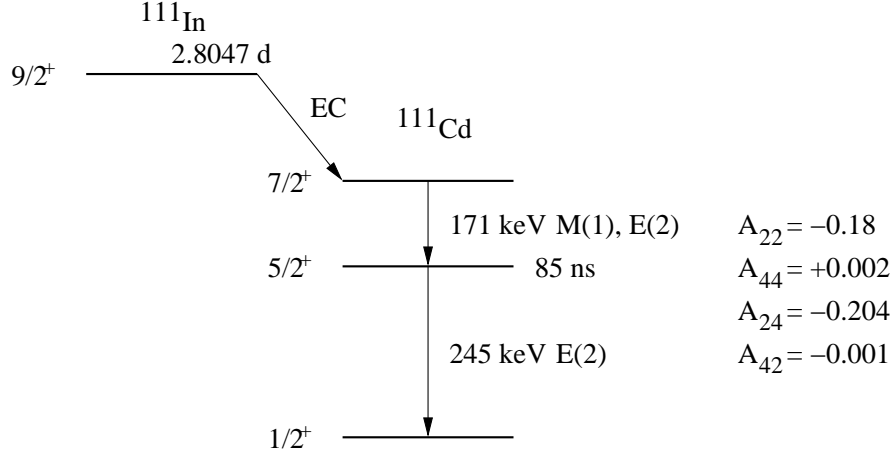


Figure 1: Illustrations of the normalized radiation characteristics F_{lm} for pure dipole and quadrupole radiation and their mathematical representations in the table below.

Illustrations of the normalized angular distribution functions for pure dipole and quadrupole radiation and their corresponding mathematical expressions are given in Figure 1.

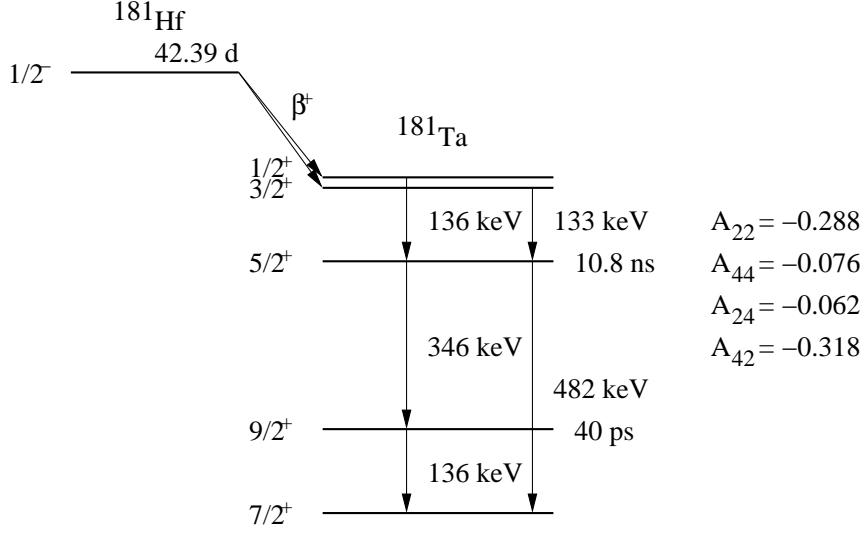
Parent isotope $^{111}\text{In} \rightarrow ^{111}\text{Cd}$, $\tau_{\frac{1}{2}} = 2.8047$ d.



State	Initial	Intermediate	Final
Spin ^{Parity}	$\frac{7}{2}^{+}$	$\frac{5}{2}^{+}$	$\frac{1}{2}^{+}$
Energy	416.70(5) keV	245.40(2) keV	0.0 keV
Half life τ_N	120 ps	85.0(7) ns	∞
Quadrupole moment (Q)	?	+0.77(12) b	none
Magnetic moment (μ)	?	-0.766(3) μ_N	-0.5948861(8) μ_N
Gamma energy	171.28(3) keV	245.40(2) keV	
Multipolarity	M(1), E(2)	E(2)	

Table 1: Characteristics of the isotope $^{111}\text{In}(\text{Cd})$. Values taken from [7, 8].

Parent isotope $^{181}\text{Hf} \rightarrow ^{181}\text{Ta}$, $\tau_{\frac{1}{2}} = 42.39$ d.



State	Initial	Intermediate	Final
Spin ^{Parity}	$\frac{1}{2}^+$	$\frac{5}{2}^+$	$\frac{7}{2}^+$
Energy	615.17(1) keV	482.18(9) keV	0.0 keV
Half life τ_N	18.1 μs	10.8 ns	∞
Quadrupole moment (Q)	?	+2.35(6) b	none
Magnetic moment (μ)	?	+3.29(3) μ_N	+2.3705(7) μ_N
Gamma energy	133.02(1) keV	482.18(9) keV	
Multipolarity	E(2)	M(1),E(2)	

Table 2: Characteristics of isotope $^{181}\text{Hf}(\text{Ta})$. Values taken from [7, 8].

Generally, the nucleus is not known to be in a definite quantum state. One can therefore assume that the initial magnetic substates are equally populated. With the detection of γ_1 in direction \vec{k}_1 a selection is made out of a pool of eigenstates of the quantum-mechanical system. The nucleus is now in an intermediate state with some relative, in general unequal population of $2I + 1$ states. Upon decaying to the ground state the detection of the second γ_2 ray in direction \vec{k}_2 is weighted with a certain probability. \vec{k}_1 and \vec{k}_2 are wave vectors in cartesian coordinates as opposed to θ and ϕ in polar coordinates. Calculations can be done to determine the probability of the observation of γ_1 and γ_2 with respect to their polar angles. The angular correlation function $W(\vec{k}_1, \vec{k}_2)$ predicts the probability of finding a γ_2 in direction \vec{k}_2 subsequent to the detection of a γ_1 in direction \vec{k}_1 .

In a quantum-mechanical formalism the initial, intermediate and final states can be described in the following ket-notation:

$$|I_i, M_i\rangle \quad , \quad |I, M\rangle \quad , \text{ and } \quad |I_f, M_f\rangle . \quad (8)$$

For the two transitions the matrix elements of the transition amplitudes can be expressed as

$$\langle I, M, \vec{k}_1, \sigma_1 | H_1 | I_i, M_i \rangle , \quad (9)$$

$$\langle I_f, M_f, \vec{k}_2, \sigma_2 | H_2 | I, M \rangle , \quad (10)$$

where H_1 and H_2 are the transition-inducing Hamiltonians. The first bracket represents the probability to find the nucleus in the state $|I, M\rangle$ right after the detection of γ_1 in direction \vec{k}_1 and polarisation σ_1 . The second bracket represents the probability to detect γ_2 under the angle $\angle(\vec{k}_2, \vec{k}_1)$. The explicit calculation over all possible states gives rise to the angular correlation function

$$W(\vec{k}_1, \vec{k}_2) = \sum_{m_i, m_f, \sigma_1, \sigma_2} \left| \sum_m \langle m_f | H_2 | m \rangle \langle m | H_1 | m_i \rangle \right|^2 . \quad (11)$$

The sublevels $|m\rangle, |m'\rangle, |m''\rangle, \dots$ form a complete set of eigenstates for the intermediate state I . Therefore, the summation in Eq. (11) is carried out incoherently, as all the mixed states have to be taken into account. In order to simplify the expressions, the lengthy terms $|I, M\rangle$ have been substituted by $|m\rangle$. Rearranging the indices yields

to the expression

$$W(\vec{k}_1, \vec{k}_2) = \sum_{m', m} \sum_{m_f} \langle m' | H_2^\dagger | m_f \rangle \langle m_f | H_2 | m \rangle \sum_{m_i} \langle m | H_1 | m_i \rangle \langle m_i | H_1^\dagger | m' \rangle. \quad (12)$$

With the definition of the density operator $\rho = \sum_m g_m |m\rangle \langle m|$ one can define

$$\rho(\vec{k}_1) |m\rangle = H_1 \rho_i H_1^\dagger |m\rangle \quad \text{and} \quad \rho(\vec{k}_2) |m\rangle = H_2^\dagger \rho_f H_2 |m\rangle. \quad (13)$$

Then Eq. (12) takes on the form

$$\begin{aligned} W(\vec{k}_1, \vec{k}_2) &= \sum_{m', m} \langle m' | \rho(\vec{k}_2) | m \rangle \langle m | \rho(\vec{k}_1) | m' \rangle = \\ &= \text{Tr} \left(\rho(\vec{k}_2) \rho(\vec{k}_1) \right). \end{aligned} \quad (14)$$

This form is the most general expression for the angular correlation function. In the density matrix formalism $\rho(\vec{k}_1)$ and $\rho(\vec{k}_2)$ describe the system immediately after the emission of γ_1 and γ_2 . No perturbations of the intermediate sublevels were regarded in this case. The following section will discuss extranuclear effects on the substates.

2.2 Perturbation of Angular Correlation

The derivation of PAC theory presented in this section follows the introduction of perturbation $\gamma\gamma$ - angular correlation of Schatz and Weidinger [3]. In general the theory describes the interaction of an intermediate nuclear state of a $\gamma\gamma$ -cascade with a perturbing potential. The intermediate state $|m\rangle$ has a finite life time τ_N . During this time the nucleus is exposed to hyperfine fields causing a realignment of the magnetic substates.

One can describe the perturbation by a unitary time-evolution operator $\Lambda(t)$, that expresses the quadrupole interaction on the intermediate substates $|m_a\rangle$ with time. It satisfies the time-dependent Schrödinger equation

$$i\hbar \frac{\partial}{\partial t} \Lambda(t) = H_{QI} \Lambda(t). \quad (15)$$

H_{QI} is the perturbing Hamiltonian and is independent of time for static interaction. In this case one solution of Eq. (15), the change of eigenstates, is expressed by the

complex phase

$$\Lambda(t) = e^{-iH_{Q1}t/\hbar}. \quad (16)$$

The population of the $|m_a\rangle$ states depends on the initial transition. The interaction of the time-evolution operator $\Lambda(t)$ on the intermediate states $|m_a\rangle$ causes a re-population into states $|m_b\rangle = \Lambda(t) |m_a\rangle$ from which the final transition into the ground states occur. The matrix elements of the Hamiltonians H_1 and H_2 are

$$\langle m_a | H_1 | m_i \rangle \quad \text{and} \quad \langle m_f | H_2 | m_b \rangle. \quad (17)$$

These amplitudes describe the probability of the population of the spin states. For no extranuclear perturbation the intermediate spin levels are $|m_a\rangle = |m_b\rangle$. The temporal change of the intermediate states through the time-evolution operator can be formally described as

$$\Lambda(t) |m_a\rangle = \left(\sum_{m_b} |m_b\rangle \langle m_b| \right) \Lambda(t) |m_a\rangle. \quad (18)$$

The expression in parentheses represents the unit operator, a superposition of all pure intermediate eigenstates. The angular correlation equation for the perturbed case rises from the combination of the probability amplitudes of the first transition and the perturbed probability amplitude of the second transition. The matrix elements are

$$\langle m_a | H_1 | m_i \rangle \quad \text{and} \quad \langle m_f | H_2 \Lambda(t) | m_a \rangle. \quad (19)$$

The probability density function of the emission of the two successive transitions in directions \vec{k}_1 and \vec{k}_2 yields to the expression

$$W(\vec{k}_1, \vec{k}_2, t) = \sum_{m_f, m_i} \left| \sum_{m_a} \langle m_f | H_2 \Lambda(t) | m_a \rangle \langle m_a | H_1 | m_i \rangle \right|^2 \quad (20)$$

Inserting Eq. (18) into Eq. (20) one can calculate a more explicit expression of $W(k_1, k_2, t)$. With the absolute square value executed and some summation terms

rearranged the probability density can be rewritten as

$$\begin{aligned}
 W(\vec{k}_1, \vec{k}_2, t) &= \\
 &= \sum_{m_f, m_i, m_a, m'_a, m_b, m'_b} \langle m_f | H_2 | m_b \rangle \langle m_b | \Lambda(t) | m_a \rangle \langle m_a | H_1 | m_i \rangle \cdot \\
 &\quad \cdot \langle m_f | H_2 | m'_b \rangle^* \langle m'_b | \Lambda(t) | m'_a \rangle^* \langle m'_a | H_1 | m_i \rangle^*
 \end{aligned} \tag{21}$$

The impact of the perturbation displays itself only in the two separated brackets where the time-evolution operator $\Lambda(t)$ appears. A more complicated and lengthy calculation brings Eq. (21) into a more accessible form

$$\begin{aligned}
 W(\vec{k}_1, \vec{k}_2, t) &= \sum_{k_1, k_2}^{k_{max}} \sum_{N_1, N_2} A_{k_1}(\gamma_1) A_{k_2}(\gamma_2) G_{k_1 k_2}^{N_1 N_2}(t) \cdot \\
 &\quad \cdot \frac{1}{\sqrt{(2k_1 + 1)(2k_2 + 1)}} Y_{k_1}^{N_1*}(\theta_1, \phi_1) Y_{k_2}^{N_2}(\theta_2, \phi_2),
 \end{aligned} \tag{22}$$

with the separated perturbation factor

$$\begin{aligned}
 G_{k_1 k_2}^{N_1 N_2}(t) &= \sum_{m_a, m'_a, m_b, m'_b} (-1)^{2I+m_a+m_b} \sqrt{(2k_1 + 1)(2k_2 + 1)} \cdot \\
 &\quad \cdot \begin{pmatrix} I & I & k_1 \\ m'_a & -m_a & N_1 \end{pmatrix} \begin{pmatrix} I & I & k_2 \\ m'_b & -m_b & N_2 \end{pmatrix} \langle m_b | \Lambda(t) | m_a \rangle \langle m'_b | \Lambda(t) | m'_a \rangle^*.
 \end{aligned} \tag{23}$$

\vec{k}_1 and \vec{k}_2 are the wave vectors of the two successive γ -rays. $A_k(\gamma_1)$ and $A_k(\gamma_2)$ are anisotropy coefficients. The parameter $A_{k_1}(\gamma_1) = A_{k_1}(l_1, l'_1, I_i, I)$ is a number which depends only on the multipolarity of the emitted radiation l_1 and l'_1 , and the spins of the nuclear states involved in the transition. The parameter $A_{k_2}(\gamma_2) = A_{k_2}(l_2, l'_2, I_f, I)$ is similar to the one before, but involving the multipolarities and spins of the second transition. Tabulated values can be found in [4, 5]. The index k is limited by the relation

$$0 \leq k \leq k_{max} = \min(2I, l_1 + l'_1, l_2 + l'_2), \tag{24}$$

where k_{max} is the highest index representing the highest involved spin state. The summation contains only even values of k because it is restricted to directional γ - γ angular correlation, not measuring the circular polarization of the emitted γ -rays.

One can find a set of eigenvectors $|n\rangle$, for that a diagonalized form of the perturbing

Hamiltonian H_{QI} exists. The scalar products in the perturbation factor (23) can be rewritten into the following form by inserting Eq. (16)

$$\begin{aligned}
\langle m_b | \Lambda(t) | m_a \rangle \langle m'_b | \Lambda(t) | m'_a \rangle^* &= \\
&= \sum_{n, n'} \langle m_b | n \rangle \langle n | m_a \rangle e^{-itE_{QI}/\hbar} \langle m'_b | n' \rangle \langle n' | m'_a \rangle e^{itE'_{QI}/\hbar} = \\
&= \sum_{n, n'} \langle m_b | n \rangle \langle m'_b | n' \rangle^* \langle m_a | n \rangle^* \langle m'_a | n' \rangle e^{-it(E_{QI} - E'_{QI})/\hbar} \quad (25)
\end{aligned}$$

It is easy to see that Eq. (25) contains a complex phase, which incarnates a splitting of the energy levels. The degeneracy of the intermediate sub-levels is hence broken up. The energy eigenvalues can be written as

$$E_m = \hbar\omega_Q (3m^2 - I(I+1)). \quad (26)$$

For half-integer I there are $(2I+1)/2$ ($I+1$ for integer I) doubly degenerate m levels.

2.3 Absence of Perturbation

The influence of the extranuclear perturbation is completely described by the perturbation factor. The magnitude is contained in the Hamilton operator H_{QI} for quadrupole interaction, which determines $\Lambda(t)$ from Eq. (16). For a vanishing perturbation $H_{QI} = 0$ the time-evolution operator reduces to the identity. The matrix elements from Eq. (23) vanish for all states $a \neq b$, and therefore is $N := N_1 = N_2$. With the orthogonality relation of the 3-j symbols [16],

$$\sum_{m_a, m'_a} \begin{pmatrix} I & I & k_1 \\ m'_a & -m_a & N_1 \end{pmatrix} \begin{pmatrix} I & I & k_2 \\ m'_a & -m_a & N_2 \end{pmatrix} = (2k_1 + 1)^{-1/2} \delta_{k_1, k_2} \delta_{N_1, N_2}. \quad (27)$$

the perturbation factor then becomes

$$G_{k_1 k_2}^{N_1 N_2}(t) = \delta_{k_1 k_2} \delta_{N_1 N_2}. \quad (28)$$

Thus, the angular correlation function (22) reduces to

$$W(\vec{k}_1, \vec{k}_2) = \sum_{k=0, \text{even}}^{k_{\max}} A_{k_1} A_{k_2} P_k(\cos \theta), \quad (29)$$

which is now independent of time.

2.4 Polycrystalline Samples

Angular correlation experiments are usually carried out on polycrystalline samples. Polycrystalline samples, or powder samples, consists of a large number of randomly oriented microcrystals. It is possible to express the perturbation factor by averaging over all possible orientations of microcrystals. This has been done by [19]. The matrix elements of Eq. (25) need to be integrated over the solid angles that account for all possible orientations. This leads to the mean perturbation factor

$$\int d\vec{\Omega} G_{k_1 k_2}^{N_1 N_2}(t) = \delta_{k_1 k_2} \delta_{N_1 N_2} \sum_{m, m'} s_{mm'}^{k_1 k_2} e^{-it(E_{QI} - E'_{QI})/\hbar} = G_{kk}^{NN}(t), \quad (30)$$

which is diagonal in N and k . The s_m^k coefficients can now be separated into a so called "hard-core" term, which is time-independent, and time-dependent terms that represent the different split sub-levels of the perturbation. The hard-core term originates from all states $|n\rangle = |n'\rangle$. The time-dependent terms are generated from all states $|n\rangle \neq |n'\rangle$. The perturbation factor for a powder source takes on the form

$$G_{kk}(t) = \sum_m s_{mm}^{kk} + \sum_{m \neq m'} s_{mm'}^{kk} \cos((E_m - E'_{m'})t/\hbar). \quad (31)$$

Using Eq. (26) and introducing a new index $n = |m^2 - m'^2|/2$ for half-integer I ($n = |m^2 - m'^2|$ for integer I) the core parameters can be written as

$$s_n^k = \sum_{mm'} s_{mm'}^{kk} \delta_{n, |m^2 - m'^2|/2}, \quad \text{half-integer } I \quad (32)$$

$$s_n^k = \sum_{mm'} s_{mm'}^{kk} \delta_{n, |m^2 - m'^2|}, \quad \text{integer } I \quad (33)$$

Thus, Eq. (31) can be simplified as

$$G_{kk}(t) = s_0^k + \sum_{n>0} s_n^k \cos(\omega_n t). \quad (34)$$

The angular frequency ω_1 is equivalent to smallest non-vanishing quadrupole frequency $6\omega_Q$ for half-integer I ($3\omega_Q$ for integer I). There is no perturbation for $t = 0$,

thus $G(t=0) = 1$. This concludes that the sum of all core parameters is $\sum_n s_n^k = 1$. One feature of the hard-core term is, that the angular correlation is not completely zero for a powder sample, even if the time-dependent perturbation vanishes. The simplified angular correlation function can hence be rewritten as

$$W(\theta, t) = \sum_{k=0, \text{even}}^{k_{max}} A_{kk} G_{kk}^{NN}(t) P_k(\cos \theta). \quad (35)$$

This expression is only dependent of the angle $\theta = \angle(\vec{k}_1, \vec{k}_2)$ and the time t . The angular correlation function consists of the time-dependent anisotropy $A_{kk} G_{kk}(t)$ and the angular term $P_k(\cos \theta)$. For the two most commonly used PAC probes, $^{111}\text{In}(\text{Cd})$ and $^{181}\text{Hf}(\text{Ta})$, the nuclear spin is $I = 5/2$, which yields to $k_{max} = 4$. For these elements the anisotropy coefficients A_{00} , A_{22} , and A_{44} are involved. For the zero-order term the Legendre polynomial $P_0(\cos \theta)$ and the A_{00} are equal to 1. Since $A_{44} \ll A_{22}$ for both $^{111}\text{In}(\text{Cd})$ and $^{181}\text{Hf}(\text{Ta})$ probes they are usually neglected in the analysis of the correlation function for practical reasons.

2.5 Static Electric Quadrupole Interaction

The electric quadrupole interaction is the interaction of the nuclear quadrupole moment with an electric field gradient (EFG) at the nucleus. The EFG is characteristic of the charge distribution around the nucleus. It is usually described by a tensor V_{aa} containing the symmetry of the charge distribution. The presence of an EFG causes a splitting of the degenerate eigenstates of the intermediate state $|I, M\rangle$.

The nucleus behaves like a non-spherical charge distribution. Its energy level depends on the quantity of nuclear and external charges and how this charge distribution is oriented with respect to the external EFG. The EFG is produced by an electrostatic potential

$$\phi(\vec{r}) = \frac{1}{4\pi\epsilon_0} \sum_i \frac{e_i}{|\vec{r} - \vec{r}_i|}. \quad (36)$$

This field originates mostly by external negative charges such as by electrons surrounding the nucleus. The classical description of the energy of a nuclear charge distribution $\rho_N(\vec{r})$ in the potential $\phi(\vec{r})$ is the Coulomb energy

$$E_{el} = \int_V \rho_N(\vec{r}) \phi(\vec{r}) d\vec{r}. \quad (37)$$

The potential $\phi(\vec{r})$ can be developed into a Taylor series around the center of the nucleus \vec{x} [10]

$$\begin{aligned} \phi(\vec{x} + \vec{r}) &= \sum_{j=0}^{\infty} \left[\frac{1}{j!} (\vec{r} \cdot \vec{\nabla}_{\vec{x}'})^j \phi(\vec{x}') \right]_{\vec{x}'=\vec{x}} = \\ &= \phi(\vec{x}) + \vec{r} \vec{\nabla} \phi(\vec{x}) + \frac{1}{2} (\vec{r} \vec{\nabla})^2 \phi(\vec{x}) + \dots = \\ &= \phi(\vec{x}) + \sum_i \vec{r} \frac{\partial \phi(\vec{x})}{\partial x_i} + \frac{1}{2} \sum_{ij} \frac{\partial^2 \phi(\vec{x})}{\partial x_i \partial x_j} r_i r_j + \dots \end{aligned} \quad (38)$$

Without loss of generality it can be assumed that the nucleus is located at $\vec{x} = 0$. The first term expresses the contribution from a point charge at the center of the nucleus to the electrostatic potential $\phi_0 = \phi(\vec{x} = 0)$. The second term contains the electric potential $\vec{E}_0 = -\vec{\nabla} \phi(\vec{x} = 0)$. It describes the interaction between a dipole moment of the nucleus and the electric field \vec{E} . The third term is called the quadrupole term. In fact it is a combination of a monopole term and the pure quadrupole term. The monopole term is related to the average radius of the nucleus and is responsible for

the isotope shift in isotopes with different radii [11]. It is, according to Poisson's law,

$$\Delta\phi(\vec{x}) = \sum_{ij} \frac{\partial^2 \phi(\vec{x})}{\partial x_i \partial x_j} = \vec{\nabla} \cdot \vec{\nabla} \phi(\vec{x}) = \vec{\nabla} \cdot \vec{E}(\vec{x}) = -\frac{\rho_N(\vec{x})}{\varepsilon_0}. \quad (39)$$

Thus the source for the monopole field is the nuclear charge $q = \int \rho_N(\vec{r}) d\vec{r} = eZ$ with the charge distribution located about $\vec{x} = 0$. To simplify things the monopole term is separated from the quadrupole term in (38) by adding and subtracting $\frac{1}{3}\Phi_{ij}r^2\delta_{ij}$. The partial derivatives have been replaced by $\Phi_{ij} := \frac{\partial^2 \phi}{\partial x_i \partial x_j}$. The separated quadrupole term is now trace-free. Under these considerations the Taylor series (38) can be rewritten into the form

$$\phi(\vec{r}) = \phi_0 - \vec{r} \cdot \vec{E}_0 + \frac{1}{6}r^2 \sum_i \Phi_{ii} + \frac{1}{2} \sum_{ij} \Phi_{ij} (r_i r_j - \frac{r^2}{3} \delta_{ij}) + \dots \quad (40)$$

Inserting (39) into the third term of (40) gives

$$\phi(\vec{r}) = \phi_0 - \vec{r} \cdot \vec{E}_0 + \frac{1}{6}r^2 \Delta\phi_0 + \frac{1}{6} \sum_{ij} \Phi_{ij} (3r_i r_j - r^2 \delta_{ij}) + \dots \quad (41)$$

The electrostatic energy of the nucleus can now be calculated by inserting (40) into (37). The Coulomb energy of the nucleus looks like

$$\begin{aligned} E_{el} &= \phi_0 \int_V \rho_N(\vec{r}) d\vec{r} - \\ &\quad - \int_V \rho_N(\vec{r}) \vec{r} \cdot \vec{E}_0 d\vec{r} + \\ &\quad + \frac{1}{6} \Delta\phi_0 \int_V \rho_N(\vec{r}) r^2 d\vec{r} + \\ &\quad + \frac{1}{6} \sum_{ij} \Phi_{ij} \int_V \rho_N(\vec{r}) (r_i r_j - r^2 \delta_{ij}) d\vec{r} + \dots = \\ &= q\phi_0 - \vec{p} \cdot \vec{E}_0 + \frac{1}{6} \Delta\phi_0 q r_N^2 + \frac{e}{6} \sum_{ij} \Phi_{ij} Q_{ij} + \dots \end{aligned} \quad (42)$$

Here is r_N the average radius of the nucleus. By definition is \vec{p} the classical dipole moment and

$$Q_{ij} = \frac{1}{e} \int \rho(\vec{r}) (3x_i x_j - r^2 \delta_{ij}) dV \quad (43)$$

the classical quadrupole moment¹. With the selection of a suitable coordinate system the integral of the non-diagonal elements is equal to zero $Q_{ij} = 0|_{i \neq j}$ and the quadrupole moment tensor is therefore diagonalized. It can further be shown that Q_{ij} is trace-free² ($\text{tr}(Q_{ij}) = 0$). The fourth term of (42) is the quadrupole energy term. It can be expressed as

$$E_Q = \frac{e}{6} \sum_a V_{aa} Q_{aa}, \quad (44)$$

where V_{aa} is the tensor of the electric field gradient (EFG). The quadrupole energy results from the alignment of the nucleus quadrupole moment with an external electric field gradient. As in this work only the quadrupole interactions are of interest the other terms are disregarded in further considerations. The V_{aa} is a symmetric tensor with $\text{tr}(V_{aa}) = 0$. Typically V_{aa} is expressed through the asymmetry parameter η and V_{zz} by

$$\eta = \frac{V_{xx} - V_{yy}}{V_{zz}}. \quad (45)$$

η can be a value between $0 \leq \eta \leq 1$ provided the principal axis is defined such that $|V_{zz}| \geq |V_{yy}| \geq |V_{xx}|$. $\eta = 0$ is the axially symmetric case, where $V_{xx} = V_{yy}$ with the z-axis as the EFGs symmetry axis. V_{aa} and Q_{aa} are tensors in cartesian coordinates. They were derived by using the classical approach.

The quantum-mechanical approach to the solution above is similar. A thorough introduction of electric field gradient interaction has been written by Lu [15]. The Coulomb energy of a charge distribution in an external potential is described by the Hamiltonian for electrostatic interaction

$$H_{EI} = \sum_{ij} \frac{e_i e_j}{|\vec{r}_i - \vec{r}_j|}. \quad (46)$$

The quantities with index i are the charges and coordinates of the nucleus, and the quantities with index j are those of its environment. This is the quantum-mechanical analogue to (37). For $|r_i| > |r_j|$ the distance between the nucleus and the external

¹The dimension of the electrodynamic quadrupole moment term is $As \cdot m^2$. In many quantum-mechanical publications the quadrupole moment Q is defined by $Q^{qm} = e^{-1} Q^{ed}$, where the quadrupole moment is reduced by the elementary charge.

²The sum of the diagonal terms contain $\sum_i 3r_i^2 - r^2 = 0$.

potential producing charges is large enough, (46) can be rewritten as ³

$$H_{EI} = \sum_{ij} \sum_{l=0}^{\infty} \frac{e_i e_j r_i^l}{r_j^{l+1}} P_l(\cos \theta_{ij}). \quad (47)$$

$\cos \theta_{ij} := \frac{\langle \vec{r}_i, \vec{r}_j \rangle}{|\vec{r}_i| |\vec{r}_j|}$ is the angle spanned by r_i and r_j . With the help of (6) and the addition theorem for spherical harmonic functions the above formula can be expressed through the spherical harmonic functions

$$H_{EI} = \sum_{ij} \sum_{l=0}^{\infty} \frac{4\pi}{2l+1} e_i e_j \sum_{m=-l}^l Y_l^{m*}(\theta_i, \varphi_i) Y_l^m(\theta_j, \varphi_j). \quad (48)$$

Reordering the summation terms and using the complex conjugation of $Y_l^{m*} = (-1)^m Y_l^{-m}$ we can rewrite (48) into the form

$$H_{EI} = \sum_{l=0}^{\infty} \frac{4\pi}{2l+1} \sum_m (-1)^m \sum_i e_i r_i^l Y_l^m(\theta_i, \varphi_i) \sum_j e_j \frac{1}{r_j^{l+1}} Y_l^{-m}(\theta_j, \varphi_j). \quad (49)$$

A more compact form of (49) can be achieved when the two summations over i and j are replaced by two spherical tensor operators $Q_m^{(l)}$ and $V_m^{(l)}$ of rank l [13]. With the definition of the scalar product of two tensor operators

$$Q^{(k)} \cdot V^{(k)} = \sum_{m=-l}^l (-1)^m Q_m^{(l)} V_{-m}^{(l)} \quad (50)$$

and

$$Q_m^{(l)} = \sum_i e_i r_i^l Y_l^m(\theta_i, \varphi_i) \quad , \quad V_m^{(l)} = \sum_j \frac{e_j}{r_j^{l+1}} Y_l^{-m}(\theta_j, \varphi_j) \quad (51)$$

(49) becomes

$$H_{EI} = \sum_{l=0}^{\infty} \frac{4\pi}{2l+1} Q^{(l)} V^{(l)}. \quad (52)$$

The Hamiltonian is now expressed by the product of two factors, a nuclear factor and an external field factor. The summation is of order l . In analogy to the classical description the terms of order $l = 0$ are the monopole terms, $l = 1$ dipole terms, and $l = 2$ the quadrupole terms. Higher order terms are generally not regarded as their

³see Green's functions of the Laplace operator

contributions are negligible. Practically it is enough to assume the first three terms of the Hamiltonian

$$\begin{aligned}
H_{EI} = & 4\pi q V^{(0)} + \\
& + \frac{4\pi}{3} \sum_{m=-1}^1 (-1)^m Q_m^{(1)} V_{-m}^{(1)} + \\
& + \frac{4\pi}{5} \sum_{m=-2}^2 (-1)^m Q_m^{(2)} V_{-m}^{(2)} \quad (53)
\end{aligned}$$

The lowest order term contains $V^{(0)}$, the Coulomb potential. The order $l = 1$ term vanishes due to the requirement of parity conservation under a space reflection. The only term that needs to be retained in the electrostatic interaction is the quadrupole term. The quadrupole interaction Hamiltonian is therefore

$$H_{QI} = \frac{4\pi}{5} Q^{(2)} \cdot V^{(2)}. \quad (54)$$

$V^{(2)}$ is the quantum-mechanical analogue to the classical electric field gradient operator V_{aa} . The spherical components $V_m^{(2)}$ can be expressed in terms of the cartesian derivatives V_{xx}, V_{xy}, \dots . With the Coulomb potential (36) the tensor components of V_{aa} can be derived as follows

$$\begin{aligned}
\frac{\partial^2 \phi(\vec{r})}{\partial z^2} &= \sum_i \frac{e_i}{|\vec{r} - \vec{r}_i|^5} (3z_i^2 - r_i^2) = \\
&= \sum_i \frac{e_i}{|\vec{r} - \vec{r}_i|^3} (3 \cos^2 \theta_i - 1) = \\
&= 4\sqrt{\frac{\pi}{5}} \sum_i \frac{e_i}{|\vec{r} - \vec{r}_i|^3} Y_2^0(\theta_i, \varphi_i). \quad (55)
\end{aligned}$$

From (51) the relation with the spherical derivatives can be identified as

$$\begin{aligned}
V_0^{(2)} &= \frac{1}{4} \sqrt{\frac{5}{\pi}} V_{zz}, \\
V_{\pm 1}^{(2)} &= \mp \frac{1}{2} \sqrt{\frac{5}{6\pi}} (V_{xz} \pm iV_{yz}), \\
V_{\pm 2}^{(2)} &= \frac{1}{4} \sqrt{\frac{5}{6\pi}} (V_{xx} - V_{yy} \pm i2V_{xy}). \quad (56)
\end{aligned}$$

From Eq. (44) it is known that the non-diagonal elements of the electric field gradient tensor vanish with the selection of the coordinate system z- axis along the principal axis of the EFG, so that in this case (56) reduce to

$$\begin{aligned} V_0^{(2)} &= \frac{1}{4}\sqrt{\frac{5}{\pi}}V_{zz}, \\ V_{\pm 1}^{(2)} &= 0, \\ V_{\pm 2}^{(2)} &= \frac{1}{4}\sqrt{\frac{5}{6\pi}}\eta V_{zz}. \end{aligned} \quad (57)$$

The matrix elements of the quadrupole Hamiltonian (54) are

$$\langle I, M | H_{QI} | I, M' \rangle = \frac{4\pi}{5} \sum_{m=-2}^2 (-1)^m \langle I, M | Q_m^{(2)} | I, M' \rangle V_{-m}^{(2)}. \quad (58)$$

Using the Wigner-Eckhart theorem the matrix elements can be calculated as

$$\langle I, M | Q_m^{(2)} | I, M' \rangle = (-1)^{I-M} \begin{pmatrix} I & I & 2 \\ M' & -M & m \end{pmatrix} \langle I || Q^{(2)} || I \rangle, \quad (59)$$

where $\langle I || Q^{(2)} || I \rangle$ is the reduced matrix element. Under the assumption that the matrix element of a known ground state $M = I$ is not equal to zero, the reduced matrix element can be calculated as

$$\langle II | Q_0^{(2)} | II \rangle = \begin{pmatrix} I & I & 2 \\ I & -I & 0 \end{pmatrix} \langle I || Q^{(2)} || I \rangle. \quad (60)$$

The conventional definition of the nuclear quadrupole moment (43) can be expressed in spherical coordinates using (55)

$$Q = \frac{1}{e} Q_0^{(2)} = \frac{1}{e} r^2 Y_2^0 = \frac{1}{e} \sqrt{\frac{16\pi}{5}} \langle II | Q_0^{(2)} | II \rangle. \quad (61)$$

Inserting (61) and (60) into (59) delivers the following expression of the matrix elements of the quadrupole moment tensor

$$\langle I, M | Q_m^{(2)} | I, M' \rangle = (-1)^{I-M} \sqrt{\frac{5}{16\pi}} e Q \begin{pmatrix} I & I & 2 \\ M' & -M & m \end{pmatrix} \begin{pmatrix} I & I & 2 \\ I & -I & 0 \end{pmatrix}^{-1}. \quad (62)$$

Defining

$$\begin{aligned} c_0^{(2)}(M) &= 3M^2 - I(I+1), \\ c_{\pm 1}^{(2)}(M) &= (1 \mp 2M)\sqrt{(I \pm M)(I \mp M + 1)}, \\ c_{\pm 2}^{(2)}(M) &= \sqrt{(I \pm M - 1)(I \pm M)(I \mp M + 1)(I \mp M + 2)}, \end{aligned} \quad (63)$$

one can express the following 3j-symbols in terms of $c_{\pm m}^{(2)}(M)$ [14]:

$$\begin{aligned} \begin{pmatrix} I & I & 2 \\ M & -M & 0 \end{pmatrix} &= (-1)^{I-M} \sqrt{\frac{4}{f_I}} c_0^{(2)}(M), \\ \begin{pmatrix} I & I & 2 \\ \mp M & \pm M - 1 & 1 \end{pmatrix} &= (-1)^{I \pm M} \sqrt{\frac{6}{f_I}} c_{\pm 1}^{(2)}(M), \\ \begin{pmatrix} I & I & 2 \\ \mp M & \pm M - 2 & 2 \end{pmatrix} &= (-1)^{I \pm M} \sqrt{\frac{6}{f_I}} c_{\pm 2}^{(2)}(M), \end{aligned} \quad (64)$$

where $f_I = (2I-1)2I(2I+1)(2I+2)(2I+3)$. The $c_{\pm m}^{(2)}(M)$ have the properties

$$\begin{aligned} c_{\pm 1}^{(2)}(M) &= -c_{\mp 1}^{(2)}(M \mp 1), \\ c_{\pm 2}^{(2)}(M) &= c_{\mp 2}^{(2)}(M \mp 2). \end{aligned} \quad (65)$$

Substituting Eqs. (62) and (64) into Eq. (58), one obtains

$$\begin{aligned} \langle IM | H_{QI} | IM' \rangle &= \sqrt{\frac{24\pi}{5}} \frac{\hbar\omega_Q}{V_{zz}} \left[\sqrt{\frac{2}{3}} c_0^{(2)}(M) V_0^{(2)} \delta_{m',m} + \right. \\ &\quad + c_{+1}^{(2)}(M) V_{+1}^{(2)} \delta_{m',m-1} + c_{-1}^{(2)}(M) V_{-1}^{(2)} \delta_{m',m+1} + \\ &\quad \left. + c_{+2}^{(2)}(M) V_{+2}^{(2)} \delta_{m',m-2} + c_{-2}^{(2)}(M) V_{-2}^{(2)} \delta_{m',m+2} \right], \end{aligned} \quad (66)$$

where the quadrupole coupling constant ω_Q is defined as

$$\omega_Q = \frac{eQV_{zz}}{4I(2I-1)\hbar}. \quad (67)$$

From Eq. (57) one can see that in the principal axis system only the diagonal terms $V_0^{(2)}$ and the off-diagonal terms $V_{\pm 2}^{(2)}$ are not equal to zero. The non-vanishing matrix

elements of the quadrupole Hamiltonian are therefore

$$\langle IM \pm 2 | H_{QI} | IM \rangle = \hbar \omega_Q \frac{\eta}{2} c_{\mp 2}^{(2)}(m), \quad (68)$$

and

$$\langle IM \pm 2 | H_{QI} | IM \rangle = \hbar \omega_Q c_0^{(2)}(m). \quad (69)$$

For the axially symmetric case $\eta = 0$ the quadrupole Hamiltonian is diagonal. The eigenvalues

$$E_Q(M) = \langle IM | H_{QI} | IM \rangle = \hbar \omega_Q (3M^2 - I(I+1)) \quad (70)$$

are doubly degenerate in M . As an example the spin state $I = \frac{5}{2}$ shall be considered, as the two most commonly used PAC probes $^{111}\text{In}(\text{Cd})$ and $^{181}\text{Hf}(\text{Ta})$ have intermediate state with nuclear spin $\frac{5}{2}$. The possible energy eigenvalues can easily be evaluated by

$$\begin{aligned} E_Q(\pm \frac{5}{2}) &= 10\hbar\omega_Q, \\ E_Q(\pm \frac{3}{2}) &= -2\hbar\omega_Q, \\ E_Q(\pm \frac{1}{2}) &= -8\hbar\omega_Q. \end{aligned} \quad (71)$$

The PAC frequencies ω_n are the differences of the energy eigenstates in Eqs. (71):

$$\begin{aligned} \omega_1 &= \left| E_Q(\frac{3}{2}) - E_Q(\frac{1}{2}) \right| / \hbar = 6\omega_Q, \\ \omega_2 &= \left| E_Q(\frac{5}{2}) - E_Q(\frac{3}{2}) \right| / \hbar = 12\omega_Q, \\ \omega_3 &= \left| E_Q(\frac{5}{2}) - E_Q(\frac{1}{2}) \right| / \hbar = 18\omega_Q. \end{aligned} \quad (72)$$

For the axially symmetric case $\eta = 0$ all three PAC frequencies $\omega_1:\omega_2:\omega_3$ for spin state $I = \frac{5}{2}$ line up in the ratio of 1:2:3.

2.6 Static Magnetic Dipole Interaction

A charged rotating body has a magnetic moment $\vec{\mu}$ when it exhibits an angular moment \vec{I} . The ratio between these two quantities is defined as

$$\vec{\mu} = \gamma \vec{I}, \quad (73)$$

where γ is the gyromagnetic ratio. Classically the gyromagnetic ratio $\gamma = \frac{q}{2m}$ is defined as a charge and a mass distributed uniformly. Protons, neutrons, and many nuclei, however, carry nuclear spin that gives rise to a gyromagnetic ratio as above. The ratio is conventionally written in terms of proton mass and elementary charge as

$$\gamma = \frac{e}{2m_p} g = g \frac{\mu_N}{\hbar}. \quad (74)$$

The factor g is the Lande g-factor which is a dimensionless quantity that characterizes the magnetic moment and the gyromagnetic ratio of the particle, and μ_N is the nuclear magneton.

If the magnetic nuclear dipole moment $\vec{\mu}$ is exposed to a magnetic flux density \vec{B} , then the interaction energy is

$$E_M = -\vec{\mu} \cdot \vec{B}. \quad (75)$$

Classically the magnetic energy depends on the angle between $\vec{\mu}$ and \vec{B} . In the quantum-mechanical world exists a direction quantization, that forces only certain adjustments for μ . If the \vec{B} -field is parallel to the z -axis the magnitude of the magnetic energy of the angular momentum state $|I, M\rangle$ is

$$\begin{aligned} E_M(M) &= \langle I, M | -\mu_z B_z | I, M \rangle = \\ &= -\gamma B_z \langle I, M | I_z | I, M \rangle = -\gamma B_z \hbar M. \end{aligned} \quad (76)$$

As can be seen in Eq. (76) the magnetic energy is linear in M . Therefore the energy levels

$$E_M(M) - E_M(M') = -(M - M')\gamma B_z \hbar = N \hbar \omega_L, \quad (77)$$

are equispaced, where ω_L is the classical Larmor frequency and $N = M' - M$ the distance of two M -states. It describes the precession frequency of the nuclear angular moment \vec{I} under the influence of a \vec{B} -field. The magnetic flux \vec{B} causes the splitting of the degenerate energy levels. For magnetic interaction the perturbation factor $G_{kk}^{NN}(t)$

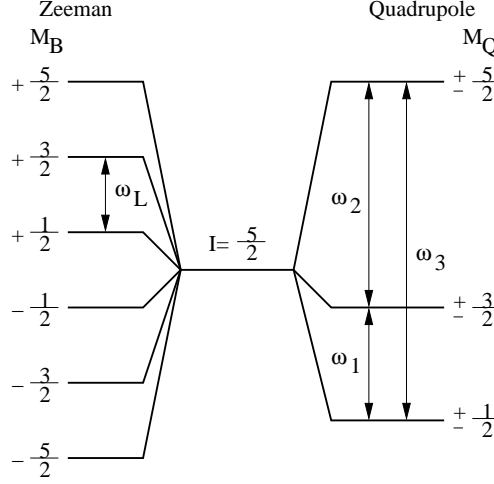


Figure 2: Energy scheme showing the degeneracy of an intermediate state $I = 5/2$. On the left are pictured the equidistant energy levels due to magnetic dipole interaction with their characteristic Larmor frequency ω_L . On the right the removal of the degeneracy due to quadrupole interaction is presented with the typical PAC frequencies ω_1 , ω_2 and the sum of them ω_3 .

is calculated by inserting Eq. (77) into the Eq. (30). The obtained expression for the perturbation factor

$$G_{kk}^{NN}(t) = e^{-iN\omega_L t} \quad (78)$$

is modulated by integer multiples of the Larmor frequency. The indices N and k underlie restrictions of Eq. (24). Because $N \leq 2I$, the maximum observable harmonic of the Larmor frequency for $I = 5/2$ is $N = 5$. For the polycrystalline sample case the index k in Eq. (35) is further restricted to $k_{max} = 2$ and k even. Since also $|N| \leq k$ the perturbation factor for the polycrystalline sample case can only contain the Larmor frequency ω_L and its second harmonic $2\omega_L$. With Eq. (78) the magnetic angular correlation function takes on the form

$$W(\theta, t) = \sum_k b_k \cos(k\omega_L t). \quad (79)$$

Figure 2 shows the splitting of the energy levels of a nucleus with angular momentum $\frac{5}{2}$ for both magnetic and quadrupole interaction. The removal of the degeneracy due to magnetic interaction is portrayed on the left side, the electric on the right. The splitting of the energies under the magnetic effect is also known as the nuclear Zeeman-effect [12].

3 Hardware

3.1 Overview of Setup and Operation

Conventional TDPAC spectrometer can basically be distinguished into slow-fast and fast-fast systems. In both systems the timing signal is derived from the anode of the Secondary-Electron Multiplier (SEM) tube. The energy signal is typically taken from the PMT dynode. The dynode signal is amplified and shaped by Linear Amplifier (LA). A scintillator crystal attached to the SEM's optical cathode window will convert the high-energy γ into ultraviolet light. The flashes enter through the optical window and strike out electrons from the negative cathode. Those electrons are being multiplied over several cascades until the avalanche reaches the positive anode. A combination of scintillator crystal and SEM is also referred to as a Photo-Multiplier Tube (PMT). Typically, in slow-fast systems NaI crystals are being used for better energy, but less timing resolution. In fast-fast systems BaF₂ crystals are being used for faster timing, but less energy resolution.

In slow-fast systems the time and energy events are available at different times. The energy determination is regarded as a slow process because the shape of the dynode pulse for NaI detectors is broader. The energy information is more precise when integrated because a NaI scintillator produces more visible photons for a given gamma than BaF₂ does. In fast-fast systems the time and energy information are practically available at the same time. The fast component of a BaF₂ detector's anode pulse enhances the detection of the signal's arrival time. The much smaller slow component contributes less information when integrated. This yields, in comparison to NaI scintillators, to an inferior energy resolution. The energy information is available faster due to shorter integration times.

The energy discrimination is performed subsequent to the amplification by twin Single Channel Analyzer (SCA). The energy information is sorted into Start and Stop events according to the energy windows. One SCA has its window set on the lower energy γ and the other on the higher energy. The size of the windows are usually sufficiently small so no overlap can occur.

The anode signal is usually artificially delayed by electronic circuitry until the energy information from the slow circuit is available. With the arrival of a Start event a timing window is opened and associated with a Stop event. The timing signal is typically shaped by a Constant Fraction Discriminator (CFD), which delivers a time of arrival

independent of its signal height. The time delay between Start and Stop events is processed in a Time-to-Amplitude Converter (TAC). Sorting into channels is performed by Analog-to-Digital Conversion (ADC) of the TAC output signal. The ADC can be read out by a microcomputer at a later time. Conventional PAC spectrometer designs require a significant amount of custom electronic circuits and complex wiring of all their components.

The goal within the context of this work was to keep the design of a new TDPAC spectrometer as simple and less laborious as possible. Like in fast-fast systems both the timing and energy information are available at the same time. But unlike conventional equipment this information is gathered from only the detector's anode output. A great deal of flexibility is introduced by using personal computer systems in combination with state-of-the-art Digital Signal Processing (DSP) technology. The PMT's anode output is being sampled digitally at high speed at all times. The main focus during the development of this new spectrometer setup was the reduction of the complexity of the electronic components. Over the last few years DSP technology has evolved and analog-to-digital recording speeds have increased tremendously. Recorderboards with sampling rates of 10^9 samples per second or more have become available. Thus, they are applicable for recording fast transient PMT signals. Photomultiplier pulse widths are typically in the order of several nanoseconds. The acquisition of several thousands of PMT signals takes place entirely inside the digitizer memory buffer. The attached computer system extracts timing and energy information and stores them. The actual evaluation of Start and Stop events can take place at any later time, as all the events are captured on a storage device. Due to the tremendous amount of data flow, it is basically just the storage space determining the length of the snapshot that can be taken of the decaying sample.

An overview of the new spectrometer setup is shown in Figure 3. Every PAC channel consists of an off-the-shelf personal computer system (Slave). Each one is equipped with a DSP board. The DSP inputs are connected to a custom-build Analog-Multiplexer board (MUX). All internal clocks of the DSP units are synchronized by a central 10 MHz reference clock network using the external clock input of the DSP board. Note that this design is basically not restricted to a certain number of channels. Due to its peer design the apparatus can theoretically be extended to an arbitrary number of channels without adding any electronic complexity to the system. The Host computer system is the supervising instance in this setup. Through an external handshaking network it monitors each Slave's state and directs their actions.

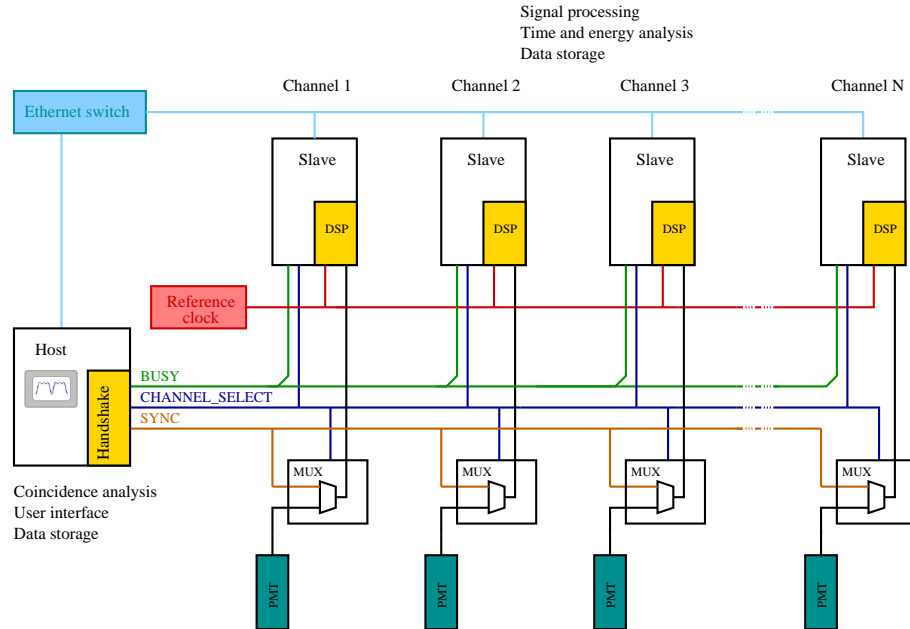


Figure 3: Functional block diagram of the PAC spectrometer. The diagram demonstrates the components of the digital PAC spectrometer design. Every PMT channel is peer to the other. The design comprises no limit to the number of total PAC channels.

While an acquisition is in progress and whenever it is convenient the Host also analyses the recorded time and energy information from the Slaves. The data is exchanged between the Host and the Slaves in a Local Area Network (LAN).

The new TDPAC spectrometer design approaches the acquisition of time-of-arrival and energy information from radiating probes more directly. The idea is to record only the PMT signal with as little electronic equipment as possible, because each additional component is known to contribute parametric errors to the measured data. Compared with conventional systems the new setup design is much simpler. The complete adjustment of a traditional PAC spectrometer is rather difficult because of its complexity. With the new approach the PMT signal is directly input to the digitizer card, which eliminates the need for external amplifier or signal conditioner units. Functions which were accomplished through electronic hardware components before are now implemented as part of the PAC software.

3.2 Handshake Bus

The operation of the PAC spectrometer is sectioned into recording cycles. During each cycle the DSP boards are triggered by pulses of the PMT anode. When the DSP memory has filled up the Slaves are forced to transfer the recorded waveforms into the main memory of the Slave. A new recording cycle is initiated immediately while the waveforms are being analyzed by the Slave. A smooth operation is arranged by the Host over a handshake bus system. A simple control network was created using the parallel port's in- and output capabilities. The Slaves need to report their state of recording to the Host computer, and the Host has to inform the Slaves to prepare their recorderboards. The principle of handshaking is illustrated in Figure 4. During the operation all Slaves are supervised and controlled by the Host. The Host cannot initiate another recording cycle as long as one of the Slaves is reporting BUSY. The Host starts a cycle by deasserting the CHANNEL_SELECT line. This action disconnects the PMT from the digitizer input. All Slaves prepare their DP110 for the upcoming recording cycle. It also informs the Slaves to prepare for the next recording cycle. As long as CHANNEL_SELECT is held low no PMT signal are routed through. By asserting their BUSY lines each Slave will notify the host that the preparation of its DSP board is complete. The Host will release a synchronization pulse after the last Slave has reported not being BUSY. The Host asserts the CHANNEL_SELECT line immediately. This action connects the PMT with the digitizer input. The Slaves will now report being BUSY until the onboard-memory of the DSP has been filled up with transient pulses. After all Slaves have transfered the waveform data from the DSP to the PC memory they will deassert their BUSY lines. The Host will then reinitiate the next recording cycle.

3.3 Standard parallel port

The signals of the Standard Parallel Port (SPP) are divided into 3 groups: Data (8 outputs), Status (5 input) and Control (4 outputs). Control and Status lines were originally designed for interface control and handshaking purposes. Eight data bits provide data from the computer to a device. Each control and data bit can be individually set or reset. Data, Control and Status bits are accessible through an I/O port. The most common base address is 0x378. In some systems this address can also be either 0x278 or 0x3bc. Usually the SPP base address can be assigned manually in the BIOS. In SPP mode the data port is write-only. Writing a byte to the base

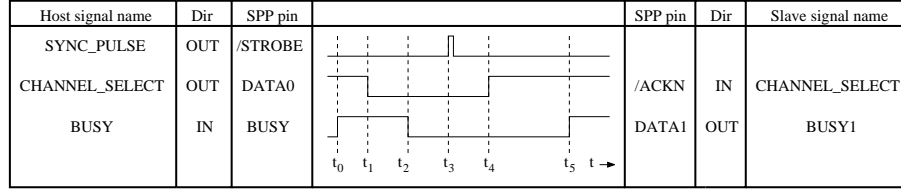


Figure 4: Handshake bus system timing diagram for a Slave/Host combination. The Slave signals to the Host that it has finished with this recording cycle at $t = t_0$. At marker $t = t_1$ the Host deasserts the CHANNEL_SELECT. The Slave arms the DSP board and acknowledges this at $t = t_2$. The Host creates the synchronization pulse at $t = t_3$. Shortly after that it asserts the CHANNEL_SELECT at $t = t_4$. t_5 symbolizes the same point in the cycle as t_0 . A low dead time is given for $t_4 - t_0 \ll t_5 - t_4$

address causes the pins to adopt either high (5 V) or low (0 V). The status port is read-only. The control port is both read- and writable. Some signals are inverted and some are low active. Table 7 in Appendix A.1 shows the pin assignment of the SPP connector [29].

The /ACKN signal is a special input pin. It is capable of being used as an interrupt source for the Programmable Interrupt Controller (PIC). A high-low transition (5V \rightarrow 0V) on the /ACKN pin triggers the PIC and causes the microprocessor to service a custom interrupt handler routine. At boot time the computer BIOS routes this signal to the PIC. This interrupt line is assigned to an integer number between 0 and 15. The typical assignment is interrupt number 7. To some extent the interrupt request number can also be assigned manually in the BIOS.

3.4 Digital Signal Processing Boards

The center piece of every PAC Slave is a fast transient recorderboard. The recorderboards used in this spectrometer setup were manufactured by a swiss company called Acqiris. Acqiris digitizers are very reliable and flexible recording devices. They are also superior in precision and accuracy [22]. Acqiris digitizers are available in two industry standards. The DP series plugs into any vacant PCI slot on a standard PC motherboard. The DC series are *CompactPCI* compliant and require an appropriate *CompactPCI* compliant crate. They are supported with a vast amount of programming libraries and interfaces. All their functionality and scope settings can be easily programmed through different ways such as LabView or C++ libraries.

The PAC spectrometer in this work features four DP110 model digitizers. The DP110

series digitizers are a basic edition with one channel probe input and one external clock input. The digitizers contain an Analog-to-Digital conversion system that is capable of recording in real-time with speeds ranging from 100 samples up to 10^9 samples per second, thus giving a timing resolution of at least 1 ns. The analog bandwidth at full sampling rate is limited to 250 MHz, meaning that fast signal components will be suppressed by an amount of >3 dB. The ADC resolution of the full scale input is 8 bit ranging from values of -128 to 127. Data from the ADC system is stored in the on-board acquisition memory. The acquisition memory has a capacity of 128 kBytes by default. An optional memory expansion to a total of 8 MBytes was installed to gain more digitizer performance.

The external clock input is used to synchronize all four digitizers to a common 10 MHz timing signal. The clock input is driven by a terminated $50\ \Omega$ line. It requires a voltage swing of at least ± 1 V to operate properly. The baseline DC-offset is programmable. The digitizers can be operated in a sequential storage mode. In this sequence mode the digitizer's memories are divided into N segments. Each segment contains n sample points. With a sample interval $t_i = 1$ ns and $n = 1000$ data points per segment each segment yields a time period of 1000 ns. On reception of a trigger event the sampling operation is started for a period of 1000 ns. The digitizer will be ready to receive the next trigger within the next following $t_p \leq 500$ ns [22]. Taken the dead time t_p , segment size n and sampling rate into account the theoretical resulting maximum detector reception rate $R_{Detector}$ yields at least

$$R_{Detector} = \frac{1}{n \cdot t_i + t_p} = \frac{1}{1000 \cdot 10^{-9} \text{ s} + 500 \cdot 10^{-9} \text{ s}} = 666 \text{ kHz.} \quad (80)$$

Figure 5 shows a plot of subsequent segments containing recorded pulses. As already mentioned, the amount of memory is limited to 8 MByte. Therefore is the maximum number of segments

$$N = 8 \text{ MByte} \cdot \frac{\text{Segments}}{1000 \text{ samples}} \approx 8000 \text{ Segments.}^4 \quad (81)$$

The acquisition stops when the maximum number of segments has been recorded. The *Pacslave* process is responsible for downloading the entire memory buffer into

⁴The present DSP configuration forbids to split the memory into more than 8000 Segments. This is a limitation that the DSP hardware puts up upon the system. Future generations might not have this limitation.

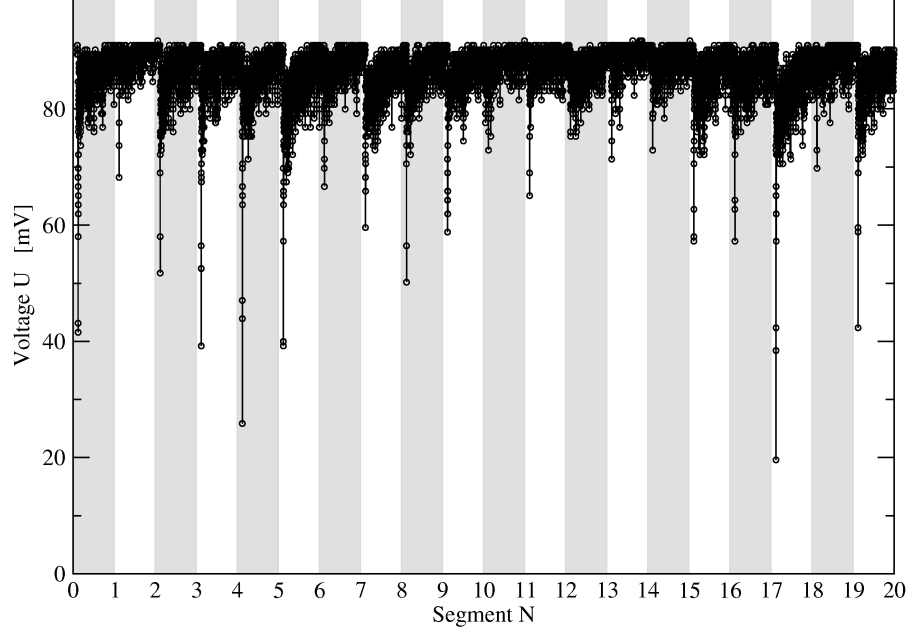


Figure 5: This graphic shows a series of subsequent segments from the PC's memory. Each segment here contains $n = 1000$ sample points.

the PC's main memory and analysing the waveforms.

While the DSP boards are recording they are considered to be online. The time they are online is defined as the time t_{online} that elapses until all 8000 segments are filled up. A dead time $t_{offline}$ exists during the data transfer to the PC mainboard. The time for one recording cycle is $t_{cycle} = t_{online} + t_{offline}$. The detector activity can be expressed as the number of trigger events per online cycle. Thus the detector activity is

$$A = \frac{m}{t_{online}} = \frac{m}{t_{cycle} - t_{offline}}. \quad (82)$$

where m is the number of segments. The duty cycle, the ratio between the online time t_{online} and the cycle time t_{cycle} , of the DSP boards are dependent of the detector activity A . The duty cycle can be expressed as follows

$$\frac{t_{online}}{t_{cycle}} = \frac{\frac{m}{t_{offline}}}{\frac{m}{t_{offline}} - A}, \quad (83)$$

where the ratio $m/t_{offline}$ can be expected to be a constant factor over the course of multiple recording cycles.

3.4.1 Scope settings

The input channel provides a fully programmable input amplifier. The probe input settings are selectable from 50 mV to 5 V full scale. At a full scale range $V_{FSR} = 200 \text{ mV}$ the recorded value of -128 would correspond to a voltage of -100 mV, 0 meaning 0 V and 127 a voltage of nearly +100 mV. The quantization increment would result in $784 \frac{\mu\text{V}}{\text{bit}}$. Some care should be taken when selecting a voltage range to allow the signal to be recorded at a maximum scale. A variable offset voltage V_O is programmable in the range of $\pm 2 \text{ V}$. The programmable offset can be regarded as a negative offset to the full scale range. V_{FSR} ranges from

$$-(V_O + \frac{V_{FSR}}{2}) \leq V_{FSR} \leq V_O + \frac{V_{FSR}}{2} \quad (84)$$

Signals outside of V_{FSR} will be clipped and should be regarded as erroneous.

Some considerations have to be taken into account when choosing the optimal scope settings. The digitizer analog input must match the impedance of a RG58 cable which connects to the MUX's output. These cables are typically rated with an impedance of $Z_0 = 50 \Omega$. In general fast transient signals could cause signal reflections which propagate back into the cable when cable impedances do not match up. Those reflections can cause multiple triggers which could lead to wrong timing information. To avoid possible signal reflections the digitizer input must be operated with its 50Ω termination turned on. As a result signal levels tend to be fairly low. Thus a reasonable sensitive input gain must be selected. Signal levels from the PMT are typically of a few mV. Hence an appropriate full scale input is programmed at $V_{FSR} = 0.2 \text{ V}$. The vertical offset is setup according to the polarity of the PMT output. The anode delivers an output signal proportional to the PMT power supply polarity. Typically a negative polarized high voltage supply is used to operate the PMT. Therefore one can expect to read a negative transient signal at the digitizer's input. In order to gain an optimal voltage range for the transient waveform the vertical offset has to be set as close as possible to the positive sampling window. An offset $V_O = 0.09 \text{ mV}$ works sufficiently for a $V_{FSR} = 0.2 \text{ V}$, giving an extra head room for determining signal levels that are out of range.

The trigger settings determine when the DSP device will start acquiring data. The trigger source is the input channel. When the input signal crosses a programmable threshold the waveform is recorded into the DSP memory. The trigger threshold

V_{thres} can be set to anywhere within V_{FSR} . The threshold also determines the trigger sensitivity. Small signals and noise can be filtered out. With a negative trigger delay time t_d the acquisition of the waveform before the actual trigger occurrence is enabled. The DSP hardware provides a timestamp for every trigger event. The timestamp is derived from the DSP's internal sampling clock. In addition it provides a horizontal positioning parameter as a correction factor for the timestamp. Trigger events usually occur asynchronously with the digitizer clock. Therefore the time between the trigger and the next sampling clock varies randomly in time. The true time reference lies within a fraction of the sampling clock. The horizontal position parameter permits a very precise positioning of the acquired trace and is necessary for the correct interpretation of the CFD's resulting parameter. The most precise trigger time is determined when the sampling clock is at maximum resolution. For the DP110 this time interval is $t_i = 1$ ns.

3.5 Host computer

The host computer is a standard state-of-the-art Personal Computer (PC). The host system is equipped with an ASUS motherboard (Parallel port, serial port, USB, PCI), a 3.2 GHz Intel hyperthreaded microprocessor, 512 MB of RAM, a 1 Gbit network card and 80 GB harddrive. The main function of the host computer's hardware is to control all participating slave computers. This is done through a series of status lines that lead from each slave computer to the host computer's parallel port, as the parallel port offers some convenient way to use its logic inputs. Further, since all machines are linked together by a local network switch, the host is able to submit commands to, and query settings from the slave over a TCP connection. The host computer switches all analog MUX boards to the sync pulse input channel. Then it sends a signal to each slave to prepare their recorderboards for a measurement cycle by switching its outgoing status lines. It waits until all slave computers respond with an acknowledge signal. Immediately after all Slaves have reported being armed it releases the sync pulse and switches the analog MUX boards to the PMT input channel. From now on the host monitors the status of the Slaves until all of them are finished recording. This cycle repeats continuously until the measurement is finished.

3.6 Slave computers

At this point of development of the PAC spectrometer there are 4 slave computers involved in the acquisition of event data. For symmetrical reasons 4 identical Personal Computer configurations were chosen. Each system features a state-of-the-art motherboard with a 2.8 GHz AMD Athlon microprocessor, 512 MB of RAM, a 100 Mbit network adapter and 80 GB harddrive. Note that there are practically no limitations on the harddisk space. Each slave is equipped with an Acqiris DP110 transient recorder board in one of its 32 bit PCI slots. A PAC slave computer is responsible for configuring the recorderboards such as setting up the input gain, trigger threshold and trigger slope, memory usage, sample intervals, etc. The Slaves download the data from the recorderboards once a recording cycle is finished. Their main purpose is to analyse the recorded waveform data, primarily extracting information such as photon energy and time of arrival. Instead of storing the entire waveform only a few parameters are permanently stored on the harddrive. For practical reasons the waveforms are generally discarded after the analysis. This saves quite a bit of harddisk space. Typically the harddisk space of a slave is filling up according to the trigger repetition at a rate of several thousands per seconds.

3.7 Analog multiplexer module

The center piece of the analog multiplexer module is an AD8180 from Analog Devices. The AD8180 is a high-speed 2-to-1 integrated analog multiplexer circuit. The functional block diagram is shown in Figure 6. It is designed as a high-speed analog signal switch and offers a -3 dB signal bandwidth for frequencies greater than 750 MHz. The crosstalk between the two channels is specified to be as low as 80 dB [23]. Switching happens upon the change of the logic input level at its SELECT input. When SELECT is logic low the common output AOUT equals the analog input IN1, otherwise AOUT equals IN2. The MUX is necessary for synchronizing the timestamps of all Slaves. This is achieved by switching the MUX's first input IN1 to its output AOUT. As shown in Figure A.3.2 in Appendix A.3, IN1 is connected to the synchronization module output. The two resistors R7 and R11 and the capacitance C6 form a derivative element which transforms the incoming logic pulse edge from U2 into a short pulse. Due to extreme precise timing requirements the pulse edge is required to be as steep as possible. Therefore the choice of the relatively small pull-down resistor value ($R11 = 25 \Omega$) and the small capacitance ($C6 = 47 \text{ pF}$) seemed appropriate. During

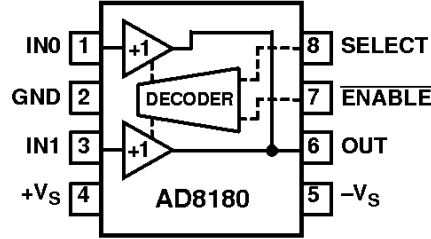


Figure 6: Functional block diagram of the 2-channel analog multiplexer circuit AD8180 from Analog Devices which is used on the MUX module.

the synchronization state the host holds the SELECT input signal low. Then the host initiates the TRIGGER pulse and immediately switches the MUX to the second input IN2 where from now on PMT pulses are getting to the SIGOUT output. This procedure ensures that the digitizers record their first pulse from which is known it has been generated from a single source. Since the pulse arrived at all digitizer units at a common time, the first timestamp can be regarded as a reference to following timestamps.

In addition to switching the multiplexer channels, the SELECT signal is also connected to the Slave's parallel port /ACKN input (X1 Pin 10). Upon the transition from high to low the slave is also notified through the parallel ports interrupt, that the host has put the spectrometer into the synchronization state. This interrupt event is received by the Linux kernel driver. A more detailed description can be found under section 4.

3.8 Reference clock distributor

A common clock source is required to operate the external clock input of the four digitizers. In order to stay synchronized throughout the measurement the digitizers require a fixed frequency of 10 MHz. The output signal of a high-precision quartz oscillator can be used for that purpose. The voltage level swing of The digitizer's external clock input requires at least an order of ± 1 V voltage level swing. The external clock input is terminated internally by a 50 Ω resistor. The clock source must be able to drive the 50 Ω impedance line to provide the required voltage swing. Therefore the oscillator output is amplified by an integrated line driver circuit. Its output signal is passed through a capacitor to remove any DC offset in the clock signal. The capacitors value matches the cable impedance at a nominal frequency of

10 MHz.

Figure A.3.4 in Appendix A.3 shows the schematic diagram of the common clock driver design. A quartz oscillator from ECS 3951 series with a nominal frequency of 10.000 MHz serves as the clock source. It is rated with a frequency stability of ± 50 ppm [24]. On the first prototype board the output is split up into four paths which leads to the input of the high speed line driver integrated circuit. The type of line driver used here is a DS26LS31 from National Semiconductors. It is a common type line driver used in several high speed interface applications such as RS422/RS458 or Ethernet 801.3 [25].

3.9 Synchronization and Channel Select fanout module

The Synchronization and Channel-Select (SCS) fanout module is the bridge from the Host's parallel port to the Slave's analog Multiplexer module. It conditions the handshake and synchronization signals to be transmitted over a RG58 cable. The module also features an integrated line driver circuit [25] which transduces the low power outputs of the SPP into four $50\ \Omega$ impedance lines. A resistor in series with the output matches the output impedance to the cable impedance. This is required to ensure the signal strength at the receiver is maintained and reflections in the cable are suppressed. The schematic diagram in Figure A.3.3 in Appendix A.3 shows the CHANNEL_SELECT bus signal driven by DATA0. /STROBE drives the SYNC_PULSE line. Both signals are fanned out into four channels.

3.10 Photomultipliers

Photomultiplier tubes are extremely sensitive detectors of light in the ultraviolet, visible and near infrared. These detectors multiply the incident light by an amount of as much as 10^8 . Even single photons can be resolved. The incident photon strikes a highly negatively charged photosensitive cathode and releases electrons as the consequence of the photoelectric effect. These electrons are directed through a focusing electrode towards a cascade of electron multiplying dynodes. The process of secondary electron emission leads to a measurable amount of electrons at the last instance of the cascade. All electrons are collected at the positively charged anode. The integral of the anode signal is proportional to the energy of the incident photon. The amount of multiplied electrons rescinds the amount of positive charges at the anode

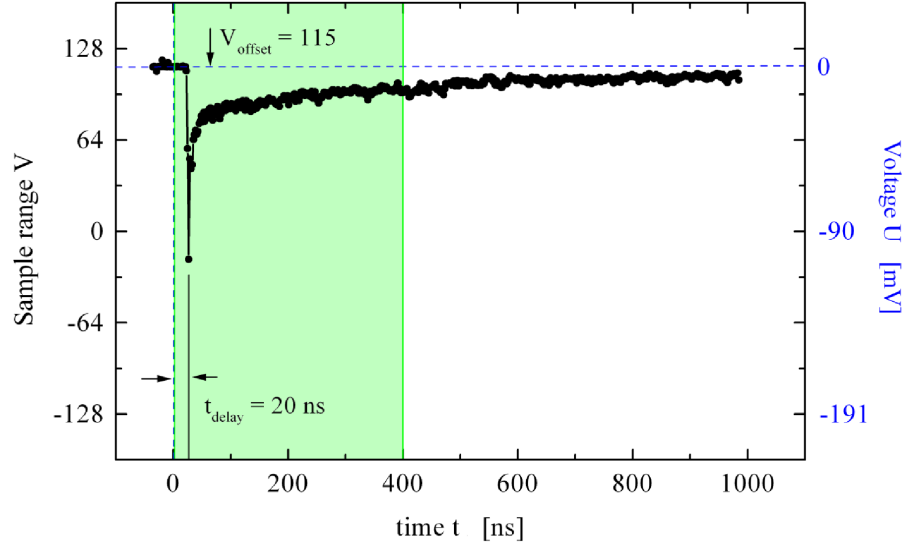


Figure 7: Single transient pulse as recorded by the DP110 digitizer board. In this sample segment the trigger delay is set to $-20 \cdot 10^{-9}$ s. The DC base line is set to $115 = 0$ mV. The shaded area of 400 sample points signifies the minimum portion necessary for reasonably good energy determination. The left ordinate represents the sample points in signed 8 bit. The right ordinate represents the sample points in mV.

and therefore appears as a negative pulse at the output. Figure 7 shows a single transient pulse as it was recorded from the PMT anode. For the conversion of higher energy γ -rays into light pulses a scintillator crystal is mounted in front of the optical window of the PMT. The two most common types of scintillator materials are BaF_2 and Titanium-doped NaI. BaF_2 detectors are used more often instead of NaI because of their higher timing resolution, even though their energy resolution is 30% less than for NaI. The PMTs used in this work are equipped with cylindrical BaF_2 crystals with a size of 1.5" in diameter and length. The tube's of type Hamamatsu R2059 operating voltage is rated between -2.0 kV and -3.0 kV [26].

4 Software

Software applications are the most vital part of this PAC spectrometer. The spectrometer is controlled and operated by Host and Slave software applications. The Host is the controlling instance of the setup. The Host demands control over the measurement and carries out all supervising tasks. Slave applications are distributed processes which are performing helper tasks on the Slave computers. Both Host and Slave applications are using the computer hardware resources. An application running on a Linux system can gain access to the computer's hardware through a device driver. The device driver intervenes with the computer's hardware resources. A device driver in the world of Linux is called a kernel module.

4.1 Parallel port device driver

The kernel module *pacmod.o* claims access over the parallel port hardware. It handles two character devices, thus giving access for user level applications to use the parallel port. On the system it provides the two device names */dev/pac0* and */dev/pac1*. Read and write operations can be performed to either one of these device names. Reading from the device retrieves a status word about the logic state of the parallel port input pins. Writing to the device sets the parallel port output pins. The kernel module *pacmod.o* is installed on all Host and Slave computers.

4.1.1 Installing the device driver

Two nodes must be created before it is safe to install the module. Under Linux a device node is identified by a unique major resource identifier. A minor id helps to distinguish between a multiple number of device names such as */dev/pac0* and */dev/pac1*. More information about kernel mode device drivers can be found in [30, 31]. The following command creates two character devices:

```
$ mknod /dev/pac0 c 254 0
$ mknod /dev/pac1 c 254 1
```

After these nodes have been created the module can be installed. While installing the module two additional kernel parameters can be provided: the base address and the interrupt number. The most typical values for these values are 0x378 and 7, but in

general they depend on the BIOS settings. The following command loads the module into the kernel:

```
$ insmod pacmod.o lptIOBase=0x378 lptIrq=7
```

Whether the module has been loaded properly can be checked with

```
$ lsmod
```

The module can be removed again by the command

```
$ rmmod pacmod
```

4.1.2 Using the device driver from the console

For testing purposes the device driver can be communicated with by sending commands over the console using the *echo* command. A set of command strings are described in the Appendix A.4.3. The following two command lines manually switch between the MUX channels.

```
$ echo cp > /dev/pac0
$ echo cs > /dev/pac0
```

4.1.3 Using the device driver in a C/C++ application

A C/C++ application can use in- and output functions from the standard I/O library. The following example in C shows how a read and a write operation is executed with the kernel driver:

```
#include <stdio.h>

int main( int argc, char* argv[] )
{
    FILE* f = fopen( "/dev/pac0", "r+" );

    if( f )
    {
        int status;

        // Read an integer from the file handle.
    }
}
```

```

        // It holds the interrupt request flag in the 1st
        // byte and the parallel port status word in the
        // 2nd byte.
        fread( &status, sizeof(status), 1, f );

        // Load the command word.
        int command = __PACMOD_PMT;

        // Write the command to the device.
        fwrite( &command, sizeof(command), 1, f );

        fclose( f );
    }

    return 0;
}

```

A file handle is created by the C function call *fopen()*. The *fread()* function returns the parallel port status in the integer variable *status*. The information is aligned as follows:

Bit 0	Interrupt flag
Bit 1..7	reserved (= 0)
Bit 8..15	Parallel port status (See Table A.8 for details)
Bit 15..31	reserved (= 0)

The *fwrite()* function call sends a command word to the device driver. The commands are predefined in the project header file *pacmod.h*. All implemented commands and their descriptions are shown in Table 3.

4.2 Slave applications

4.2.1 Pacslave

The slave process *Pacslave* performs operational tasks of the Slave computers. It provides a TCP/IP server socket for the Host application to connect to over the local area network. The server socket is listening on port 15000. It was designated for the exchange of project settings between the Host and the Slaves. *Pacslave* interfaces with the handshake bus and drives the Slave's logic signals. However, the main task

Command definition	Description
PACMOD_TRIGGER	Create sync pulse on /STROBE
PACMOD_SYNC	Switch MUX to sync channel. Deasserts DATA0
PACMOD_PMT	Switch MUX to anode channel. Assert DATA0
PACMOD_DATA_SET	Set bit in parallel ports DATA register
PACMOD_DATA_RESET	Reset bit in parallel ports DATA register

Table 3: List of command declarations which are currently implemented in the *pacmod* kernel module source.

of *Pacslave* is to manage the DSP hardware. It prepares the DSP acquisition cycles as commanded by the Host. The chart in Figure 10 *a.*) shows the program flow of *Pacslave*.

The DSP cards are supported by programming libraries which have been provided by the manufacturer. The libraries give access to the DSP card settings and are utilized by *Pacslave*. *Pacslave* analyzes the formerly acquired data parallel to the digitizer's recording cycle, so that no overhead time is demanded for the analysis task. It accumulates a time and energy stamp from each segment and stores this information on the harddisk. The timestamp information is more or less already provided by the DSP boards trigger mechanism in form of a 64-bit integer variable in units of 10^{-12} s. However, the precise time of flight t_{tof} is often depending of the signal height of the incoming pulse. A technique, called constant fraction discrimination, delivers the trigger time independent of the signal height. In conventional PAC setups this technique is applied to the PMT signal by external electronic hardware. In this spectrometer setup it has been replaced by pulse analysis routines implemented into *Pacslave*. The source code was developed to utilize the anode signal of the PMT to perform energy and time extraction. The anode signal can be separated into two fractions, the fast and the slow component [20, 21]. It was found that the slope of the fast component of the anode signal had a rise time of about 3 ns and a decay time of 4–5 ns and could be expressed through a Gaussian distribution. The shape of the fast component was found to be extremely suitable for the CFD technique. Figure 8

displays in detail how the technique is applied to the waveform. The PMT pulse is recorded with a pre-delay of $t_d = -20 \cdot 10^{-12}$ s. This moves the trigger point well into the recording window so that the CFD technique can be applied. The fast component is first inverted, divided in half and added to the original fast component data by an offset of less than the FWHM of the fast component. The zero-crossing point t_{cfd} is independent of the original signal height. t_{tof} can now be correctly appraised under consideration of the timestamp t_{ts} , the horizontal position parameter t_{horPos} , and the zero-crossing point t_{cfd} by the formula

$$t_{tof} = t_{ts} - t_{horPos} + t_{cfd}. \quad (85)$$

The horizontal position parameter t_{horPos} is a correction factor for the DSP horizontal parameters. This value is provided by the DSP hardware. Trigger events usually occur asynchronously with the digitizer clock. Therefore, the time between the trigger and the next sampling clock varies randomly in time. The true time reference lies within a fraction of the sampling clock. The horizontal position parameter permits a very precise positioning of the acquired trace and is necessary for the correct interpretation of the CFDs resulting parameter.

As an example the variations in t_{cfd} for the isotope $^{181}\text{Hf}(\text{Ta})$ are demonstrated in Figure 9. $^{181}\text{Hf}(\text{Ta})$ has three distinct energy peaks that are useful to show the relationship of the photon energy and the time of arrival. On average the timestamps for lower energies are corrected toward shorter times, as they tend to be detected at a later time. Higher energies appear to be detected at earlier times and therefore their correction term is towards larger times. The CFD technique was applied on transient waveforms of the BaF_2 detector's fast component. In addition the waveforms were filtered according to their energy integral. Only those γ -rays which fell into the energy windows were regarded. On average the lower energy γ -rays are detected later than the higher energy γ -rays. The first 136 keV appears to arrive about 800 ps later than the second 384 keV. And the third 481 keV arrives even earlier than the second by almost 400 ps. The application of the CFD technique also yields to the identification of false trigger events. If the shape of the recorded transient deviates from a certain average this segment is disregarded.

The energy can be determined by integrating the signal over the entire length of the segment. The tail of the pulse, the slow component, typically decays within several hundred nanoseconds. Its integral contains most of the energy information.

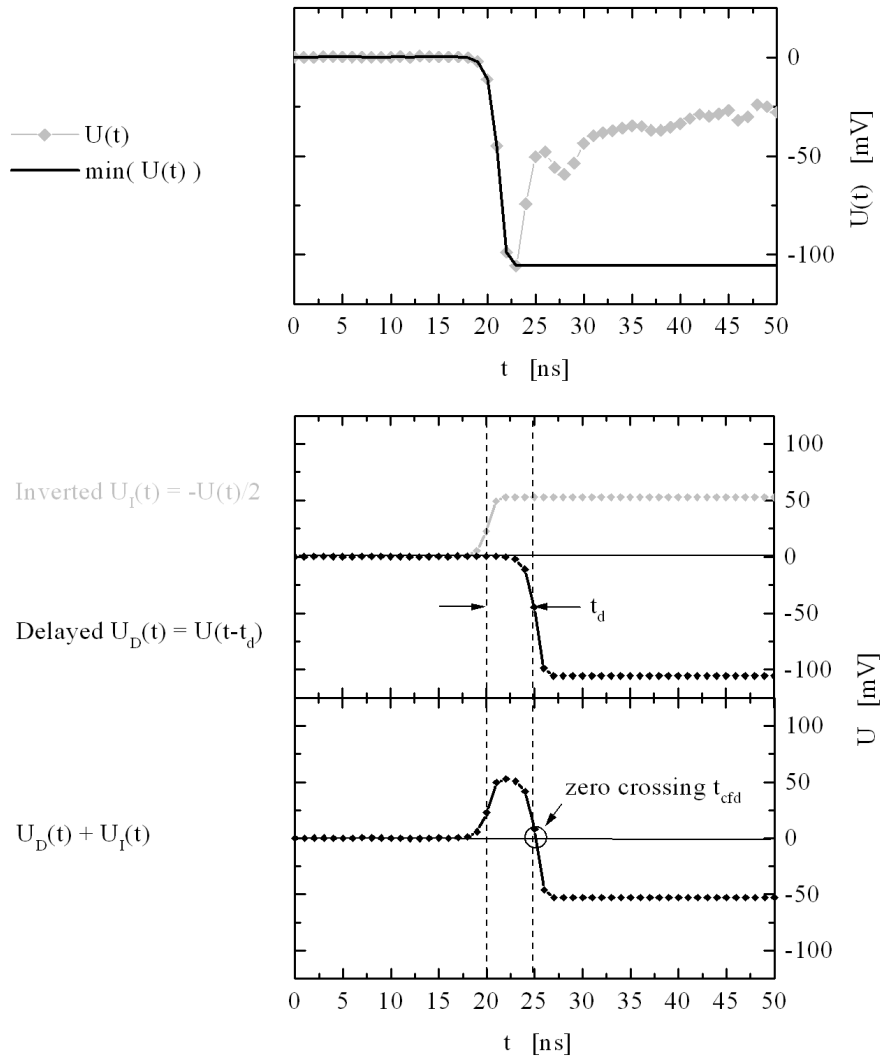


Figure 8: Illustration of the software-based CFD technique applied on a transient waveform. The slope of the BaF₂ detector's fast component is used for the corrections on the time of arrival. The zero-crossing point t_{cfd} is independent of the signal height.

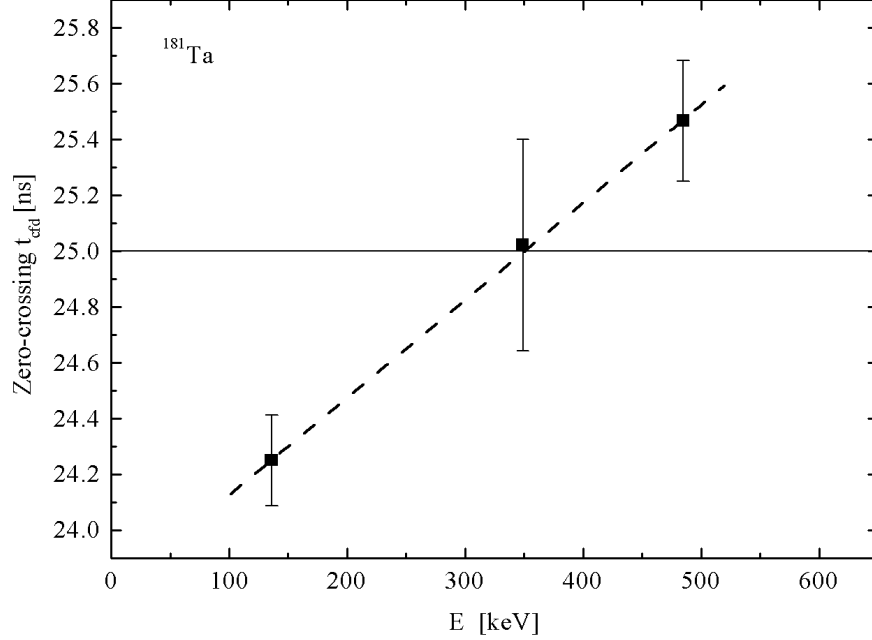


Figure 9: Results of the CFD technique applied on the three energy peaks of $^{181}\text{Hf}(\text{Ta})$. On average lower energies appear to be detected at later times than higher energies. The data points represent the zero-crossing times t_{cfd} by which the actual timestamps have to be corrected.

For practical reasons the segment size is set 400 samples thus giving the maximum number of recordable number of segments of 8000. Furthermore, by using Eq. (80) this yields to a maximum possible repetition rate of 833 kHz. Test runs have shown that this theoretical reception rates can be achieved by the electronic system. In practice the limiting factor is by far the PMT. When the incident photon flux is too high the anode saturates and the trigger slope cannot be identified sufficiently.

After the fitting process is completed for all segments the results: the energy integral number, the timestamp, and the CFD factors are stored in sequence files. A discription of the sequence files is given in Section 4.2.3. With every new sequence the sequence counter is increased. The file name reflects the sequence counter value. A set of files with the same sequence number possesses a chronological relationship. The synchronization pulse is typically the first segment recorded by the DSP board. Because of its unique shape it can be easily identified as a valid reference point. Therefore, the first entry in a sequence file represents this reference point. Within a set of sequences the *Cocheck* process will later look for coinciding events. See Section

4.3.2 for more details.

4.2.2 Pacslave options

In order to work with the DSP cards correctly *Pacslave* must be provided with the right set of options. Each PAC channel has its individual set of parameters. The full scale range V_{FSR} default value is 200 mV with a vertical offset of $V_{Off} = +90 \text{ mV}$. The trigger threshold must be adjusted individually according to the PMT gain. A trigger delay of $t_d = -20 \cdot 10^{-9} \text{ s}$ proved to be sufficient for the trigger time analysis. The configuration for each PAC channel is stored in the file *pacslave.conf*. The file is located in the project folders */etc* directory.

Pacslave can be given a set of command line options. Any option specified on startup overrides its default value. The set of command line options and the content of the configuration file can be found under Appendix A.4.1.

The following is an example of how to start *Pacslave* with an input gain of 0.2 V full scale, an offset of +0.09 V, a negative trigger slope and a trigger level at 50 mV the command line would look like this:

```
$ pacslave -a1 -v0.2 -o0.09 -ts1 -tl40 -s400 -S8000
```

The number of segments per recording cycle is set to 8000. Each segments holds 400 sample points.

4.2.3 Pacslave file format

This is a discription of the file format used by *Pacslave* to store the fitting parameters. The file name is composed of the PAC channel number n_{ch} and a 6 digit sequence number n_{seq} plus the extension *.seq*. A 4-channel spectrometer would produce chronologically related files with names 1000100.seq, 2000100.seq, 3000100.seq, and 4000100.seq, where $n_{seq} = 100$. In general sequence files contain ASCII text. Labels are introduced by *#* sign at the beginning of every line. A label represents the beginning of a series of arguments. Arguments can be any kind of number types or string types. The header of the 1000100.seq file looks like

```
# WAVEFORM 0 100 7041
# DATE 1136248918 Tue Jan 3 01:41:58 2006
# TEMPERATURE 38
# SEGMENT 0 5834283940 0 -439 1415
```

```
# SEGMENT 1 9791467276 913 -775 1755
# SEGMENT 2 12821855718 961 -217 1172
# SEGMENT 3 15789855866 948 -365 1320
# SEGMENT 4 ... .
```

where the interpretation of the labels is

```
# WAVEFORM <pac channel> <sequence> <segments>
# DATE <unix time> <date and time string>
# TEMPERATURE <degree C>
# SEGMENT <n> <timestamp> <energy> <horPos> <cfid value>
```

The first line designates the file type. The WAVEFORM label signifies that this is a sequence file. It has three arguments. The first <pac channel> entry is a zero-based index of the PAC channel number. The second entry is the sequence number. The third argument is the total number of segments this file contains. The DATE label represents the Unix time as an integer value and as a string. TEMPERATURE gives the current temperature of the DSP board in units of °C. The parameters that were obtained from the analysis are kept under the SEGMENT label. This is mainly a 64-bit wide timestamp in units of ps. The energy integral is an arbitrary value. In the first SEGMENT line the energy value has a special meaning. The timestamp identifies a valid synchronization pulse when it is equal to zero. A non-zero value represents an invalid entry.

4.3 Host applications

4.3.1 Pachost

The host application *Pachost* is a helper process which controls the operational flow of all Slaves during a recording cycle. When *Pachost* is invoked it connects itself with all Slaves over the local area network. It evaluates its configuration and sets up the Slaves. With the beginning of a new measurement *Pachost* will deliver the project settings to the Slaves, such as the project name and date and time when the measurement was started, etc. The final step is to initialize the handshake bus before assuming operation. The diagram in Figure 10 *b.*) depicts the application flow of the host process. *Pachost* requires the following arguments at minimum.

```
$ pachost <first sequence> <last sequence> [options]
```

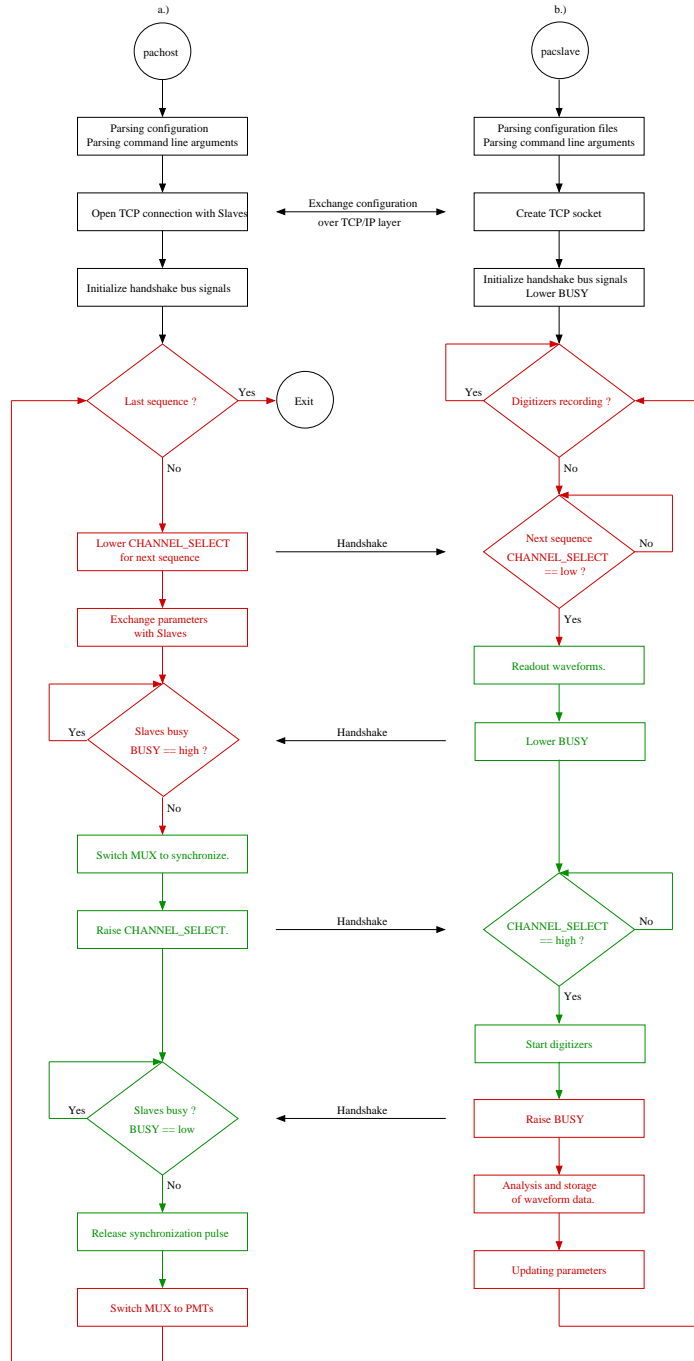


Figure 10: Flow chart for the PAC processes during the recording cycles of the PAC spectrometer. Depicted in the left column is the program flow for the *Pachost* process, on the right the program flow for *Pacslave*. The arrows in the center denote the inter-communication messaging between those two processes.

The first argument specifies the number of the first sequence file. The second argument specifies the number of the last sequence file. The measurement will stop immediately after the last sequence file was written by *Pacslave*. *Pachost* will exit after completion of the last recording cycle.

4.3.2 Cocheck

For each PAC Slave exists a set of sequence files containing segments with timestamp and energy information. The sequence files must be analyzed for coincidences. *Cocheck* is the next instance in the series of PAC helper applications that puts the recorded data through energy and coincidence filters. All events are divided into Start and Stop events according to the energy window settings. The energy values are arbitrary integral numbers that are usually sorted into arrays which then reflect the energy spectrum. Figure 11 shows three typical energy spectra for $^{181}\text{Hf}(\text{Ta})$, $^{111}\text{In}(\text{Cd})$, and ^{22}Na as recorded by the PAC spectrometer. The energy windows for Start and Stop are depicted as shaded areas. Segments with energies that fall beyond the energy windows are discarded. The remaining segments are put through a coincidence perceiving routine, which searches for coincidences in every PAC Slave combination. Options and the configuration file are listed in Appendix A.4.5.

The coincidence algorithm is a nested loop that cycles through all Start/Stop permutations to create the time spectra $D_{ij}(t)$, where i is the index of the Start channel and j the index of the Stop channel. The algorithm will skip combinations of $i = j$. Therefore the total number of time spectra created is $m = n(n - 1)$ with $n =$ number of PAC channels. For a 4-channel PAC spectrometer this yields to 12 different time spectra or 30 time spectra for a 6-channel setup. With $N =$ average number of segments the complexity of the algorithm can be classified as $O(N\sqrt{m})$.

The common timing reference between all PAC Slaves is the timestamp of the first segment. In general the timestamps of the DSP cards have no relationship with respect to each other. Though running coherently the DSP internal clocks are running independently. The reason for the Host inserting the synchronization pulse is the provision of a common timebase. Every Slave is recording the synchronization pulse first before switching over to the PMT channel. If the energy integral of the first segment is of zero value, the corresponding timestamp represents the chronological origin t_{n0} . Thus within a segment, subsequent timestamps t_{nk} need to be converted into absolute timestamps with respect to t_{n0} . Coinciding events can hence be found

among absolute timestamps. The Start and Stop are collected into time spectra $D_{ij}(t)$ according to formula

$$\Delta t_{ijk} = (t_{jk} - t_{j0}) - (t_{ik} - t_{i0}) + \frac{t_{max}}{2} \quad (86)$$

$$D_{ij}(\Delta t_{ijk}) = \begin{cases} D_{ij}(\Delta t_{ijk}) + 1 & \text{if } 0 \leq \Delta t_{ijk} < sizeof(D_{ij}) \\ D_{ij}(\Delta t_{ijk}) & \text{otherwise ,} \end{cases} \quad (87)$$

where the indices i and j are permutations of the PAC Slaves and $sizeof(D_{ij})$ the size of the D_{ij} array. The factor $\frac{t_{max}}{2}$ in Eq. (86) shifts the time spectrums center point t_0 into the mid-range of the array. Figure 12 in Section 5.2 shows such a typical a time spectrum with the prompt peak located in the center of the graph.

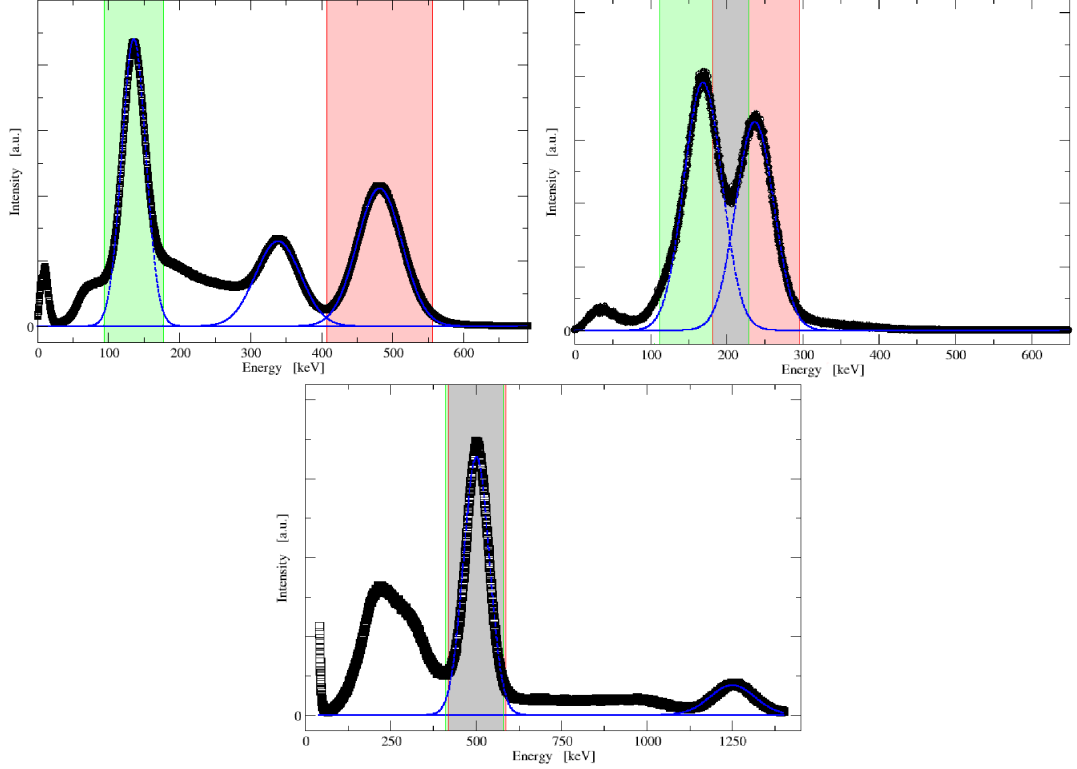


Figure 11: Three plots showing the decay energy spectrum of *a.*) $^{181}\text{Hf}(\text{Ta})$, *b.*) $^{111}\text{In}(\text{Cd})$, and *c.*) ^{22}Na . The horizontal energy axis is scaled down to match the significant energy peaks. The Start window is marked through the shaded green area, the Stop window is marked through the shaded red area. The 511 keV peak of the Sodium sample is marked by both the Start and Stop window. This peak appears through a e^+e^- annihilation process in Sodium, where two γ -rays are emitted in opposite directions at the same time. The detection by two opposite PMT tubes can be used for calibration purposes of the PAC setup.

4.3.3 Cocheck file format

The time spectra are saved in files *dij.dat*. *i* and *j* represent permutations of the PAC channel numbers. The file format contains a header followed by a two-column data field. The first column is the running index of the slot. The second one holds the number of coincidence counts. The columns are separated by the `<tab>` character. The header is designed like this:

```
# DIJ <i> <j> <number of data lines>
# <next sequence> <last sequence> <max count> <time scale>
  <diff. unix time>
# MAX <max count>
```

```

# CENTER <slot of tzero>
# TIMESCALE <time scale> ps
0      567
1      553
2      532
3      ...

```

The DIJ label is a designator for file type. i and j are zero-based indices of the PAC channel combination. The third argument gives the total number of slots. The MAX, CENTER, and TIMESCALE labels hold the maximum number of coincidence counts, the center slot index, and the time base in units of 10^{-12} s.

4.4 Network File System

File folders are shared among the Host and the Slaves over the **Network File System**. The Slaves export their data directories to the NFS. The Host gets access to them by mounting the exported data directory into its own file system. On the Host side each mount point is constructed as `/mnt/pac<n>/data/<projectname>`, where n is the index of the PAC channel and `<projectname>` the path to the measurements data directory, respectively.

5 Experiments

5.1 Host and Slave Preparation

Before an acquisition cycle can start the spectrometer elements have to be configured. This involves mainly the preparation of the configuration files for the *Pacslave*, *Pachost*, and *Cocheck* processes. Every measurement requires its specific set of configuration files. The *Pacslave* process uses the provided information in file *pacslave.conf* to prepare the DSP cards accordingly. It receives information about electrical properties of the PMTs that are specific for this kind of experiment. Additional project information, such as project path and network port, is also provided. Table 4 contains a summary of the default options for the *Pacslave* process. Once the *Pacslave* process is started on each of the Slave computers, it listens on a network port for the *Pachost* process to connect.

When the *Pachost* process is executed the project configuration file *pachost.conf* is loaded. The configuration file was setup specifically for the measurement and contains information about general project settings, such as project path and the Slave computer IP addresses. *Pachost* opens up the network ports to the listening *Pacslave* processes and negotiates the preparation for the measurement with them. When the acquisition cycle begins, the *Pachost* process supervises the measurement and the *Pacslave* processes constantly log the energy spectra and time of arrival into the specified project path.

Both the energy spectra and timestamps are available during the measurement, so that the *Cocheck* process can be started any time during the acquisition cycle. The *Cocheck* process generates the energy spectra from the gathered information. The operator can adjust the Start and Stop energy windows according to each channel's energy spectrum individually. *Cocheck* will search for coinciding timestamps and will build the count rate spectra with the help of the Start and Stop window settings. Note that no calibration of any electronic component is necessary.

5.2 Data Processing

During the performance of a PAC experiment, the *Pacslave* processes collect γ -ray information during the decay of the isotope. The time of arrival and energy of the γ -radiation is stored on the storage medium. At this time neither energy nor time discrimination is performed on the raw data. Basically, a snapshot is taken of the

Global setting [unit]	Value
Full scale [mV]	200
Offset [mV]	90
Input coupling [Ω DC]	50
Trigger slope	negative
Trigger delay [s]	$-20 \cdot 10^{-12}$
PMT signal	Anode
Listening IP port	15000
Project path	(to be determined upon start)
Individual setting	Description
IP address	192.168.0.<number of slave pc>
Trigger threshold	Depending on PMT type and power setting
Energy windows	Individual, if applicable. Typically, energy windows are set to filter γ_1 and γ_2 .

Table 4: A list of *Pacslave*'s default settings.

isotopes decay, which is available for analysis later at any given time. The overwhelmingly large amount of data has to be reduced in following data reduction steps. For instance, a typical PAC experiment for 8 hours with a 4 detector setups and $40 \cdot 10^3$ registered events per second gathers roughly 60 GB of data. The *Cocheck* process applies Start and Stop windows, and searches for segments that coincide with time and energy. Random coincidences that do not fall within these windows are discarded for memory conservation purposes.

The raw coincidence data of the new collection method can contain count rates in any arbitrary time interval resolution. These time interval widths are primarily limited by the DSP hardware. Depending on the half life of the decaying process and strength of perturbation the time interval width are typically be set somewhere between 100

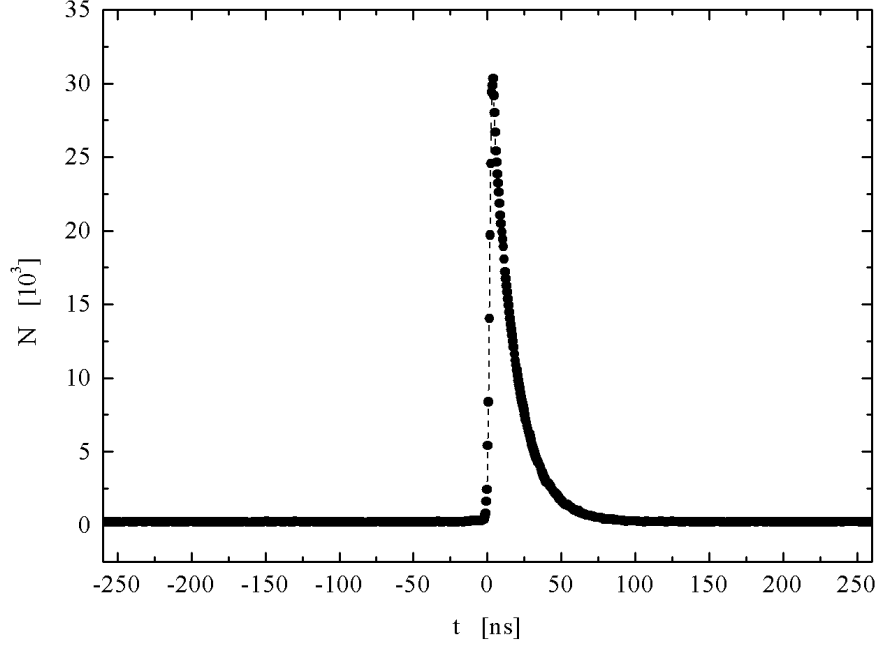


Figure 12: Time spectrum of a detector pair observing the Start and Stop γ 's of an intermediate nuclear state. For negative times the random background count is evenly distributed. At t_0 the coincidence count rate rises instantly. For positive times the coincidence peak decays according to an exponential function with the half life of the intermediate state. For larger positive times only the random background remains.

ps and 1 ns. Theoretically, there is also no limit in size of the observable time window. In this work the spectrometer was set up to search for coincidences within an 8 μ s window. Figure 12 shows a typical time spectrum. The prompt peak for each detector pair i,j is typically located about the center of the spectrum $t_{0,ij}$. Using the wide data range available left and right of $t_{0,ij}$, it is possible to determine the average background B_{ij} very accurately. In addition, the high time interval resolution supports the determination of the exact location of $t_{0,ij}$. The knowledge of both, the horizontal location of the time spectra and the average background, is important in the process of obtaining the perturbation function.

Given a sample with activity N , every detector i registers a sample activity proportional to $N_i = \varepsilon_i \Omega_i N$, with $N = e^{-t/\tau} N_0$ and τ is the decay time of the nucleus. ε_i describes the single detector response efficiency and Ω_i is the fraction of the solid angle. Not every γ -ray that enters a detector represents necessarily a Start event. Also, dark noise effects inside the detector, such as thermal electrons, may induce a

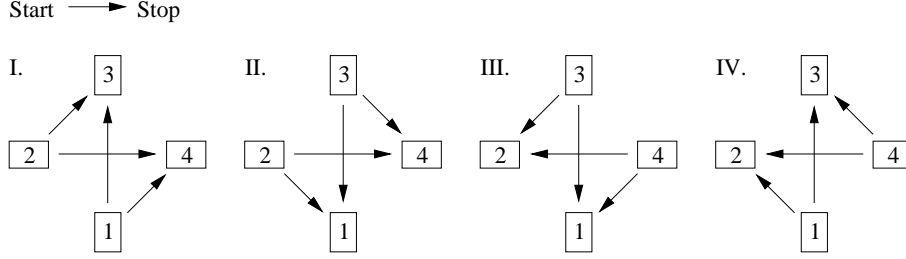


Figure 13: Conventional Start-Stop arrangements for the 4 channel acquisition system. The 12 time spectra can be systematically combined to achieve at least the 4 conventional PAC count ratios I – IV.

trigger signal. Therefore, the probability detecting a Start event in detector i can be weighted by a value κ_i . The probability of detecting a Stop event after successfully detecting a Start event can be measured in terms of the half life τ_N of the intermediate state. Values for τ_N for the used isotopes in this work, respectively, are given in Tables 1 and 2.

For each detector pair i,j the raw data contents can be expressed as

$$D_{ij}(\theta, t) = \varepsilon_i \varepsilon_j \kappa_i \frac{e^{-t/\tau_N}}{\tau_N} e^{-t/\tau} N_0 W(\theta, t) + B_{ij}. \quad (88)$$

$W(\theta, t)$ is the angular correlation function (35). The average background count B_{ij} is a constant fraction due to random coincidences collected by the spectrometer. For times t that are much shorter than the half life time of the nucleus, the term $e^{-t/\tau} \approx 1$. For large t the count rate is $D_{ij}(\theta, t) = B_{ij}$. The background-corrected count rate is

$$N_{ij}(\theta, t) = D_{ij}(\theta, t) - B_{ij} = \varepsilon_i \varepsilon_j \kappa_i \frac{e^{-t/\tau_N}}{\tau_N} N_0 W(\theta, t). \quad (89)$$

The present 4-detector setup provides a set of 12 time spectra, four 180° and eight 90° spectra. Figure 13 depicts all the conventional detector pairings which can be constructed from the pool of the 12 time spectra. The 12 spectra can systematically be combined, so that 4 different conventional count ratios can be built. These used to be referred to in literature as the two forward (I. + II.) and two backward (III. + IV.) count ratios.

In order to separate the perturbation function $W(\theta, t)$ from Eq. (89) the following

count rate ratio $Z_0(t)$ is constructed from the individual count rates $N(\theta, t)$:

$$\begin{aligned}
 Z(t) &= \frac{N_{02}(180^\circ, t) N_{13}(180^\circ, t)}{N_{03}(90^\circ, t) N_{12}(90^\circ, t)} = \\
 &= \frac{\kappa_0 \kappa_1 \varepsilon_0 \varepsilon_1 \varepsilon_2 \varepsilon_3 \frac{e^{-t/\tau_N}}{\tau_N} N_0 W^2(180^\circ, t)}{\kappa_0 \kappa_1 \varepsilon_0 \varepsilon_1 \varepsilon_2 \varepsilon_3 \frac{e^{-t/\tau_N}}{\tau_N} N_0 W^2(90^\circ, t)} = \\
 &= \frac{W^2(180^\circ, t)}{W^2(90^\circ, t)}. \tag{90}
 \end{aligned}$$

Note that all, in general unknown efficiencies cancel each other. However, if the 180° and 90° count rates are arbitrarily combined, the terms ε_i and κ_i might not necessarily vanish. For instance is

$$Z_{12}(t) = \frac{N_{02}(180^\circ, t) N_{13}(180^\circ, t)}{N_{01}(90^\circ, t) N_{23}(90^\circ, t)} = \frac{\kappa_1 W^2(180^\circ, t)}{\kappa_2 W^2(90^\circ, t)} = \frac{\kappa_1}{\kappa_2} Z_0(t). \tag{91}$$

The remaining fraction of κ_i and κ_j shall here be defined as the Start-Stop efficiency between Detector i and j . When the balanced ratio (90) is known, one can gain all the other detector efficiencies by thoughtfully combining the count rates $N(\theta, t)$. A matrix that describes the detector efficiencies can then be defined accordingly as

$$\kappa_{ij} = Z_{ij}(t)/Z_0(t) = \kappa_i/\kappa_j. \tag{92}$$

For polycrystalline PAC experiments involving probes with an $I = 5/2$ intermediate state, the angular correlation function (35) can be written in the more simplified form

$$W(\theta, t) \approx 1 + A_{22} G_{22}(t) P_2(\cos \theta). \tag{93}$$

For $^{111}\text{In}(\text{Cd})$ and $^{181}\text{Hf}(\text{Ta})$ is $A_{44} \ll A_{22}$, and hence A_{44} can be neglected for practical reasons. In order to extract the time-dependent anisotropy $A_{22}G_{22}(t)$ from the count rate spectra the following formulae,

$$R'(t) = \frac{2}{3} \left[\frac{N(180^\circ, t)}{N(90^\circ, t)} - 1 \right]$$

and

$$R(t) = A_{22}G_{22}(t) = \frac{R'(t)}{1 + \frac{1}{2}R'(t)} \tag{94}$$

can be used with the four $N(180^\circ, t)$ and eight $N(90^\circ, t)$ spectra. The time-dependent anisotropy $A_{22}G_{22}(t)$ is here equated with the count ratio function $R(t)$. In polycrystalline samples with random nuclei orientation exists no preference in orientation with respect to the detector arrangement. The four 180° count rates and the eight 90° count rates can be grouped together to gain a single expression as follows:

$$\begin{aligned} N(180^\circ, t) &= (N_{02}N_{13}N_{20}N_{31})^{\frac{1}{4}} \\ &= (\kappa_0\kappa_1\kappa_2\kappa_3)^{\frac{1}{4}} \frac{\sqrt{\varepsilon_0\varepsilon_1\varepsilon_2\varepsilon_3}}{\tau_N} N_0 e^{-t/\tau_N} W(180, t) \end{aligned} \quad (95)$$

$$\begin{aligned} N(90^\circ, t) &= (N_{03}N_{12}N_{01}N_{23}N_{30}N_{21}N_{10}N_{32})^{\frac{1}{8}} \\ &= (\kappa_0\kappa_1\kappa_2\kappa_3)^{\frac{1}{4}} \frac{\sqrt{\varepsilon_0\varepsilon_1\varepsilon_2\varepsilon_3}}{\tau_N} N_0 e^{-t/\tau_N} W(90, t) \end{aligned} \quad (96)$$

This artifice makes use of all available data at once increasing the statistical information in the combined count rates $N(\theta, t)$.

All the information about the interaction between the nucleus and the extranuclear fields are only contained in $G_{22}(t)$. In practice the count ratio is fitted to an expression which represents the perturbation function. The value of the anisotropy A_{22} contains nuclear parameters and was determined by other experiments in which their nature in nuclear physics were of primary interest. For $^{111}\text{In}(\text{Cd})$ and $^{181}\text{Hf}(\text{Ta})$ those values are given in Tables 1 and 2. The experimentally measured anisotropy $A_{22,eff}$, however, varies from the true value. Several sources for causing this deviation have been listed as [19]

- Finite detector size attenuation γ_a ,
- Finite time resolution γ_b ,
- Compton scattering γ_c ,
- Sample self-absorption γ_d .

The effective anisotropy can coarsely be expressed by the true A_{22} by

$$A_{22,eff} = \gamma_a\gamma_b\gamma_c\gamma_d A_{22}. \quad (97)$$

The finite detector size attenuation γ_a is a source that can be easily reconstructed theoretically. The count ratio (94) is generally computed under the assumption of

a point source and infinite detector distance. In practice the ideal condition is never fulfilled. If the finite size of the sample and the finite detector distance is taken into account, the angular correlation function (35) needs to be replaced by one that is a spatial average over the effective angles spanned by the source and the detector. By inserting the term (93) into Eq. (94) the $R(t)$ becomes

$$R(t) = \frac{2A_{22}G_{22}(t)(\langle P_2(180^\circ) \rangle - \langle P_2(90^\circ) \rangle)}{3 + A_{22}G_{22}(t)(\langle P_2(180^\circ) \rangle + 2\langle P_2(90^\circ) \rangle)} = \gamma_a A_{22}G_{22}(t). \quad (98)$$

where γ_a is the theoretical correction factor for the finite detector size effect. Figure 14 shows the result of a calculation of $\gamma_a A_{22}$ for the radioactive probe $^{111}\text{In}(\text{Cd})$. This calculation was performed using the Monte-Carlo method, where the effective angles were assumed for 1.5" diameter scintillators under variable distances. The sample dimensions were assumed to be a point sample. In addition, Figure 14 — \circ — exhibits effective anisotropy coefficients that were obtained from measurements on polycrystalline samples during the development of the new PAC spectrometer. The measured anisotropy is mostly below the theoretically evaluated values. The sole consideration of the effect of the finite detector size attenuation does not explain the result sufficient enough. It must be assumed that the effects of the remaining attenuation factors contribute to the reduction of the effective anisotropy. The good resolution of the new PAC spectrometers timing mechanism may lead to the assumption that the finite time resolution effect is relatively small, and thus $\gamma_b \approx 1$. As these results were obtained from solid samples with finite size the effects of Compton scattering and Self-sample adsorption cannot be neglected.

The $A_{22,eff}$ for $^{111}\text{In}(\text{Cd})$ in solution in Figure 14 — \triangle — were obtained using a diluted InCl_3 sample. Therefore the attenuation effect caused by Compton scattering and self-sample adsorption can be mostly ruled out. The magnitude of the $A_{22,eff}$ for the diluted sample were measured to be comparable to the $A_{22,eff}$ of the solid samples.

5.3 Timing Tests

Correct timing calibration is essential for PAC spectroscopy. For the new hardware it is not necessary to perform any timing calibration as it is known from conventional spectrometers. The spectrometer depends on the reliability of the DSP clocks. The maximum time resolution of the electronic system depends on the stability of the DSP clocks. Therefore, it is necessary to have knowledge of the quality of the

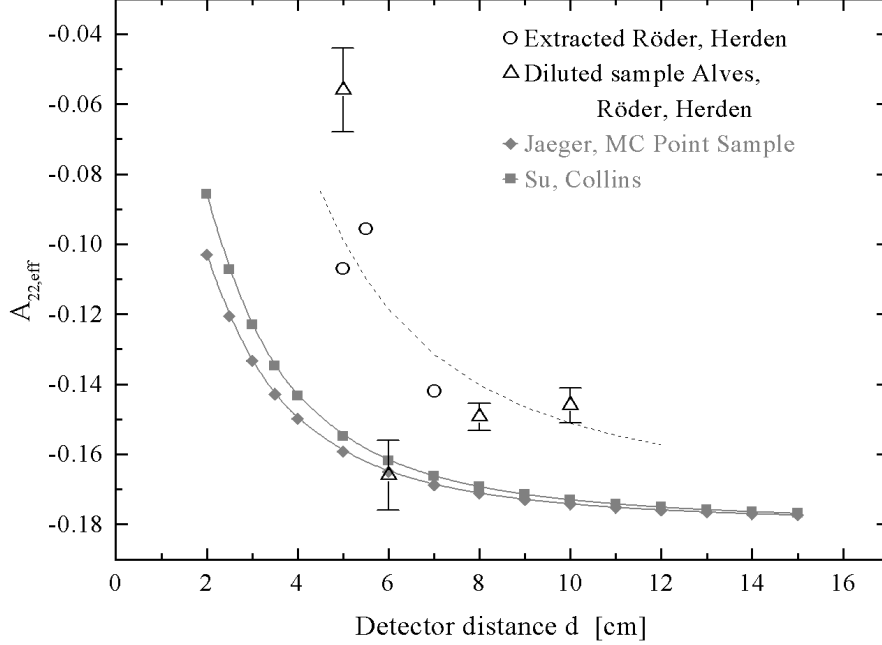


Figure 14: Effective anisotropy $A_{22,eff}$ in relationship with the detector distance. The data points marked as $- \circ -$ represent the obtained effective anisotropies $A_{22,eff}$ from various measurements on polycrystalline samples. The data points marked as $- \triangle -$ were obtained from anisotropy measurements with diluted samples. The dashed line just guides the eye. As a comparison, the plot shows two results from Monte Carlo calculations done by [16] and an empirical equation by [18].

synchronization system. The DSP clocks are synchronized by a 10 MHz external clock signal, which is distributed from a common source to all channels. In order to test the performance of the timing circuit the output of an external frequency generator was hooked up to all the MUX's PMT inputs. The frequency generator was primarily used to test the performance of the spectrometer, but also to certify that the synchronization mechanism is working accordingly. During the measurement the timestamps were recorded. Later the coincidence check process subtracted all the recorded timestamps for all permutations of channels i and j . Figure 15 *a.*) and 15 *b.*) show two prompt peaks that represent the achievable timing resolution.

The data points in Figure 15 *a.*) show a gaussian distribution, and also exhibit an interference pattern which results from the superposition of two timestamp counters driven by two nearly coherent running clocks. This behaviour can be explained formally like a double-slit experiment, where two coherent wave fronts interfere with each other [32]. Each clock can be adjudicated a frequency ν_i and a phase φ_i . The

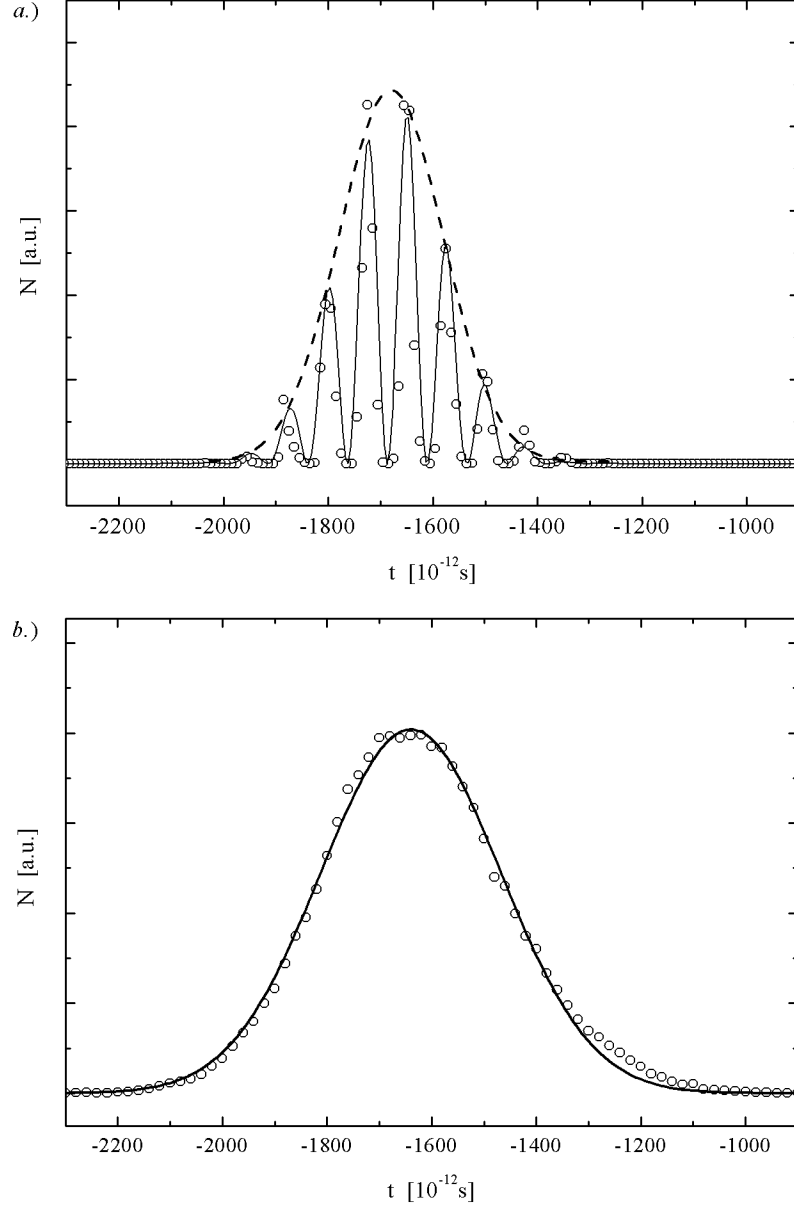


Figure 15: These two prompt peaks represent the achievable timing resolution of the bare electronic acquisition system between two PAC channels. *a.)* shows the peak without the application of CFD and jitter. The data points (o) in *a.)* were fitted according to Eq. (100), with $\Delta t_{FWHM} = 236 \pm 8$ ps. *b.)* shows the prompt peak with both jitter and CFD applied.

granularity of the DSP internal clocks are specified by the manufacturer at ~ 80 ps. The internal clock frequencies shall thus be assumed at $\nu_i = 1/80 \text{ ps}^{-1}$. The synchronization intervals are given by the external 10 MHz clock. When a coinciding event is recorded between two channels, a snapshot of the two timestamp counters is taken. A slight divergence of the clock frequencies ν_i and phases φ_i during the 100 ns period must be regarded, therefore, the internal clock frequencies ν_i can in general be slightly out of tune. The superposition of two frequencies ν_1 and ν_2 results in a fast and slow (beat) oscillation

$$\nu_{fast} = (\nu_1 + \nu_2)/2 \quad , \quad \nu_{slow} = (\nu_1 - \nu_2)/2. \quad (99)$$

Are the two frequencies close enough together the slow oscillation almost vanishes and ν_{fast} can be regarded as $\nu_{fast} = \nu_1 = \nu_2$. When the phenomenon of interference between two coherent sources are described mathematically by the superposition theorem, the result is usually modulated by a sinusoidal term [32]. The experimental evidence suggested that the data points were fitted according to the empirical expression

$$f(t) = 2 \frac{A}{w \sqrt{(\pi/2)}} e^{-2((t-t_0)/w)^2} (1 + \cos(2\pi\nu_{fast}(t - t_0) + \varphi(t))). \quad (100)$$

Several measurements between all detector combinations were performed with results that yield to an average time resolution of $\overline{\Delta t}_{FWHM} = \sqrt{2 \ln 2} \cdot w = 365 \pm 82 \text{ ps}$. The minimum profile width ever achieved was $\overline{\Delta t}_{FWHM} = 236 \pm 8 \text{ ps}$. From the fits the average clock granularity could be determined as $\overline{\nu}_{fast} = 1/76 \text{ ps}^{-1}$. The center of the prompt peak t_0 is shifted to negative times at $t_0 = -1698 \text{ ps}$. This gives rise to the conclusion that the signal propagation times per channel are not equal. Variations in cable lengths or tolerances in electronic components can cause a phase shift in the signal. The knowledge of these delay times, however, allows one to account for these times when computing the count ratio (94). All results have been summarized in Table 5.

The gaussian profile in Figure 15 *b.*) shows the prompt peak after smoothening the clock granularity. For smoothening the granularity an artificial jitter was added onto the timestamps. The jitter function is the result of the Linux kernel randomizer with an amplitude of 100. This technique introduces an additional broadening of the width of the prompt peak by an additional 100 ps. The result is a smoother gaussian

Parameter		time / [ps]	
Average time resolution Δt_{FWHM}		365 ± 82	
Average clock granularity $\bar{\nu}$		76	
Avg. signal delay	time / [ps]	Avg. signal delay	time / [ps]
$t_{0,12}$	488	$t_{0,21}$	-498
$t_{0,13}$	-1812	$t_{0,31}$	1791
$t_{0,14}$	-1698	$t_{0,41}$	1716

Table 5: Average timing resolution of the spectrometers electronic components and parametric time deviation in t_0 of the acquisition system involving Channel 1 as a Start (left column) and as a Stop (right column).

distribution under the sacrifice of some time resolution, which for many experiments is negligible.

These results determine the maximum achievable time resolution of the PAC setup. The average timing resolution of the measuring system lies well below 1 ns. This result gives also evidence that the independent DSP clocks are actually running coherently. It can thus be assumed with confidence, that the synchronization circuit is working sufficiently.

Six coincidental distributions of three channel pairings are displayed in Figure 16. All combinations were measured with respect to Channel 1. The first group consists of three distributions (solid black), which represent the combinations where the timestamps of Channel 2, 3, and 4 were subtracted from the timestamps of Channel 1. The second group consists of three distributions (light gray), where the timestamps of Channel 1 were subtracted from those of Channel 2, 3, and 4. Within every group the center of the three coincidental distributions are displaced by an average amount of $t_{0,12}$, $t_{0,13}$, and $t_{0,14}$. For the second group the time shifts are $t_{0,21}$, $t_{0,31}$, and $t_{0,41}$, respectively. Values for the average signal delays are given in Table 5. It is easy to see that the two groups of distributions are symmetrical around $t_0 = 0$ ps. The knowledge of the time shifts between the detector combinations is important for the correct computation of the count rates Eq. (89).

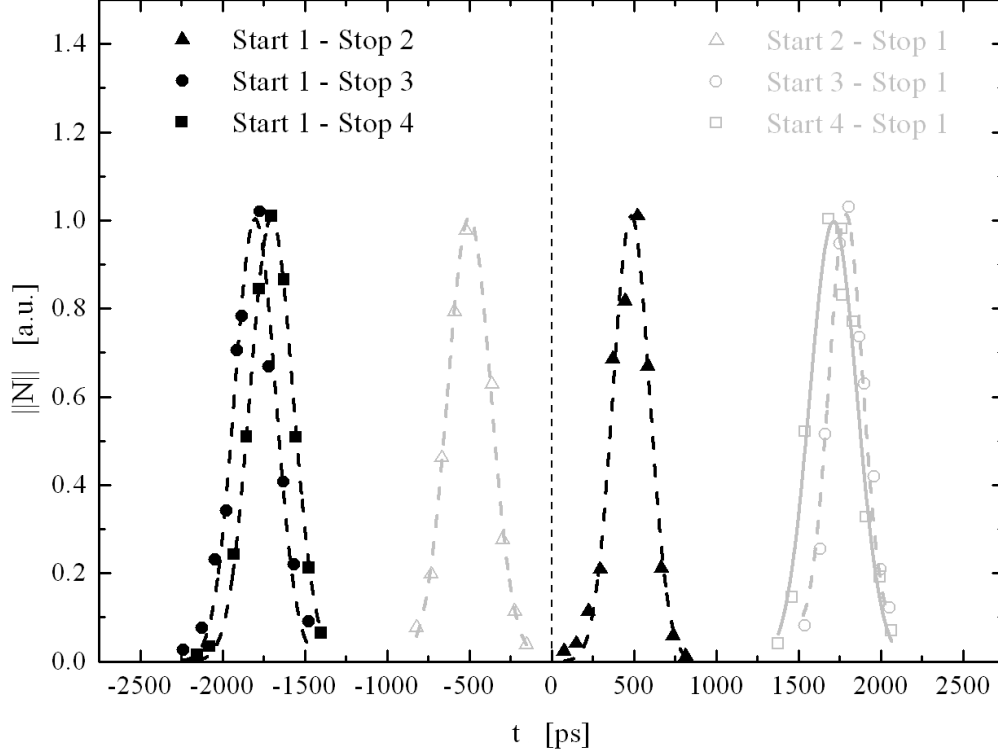


Figure 16: Time deviation in t_0 of the acquisition system involving Channel 1 as a Start (black) and as a Stop (grey). The center of the prompt peaks represent the time delay between two channels within the electronic system. The average width of the peaks are $\overline{\Delta t}_{FWHM} = 365 \text{ ps}$.

5.4 PAC Sample Preparation

PAC samples, utilizing $^{111}\text{In}(\text{Cd})$ in chloride solution and $^{181}\text{Hf}(\text{Ta})$, were prepared for testing purposes. The test samples were chosen because the compounds were studied with PAC spectroscopy before, and results are listed in numerous publications [33, 34, 38, 40, 44, 43, 42, 39]. Thus, their PAC frequencies are well known and can be used as a reference to the results obtained with this new spectrometer setup. The following list of samples were deployed in the first test runs:

- a.)* $^{111}\text{In}(\text{Cd})$ in Sn metal,
- b.)* $^{111}\text{In}(\text{Cd})$ in CdSiP_2 ,
- c.)* $^{111}\text{In}(\text{Cd})$ in Fe foil, and
- d.)* $^{181}\text{Hf}(\text{Ta})$ in Hf metal.

Sample *a.)* was provided by M. O. Zacate, Department of Physics, Washington State University. A few drops of InCl_3 solution were added to 3 g tin powder in a melting dish. At preparation time the sample activity was calibrated to 160 μCi . The sample was then molten in an oven for 2 h at a temperature well above the melting point of 231 °C. During this time most of the chloride evaporated out of the sample. The sample was then quenched and shaped to a sphere in a polishing process. The sample was received 2 days after preparation and the activity was measured to be around 73 μCi .

Sample *b.)* was obtained from Dr. S. Unterricker, Institut für Angewandte Physik, TU-Bergakademie Freiberg, as a few splinters from a single grown crystal. CdSiP_2 is a chalco- pyrite-structure compound of type $\text{A}^{\text{II}}\text{B}^{\text{IV}}\text{C}_2^{\text{V}}$. The splinters were grinded down manually in a mortar dish into a powder. The powder was then given into a quartz glass vial. The amount of InCl_3 solution was measured to not exceed the activity of 27 μCi . The solution was then given onto a quartz glass plate and then dried in an oven for a short time to vaporize the chloride content. The dried $^{111}\text{In}(\text{Cd})$ plate was added to the powder in the quartz vial. Before sealing the vial, a spatula tip of red phosphorus was added. This retains the partial pressure of phosphorus inside the vial during the annealing process, and prohibits the sample to be reduced from phosphorus. The vial was sealed under a vacuum, and then heated for 2-3 h at a temperature of 900 °C. Under this temperature the $^{111}\text{In}(\text{Cd})$ will substitute with the Cd sites, while the overall structure of the chalcopyrite stays intact.

A piece of iron foil of the size of a centimeter in square and a thickness of 5 μm was use as sample *c.)*. The radioactive isotope $^{111}\text{In}(\text{Cd})$ was implanted at IONAS, II. Physikalisches Institut, Universität Göttingen, with an energy of 400 keV. The terminal activity did not exceed 27 μCi due to legal restrictions and transportation purposes.

The probe element $^{181}\text{Hf}(\text{Ta})$ in sample *d.)* was obtained by neutron irradiation of a piece of Hafnium metal wire. The sample was provided by Dr. Ken S. Krane at the Oregon State Radiation Center, Oregon State University. More detailed information

about the irradiation process and initial sample activity was not available to the author. The sample was a recycled piece of irradiated hafnium metal wire of unknown age. Due to hafniums fairly long decay time of nearly 1.5 months the sample showed sufficient activity to perform a PAC experiment on.

6 Results

6.1 Performance

The performance of the recording apparatus will be discussed in this section. Primary interest is how the new apparatus performs in comparison to conventional PAC spectrometers.

In this analysis the data recorded for sample *c.*) was used to determine the performance of the apparatus. The sample was measured over a time span of 456 hours. During this time the spectrometer recorded $5.1 \cdot 10^9$ segments in $4 \cdot 168000$ sequence files. It takes the *Cocheck* program about 1215 minutes to process all the segments. The quotient between process time and real time is 4.4 %. Thus, the *Cocheck* process is on average 22.5 faster than the recording. Every sequence file contains a set of 8000 segments, that represent a transient signal recorded by the DSP boards. The raw data usually contains all trigger events without preselection through energy windows. Thus, all events from Compton-scattered photons and thermal electrons are part of the data as well. Transients whose integral and shape were identified as being less than zero or oddly shaped were discarded. The percentage of discarded events is on average under 1 %. The recorded activity for a single channel is given by the number of trigger signals registered within a time frame. However, the measured detector activity does not reflect the original sample activity, as only a fraction of the samples decay is detected. The solid angle fraction for the four detector setup used in this work can approximately be expressed as $f_{sa} = 4 \cdot A_D / A_S$. This ratio represents the area of the four scintillator crystals $4 \cdot A_D$ on the surface of a sphere A_S . The radius of the sphere is equivalent to the detector distance with the sample in the center. For this experiment a scintillator crystal diameter $\varnothing = 3.81$ cm and a detector distance $d = 5$ cm yield to the solid angle fraction $f_{sa} \approx 14.5$ %. Hence, it can be assumed that the original sample activity is by an amount of $1/f_{sa} \approx 6.9$ higher than the detected one. The average activity was determined from a set of 100 sequences, that were picked out of the pool of sequence files at various times. For 100 sequences the online time differences $t_{online}^n = t_{last}^n - t_{first}^n$ of the first and last recorded segment were taken, and the average activity calculated as

$$\bar{A}(t) = \frac{1}{100} \sum_{n=1}^{100} \frac{8000}{t_{online}^n}. \quad (101)$$

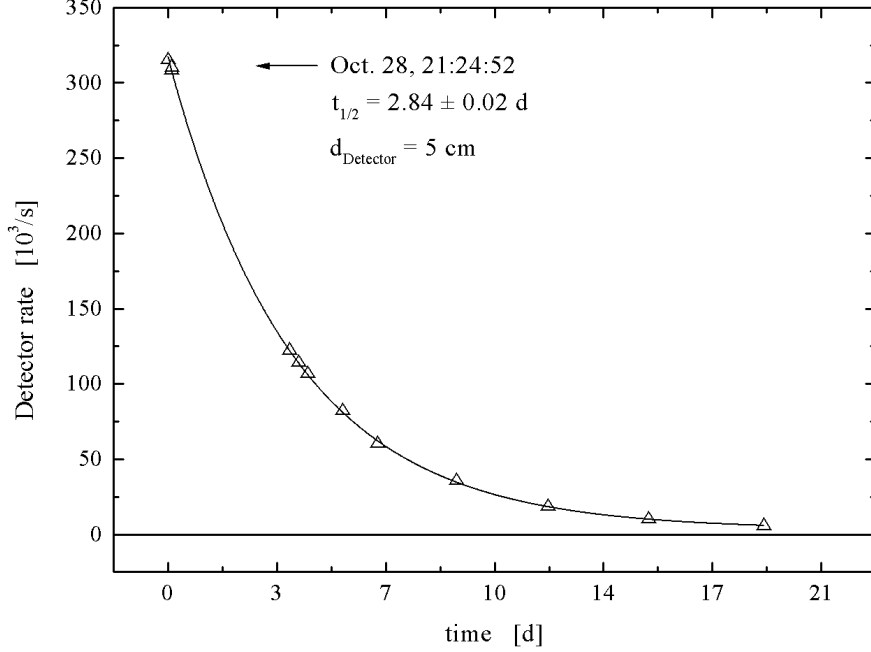


Figure 17: Activity of the *c.*) $^{111}\text{In}(\text{Cd})$ in Fe sample over time as recorded over a time span of 456 hours. The initial activity was measured to be around 0.315 MBq. The exponential fit yielded a half-life of 2.84 days.

Figure 17 shows a plot of the detected sample activity over time. At the beginning of the experiment the detected activity of sample *c.*) was determined to be 0.315 MBq. The dashed line represents an exponential fit to the data points. The half-life of the fit was determined to be $t_{1/2} = 2.84 \pm 0.02$, which is in good correspondence to the value given for $^{111}\text{In}(\text{Cd})$ in Table 1.

According to the measurements above the average trigger rate of each detector channel was 11.4 kHz at the beginning of the experiment. Thus, the DSP boards recorded one sequence of 8000 segments on average in approximately $8000 \cdot 87.7 \mu\text{s} \approx 0.7$ ms. The sequence files contain an absolute Unix timestamp that signifies when the data was collected. The Unix timestamp gives information about the recording cycle period t_{cycle} . The cycle time t_{cycle} that has elapsed during the recording of one sequence, however, exposes a variance with respect to the online time t_{online} . This variance is the dead time, or offline time, t_{offline} of the spectrometer. Figure 18 shows the duty cycle plotted as a function of the detected sample activity. The duty cycle was obtained from the ratio of the online time t_{online} and the cycle time t_{cycle} . For low activities t_{online} is dominant in regard to t_{offline} , which is almost negligible. Therefore,

the duty cycle approaches 100 %. The duty cycle values were obtained from activities recorded during the experiment. Activities beyond 1 MBq were not available for experimental purposes due to lab conditions and safety regulations. For a sample activity of 0.315 MBq the duty cycle of the apparatus was reduced to 87 %. The dashed line in Figure 18 was obtained from a fit according to Eq. 83. The fitted function extrapolates the duty cycle beyond the measured values. The development of the duty cycle starts out linear at first, but is expected to approach 0 % for higher activities. According to these results the 50 % duty cycle point of the apparatus can be estimated at a sample activity of 2.3 MBq. The fitting parameter $m/t_{offline}$ gains a value for the average dead time of $t_{offline} = 0.14 \pm 0.04$ s, with $m = 8000$ segments. This value is well to expect if one assumes the dead time only originates from the relation

$$t_{offline} = t_{trans} + t_{arm}. \quad (102)$$

The transfer time for transferring the raw waveform data over the PCI bus t_{trans} plus the time for reactivating the recorder boards t_{arm} add up to almost that value. According to the manufacturers specification the time to arm the boards for the sequence mode is rated around $t_{arm} = 0.1$ s [22]. The amount of data to be transferred is 3.2 MByte. With the PCI bus at a speed of 133 MByte/s it takes approximately $t_{trans} = 0.024$ s to download the waveform data into the PCs memory. One can conclude that the spectrometers dead time is as low as the digitizer hardware and the PCI bus speed would possibly allow it.

In this experiment the segment length was set to 400 ns. The energy integral was calculated from 400 sample points. A relative dissolution of energy of 16 ± 5 % was achieved. Using a longer segment length was thought to increase the energy resolution. More sample points might have put more weight on the integral. But no significant improvement could be detected, even up to 1000 sample points per segment. Depending on the calibration of the photomultiplier tubes, the anode signal decays within the first 400 - 500 ns. Choosing a larger segment length does not gain significantly more information about the energy. For the *Cocheck* process the energy window width was set to twice the FWHM of the energy, as shown in Figure 11 in Section 4.3.2 as the red and green shaded areas. The total amount of coincidences gathered in this experiment was $183.7 \cdot 10^6$, in 12 detector combinations and a coincidence window with of 8 μ s. Thereof the coincidence efficiency results in 3.6 %. The starting coincidence rate was 1.5 kCo/s for an activity of 0.315 MBq and en-

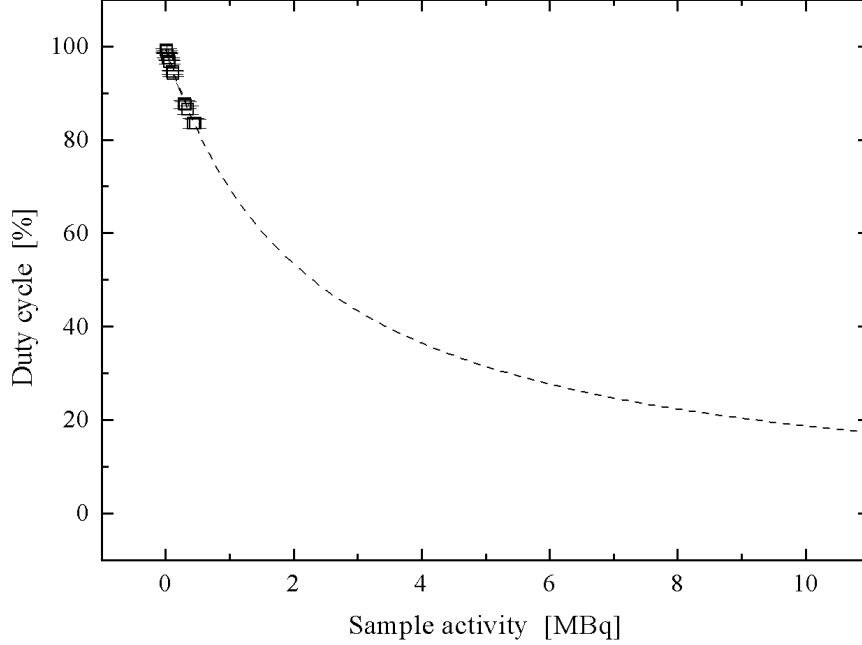


Figure 18: The spectrometers duty cycle over the detected sample activity. Data points are shown for activities between 0 and 0.315 MBq. The dashed line is a fit through the data points and represent the development of the duty cycle for higher activities.

ergy window width of $2 \cdot \text{FWHM}$. Table 6 summarizes all the obtained results for this experiment.

The coincidence rate varies with the width of the energy windows. This is understandable because the number of random coincidences increases with the size of the energy windows. In open-window mode all the possible coincidences are collected regardless of the γ -ray's energy. The beginning coincidence rate in open-window mode was 10.5 kCo/s.

The experiment showed that the new PAC apparatus did perform well with respect to a conventional PAC spectrometer. Sample activities were moderate and did not challenge the acquisition system. With an average trigger rate of 11.4 k/s this is well below of what the DSP boards can handle. In Section 3.4 it was previously discussed how the digitizers are very well capable of triggering at faster speeds. Using Eq. (80) a theoretical trigger rate of 1110 kHz for segment sizes of 400 samples is possible. However, tests with pulse generators have shown that the apparatus triggering saturates at rates around 825 kHz [47].

Parameter [unit]	Value
Scintillator crystal diameter [m]	0.0381
Detector distance [m]	0.05
Solid angle fraction [%]	14.5
Detected beginning sample activity [Bq]	$0.315 \cdot 10^6$
Recording duration [h]	456
Number of sequences	$4 \cdot 168000$
Acquired γ -rays	$5.1 \cdot 10^9$
Acquired coincidences	$183.7 \cdot 10^6$
Beginning trigger rate [kHz]	$4 \cdot 11.4$
Beginning coincidence rate [kCo/s]	1.5 (2-FWHM window) 10.5 (open-window)

Table 6: Summarized results for the *c.*) $^{111}\text{In}(\text{Cd})$ in Fe sample experiment.

6.2 PAC measurements

The PAC samples introduced in Section 5.4 were measured in the new PAC setup. This section will present the results obtained for samples (*a.*) - (*d.*). The results will be compared with data denoted in the literature. In order to verify the system functionality these measurements on well known systems were done for validation purposes. All measurements were carried out at room temperature and no external magnetic or electrical fields were present. Because of variations in sample activities and detector distance the duration of the experiments varied between 7 hours and 3 days.

The *Cocheck* process accumulated the time spectra into a set of 12 files denoted by *dij.dat*. These files contain 12 single time spectra $D_{ij}(t)$ plus the random background count. Coincidences were collected in time slots with a resolution of 250 ps. The coincidence spectra consists of 8000 of such slots. Coincidences were collected for a wide span of positive times as well as negative times. The prompt peak t_0 is located in the center of the spectrum. The large time span enables the exact determination of the average background count B_{ij} . The knowledge of the exact average background count is very important for the determination of the count ratio function (94). In general,

the time spectra need to be both background and time corrected. According to Eq. (89) the background-corrected $N_{ij}(t)$ is obtained by subtraction of the background count. The random background data is available for a large time span, so it can be easily fitted to a linear approximation. With the help of the channel delay times from Table 5 the time-corrected $N_{ij}(t)$ can be determined. The delay times can be used to correct the time axis to positive or negative times, respectively. Thus, the count ratio (94) can be built from the obtained time- and background-corrected time spectra $N_{ij}(t)$. The characteristics of the obtained count ratios $R(t)$ were all fitted according to Eq. (34) for electric quadrupoles and Eq.(79) for magnetic dipoles. Practical, more general and simplified versions of Eqs. (34) and (79) suitable for fitting the data under the assumption of a static, non-fluctuating EFG or intrinsic \vec{B} -field and $I = 5/2$ are

$$R_Q(t) = A_{22,eff} \left(\sum_{i=1} f_i \sum_{n=0}^3 s_{2n,i} \cos(\omega_{n,i}t) \right), \quad (103)$$

$$R_M(t) = A_{22,eff} \left(\sum_{i=1} f_i \sum_{k=0,even}^{k_{max}} b_{2k,i} \cos(k\omega_{L,i}t) \right), \quad (104)$$

while the fractions f_i were introduced considering the fact, that different sites in the lattice may be occupied by the nucleus. Depending on the type of interaction multiple constraints can be inflicted on the fitting function. Firstly, for quadrupole interaction it is essential for all core parameters that $\sum_n s_{2n} = 1$ complies. Secondly, the integrity of the quadrupole frequencies $\omega_3 = \omega_1 + \omega_2$ has to be regarded.

For magnetic interaction the perturbation function can contain the fundamental Larmor frequency ω_L as well as higher harmonics $k \cdot \omega_L$. The core parameters b_{2k} for magnetic interaction yield more or less to the statistical information about the orientation of the magnetic flux. The resulting anisotropies obtained for samples *a.)* - *d.)* shall be discussed in the following.

6.2.1 Sample *a.)* $^{111}\text{In}(\text{Cd})$ in $\beta\text{-Sn}$ metal

Tin is a non-cubic, highly crystalline metal. Below 13.2 °C it exists as $\alpha\text{-Sn}$, which has cubic crystal structure. At room temperature the crystal structure is tetragonal [50]. Due to tetragonal crystal structure the V_{zz} component of the electric field gradient is non-zero. In general is it difficult to predict where the radioactive probe is integrated

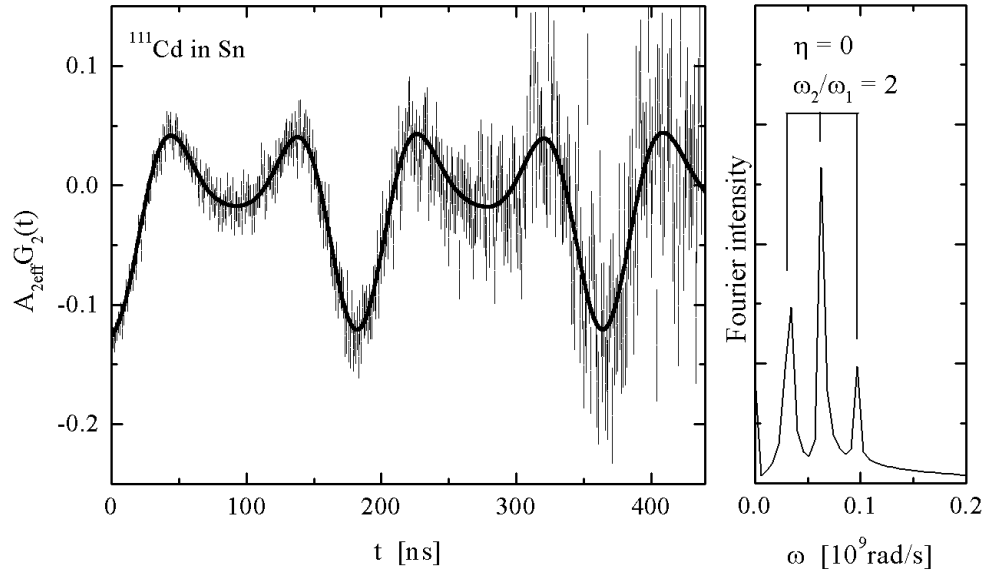


Figure 19: Time-dependent anisotropy $A_{22,eff}G_{22}(t)$ and the corresponding Fourier transform for $^{111}\text{In}(\text{Cd})$ in $\beta\text{-Sn}$ metal. The data point resolution is 0.25 ns/channel.

into the host lattice. The characteristics of the obtained time-dependent anisotropy $A_{22,eff}G_{22}(t)$ for sample *a.*) were fitted according to Eq. (103). The orientation of the Sn metal grains is mostly randomly distributed within the quenched metal. The core parameters s_{kn} , however, may deviate from the theoretical proportions due to non-random texture effects. This can occur when there are just a few large grains in the sample. A correlation has been seen between low melting temperature and increased non-random texture effects [41].

Figure 19 shows a plot of the fit function prototype Eq. (103) and the time-dependent anisotropy as measured for sample *a.*) with a timing resolution of 250 ps. The corresponding Fourier spectrum on the right renders the intensity relation of the coefficients s_{2n} . On average the maximum acquired coincidence count for all detector pairings was 9000 around t_0 . The statistical coincidence information per time slot decreases with higher timing resolution for experiments with equal duration. The acquisition hardware in this work is 2 – 4 times superior in comparison to conventional analog PAC setups, which typically yield between 0.5 and 1 ns per slot [17, 53]. Lower statistical information per time slot results typically in larger errors bars for each data point.

Sample *a.*) showed a quadrupole interaction with an asymmetry factor $\eta = 0$. The occupation of Cd in one site was observed as is $f_1 = 1$. The three PAC frequencies

ω_n were found to be in the ratio 1:2:3 with the fundamental frequency

$$\omega_1 = 34.76 \text{ Mrad/s.}$$

The effective anisotropy was determined as $A_{22,eff} = -0.143$. This value varies in general with the detector distance, which was $d = 7$ cm in this experiment. The obtained core parameters s_{2n} from this least-square-error fit are

$$\begin{aligned} s_{20} &= 0.218, \\ s_{21} &= 0.256, \\ s_{22} &= 0.403, \\ s_{23} &= 0.123. \end{aligned}$$

From the above results the quadrupole frequency $\omega_Q = \omega_1/6$ for $I = 5/2$ can be derived. The quadrupole coupling constant ω_Q is defined for the axially symmetric case $\eta = 0$ by Eq. (67). For the quadrupole coupling constant one obtains $\omega_Q = \omega_1/6 = 5.79$ Mrad/s for half-integer nuclear spin. With the quadrupole moment $Q_{5/2} = 0.77 \cdot 10^{-28} \text{ m}^2$ for Cd the magnitude of the electric field gradient element is $V_{zz} = 1.98 \cdot 10^{21} \text{ V/m}^2$. These results are in good agreement with the quadrupole coupling constants $\omega_Q = 5.84(1)$ Mrad/s or $\omega_Q = 5.73(4)$ Mrad/s found in the literature [48, 49]. Measurements were performed on $^{111}\text{In}(\text{Cd})$ in Sn hosts for various pressures at room temperature [51]. Although, the published PAC spectra show no texture effects in the core parameters, the actual quadrupole frequencies agree very well with the ones found with this spectrometer.

6.2.2 Sample *b.*) $^{111}\text{In}(\text{Cd})$ in Cadmium Silicon Phosphide

The quadrupole interaction of the chalcopyrite semiconductor CdSiP_2 was investigated with the new PAC spectrometer setup. The electric field gradient in this type $\text{A}^{\text{II}}\text{B}^{\text{IV}}\text{C}_2^{\text{V}}$ compound is known to be axially symmetric ($\eta = 0$) when the sample was annealed [34]. The unit cell of a chalcopyrite consists basically of two sphalerites that were doubled in c -direction and two different cations. In sphalerite exists a face-centered cubic arrangement of A-sites and B-sites in the center of each tetrahedron. For CdSiP_2 the cells with silicon atoms alternate with cells containing cadmium. The phosphor is positioned on the chalcopyrite C-sites. The double cells mean that chalcopyrite is tetragonal, but the fact that the unit cell consists of two cubes means chalcopyrite mimics cubic symmetry very often. TDPAC investigations gave very

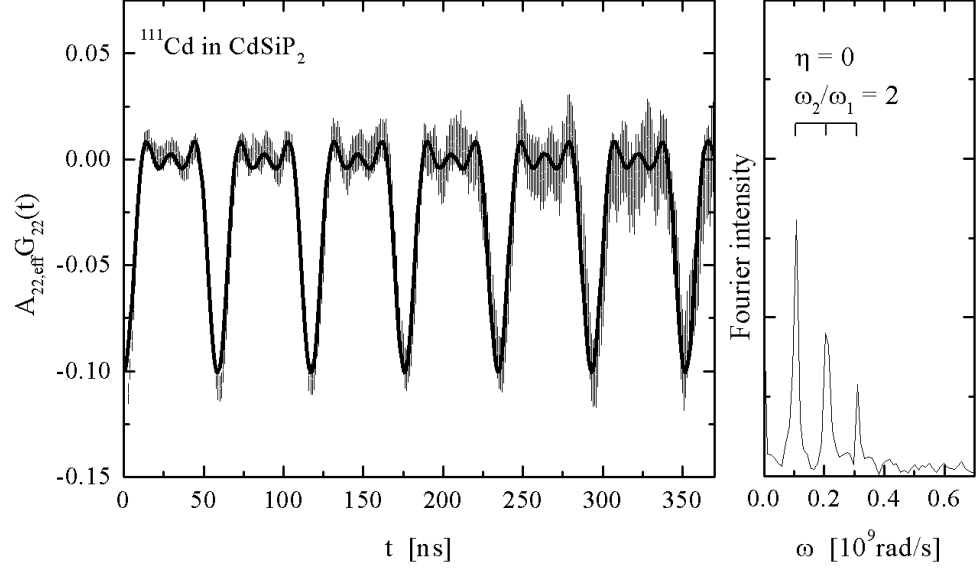


Figure 20: Time-dependent anisotropy $A_{22,eff}G_{22}(t)$ and corresponding Fourier transform for $^{111}\text{In}(\text{Cd})$ in polycrystalline CdSiP_2 at room temperature. The sample shows quadrupole interaction with an axially symmetric EFG ($\eta = 0$). The fundamental PAC frequency was determined as $\omega_1 = 107.2$ Mrad/s leading to a quadrupole coupling constant of $\omega_Q = 17.87$ MHz.

clear spectra and in previous works it was shown that the $^{111}\text{In}(\text{Cd})$ cation is really positioned on the chalcopyrite A-site [35]. The nearest neighbour to the Cd-atoms are the P-atoms. The time-dependent anisotropy in Figure 20 is a perfect example for an axially symmetric EFG ($\eta = 0$) in a polycrystalline sample.

The quadrupole coupling constants were obtained from a least-square-error fit on the data according to Eq. (103) with a single fraction $f_i = 1$. The theoretical predicted values of the core parameters s_{kn} for a polycrystalline sample with an axially symmetric EFG were held fixed during the process. The theoretical core values for $I = 5/2$ are [2]

$$\begin{aligned} s_{20} &= 1/5, \\ s_{21} &= 13/37, \\ s_{22} &= 2/7, \\ s_{23} &= 1/7. \end{aligned}$$

The least-square-error fit complies very well with the obtained data. The effective anisotropy was identified as $A_{22,eff} = -0.109$ for a detector distance of $d = 5$ cm. The

fundamental PAC frequency resulted in $\omega_1 = 107.2$ Mrad/s giving rise to a quadrupole coupling constant of $\omega_Q = 17.87$ Mrad/s for half-integer spin and an EFG component of $V_{zz} = 6.11 \cdot 10^{21}$ V/m² ($\eta = 0$). The quadrupole frequencies and components of the EFG could be reproduced with an accuracy of about 4% and comply very well with the quadrupole coupling constant $\nu_Q = 110.1(9)$ MHz ($\omega_Q = 17.5(4)$ Mrad/s) found in [33, 34].

6.2.3 Sample *c.*) ¹¹¹In(Cd) in Iron foil

Electric quadrupole interaction is usually abandoned in materials with body-centered (*bcc*) cubic structure, such as α -iron metal [52]. Ion-implantation-induced defects in the host lattice can lead to break up of the symmetry and leaves the probe atom in an environment which causes the EFG to be non-zero. Defects are usually healed when the irradiated sample is annealed, the original symmetry is restored and the quadrupole interaction is known to be zero [43]. The fact that iron exhibits spontaneous ferromagnetism leads to the presence of internal magnetic fields. When exposed to a magnetic field the nucleus magnetic momentum is aligned with the magnetic flux. The strength of the local magnetic field is proportional to the split of the nucleus discrete energy levels. This magnetic dipole interaction was measured in sample (*c.*). A quadrupole interaction was practically non-existing. The measured time-dependent anisotropy $A_{22,eff}G_{22}(t)$ is presented in Figure 21. The coincidence data was recorded with a timing resolution of 250 ps. For magnetic interaction the theory predicts that the time-dependent perturbation factor $G_{22}(t)$ is modulated with the Larmor frequency ω_L . For a nuclear spin of $I = 5/2$ and the index $k \leq 2I$ as of Eq. (78), the perturbation factor $G_{22}(t)$ can contain integer multiple terms of the fundamental frequency ω_L . The obtained data shows clearly magnetic interaction with ω_{L1} , but there is evidence of the presence of a second site with a slightly lower Larmor frequency ω_{L2} . The anisotropy data was fitted according to Eq. (104) with a two-site variation. The results for this fit are listed as follows:

Site	f_i [%]	ω_L [Mrad/s]
1	91.3	558.8 ± 0.2
2	8.7	384.8 ± 1.1

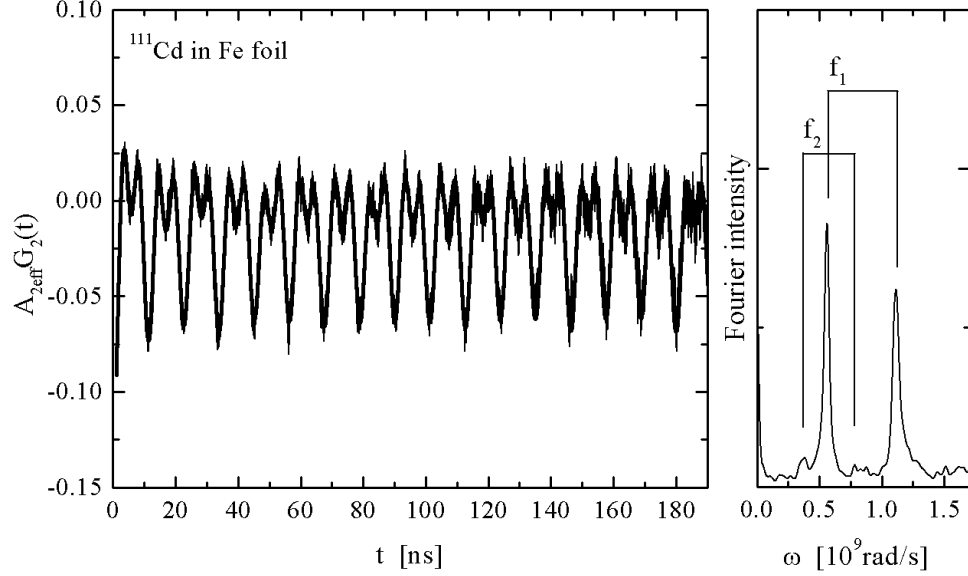


Figure 21: Time-dependent anisotropy $A_{2,eff}G_{22}(t)$ and the corresponding Fourier transform for $^{111}\text{In}(\text{Cd})$ in α -iron metal foil at room temperature. The data point resolution is 0.25 ns/channel. The sample shows magnetic interaction on two sites f_1 and f_2 . The two obtained Larmor frequencies are $\omega_{L1} = 558.8$ Mrad/s and $\omega_{L2} = 384.8$ Mrad/s.

The first fraction f_1 represents Cd placed on substitutional, defect-free sites of Fe in the Fe host lattice [45]. The second site may occur from remaining defects in the host lattice due to the ion implantation process. The second fraction f_2 is very much suppressed in comparison to the main fraction. It was reported that the presence of a second site results from nn-defects, however, metallic samples generally show negligible radiation damage after low-dose implantation treatment [46]. The fairly high-frequency PAC spectrum could be very well resolved with the new spectrometer setup over a wide time span. The Larmor frequency ω_L could be very well reproduced and deviates within an amount of 0.9 % compared to the quadrupole coupling constant $\omega_Q = 553(4)$ Mrad/s found in [37, 43].

6.2.4 Sample d.) $^{181}\text{Hf}(\text{Ta})$ in Hafnium metal

As a hexagonal-closed-packed (*hcp*) group IV metal Hafnium is a noncubic metal. In contrast to diamagnetic cubic metals, a noncubic metal already exhibits quadrupole interaction if a probe atom occupies a substitutional lattice site with an unperturbed surrounding due to the intrinsic EFG. The obtained time-dependent anisotropy $A_{2,eff}G_{22}(t)$

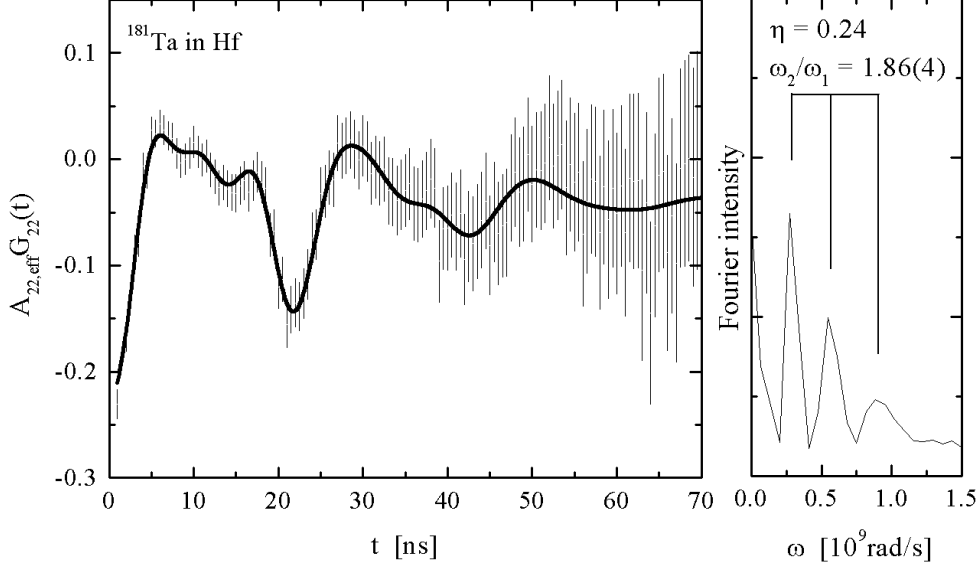


Figure 22: Time-dependent anisotropy $A_{22,eff}G_{22}(t)$ and the corresponding Fourier transform for $^{181}\text{Hf}(\text{Ta})$ in Hf metal. The data point resolution is 0.25 ns/channel. The sample shows an asymmetry of $\eta \approx 0.24$. The obtained fundamental PAC frequency at room temperature is $\omega_1 = 309 \pm 2$ Mrad/s.

at room temperature and its corresponding Fourier transform are displayed in Figure 22. The PAC spectrum for sample *d.*) exhibits a nonaxial symmetric EFG. It was fitted to Eq. (103) with a single fraction $f_1 = 1$. The core parameters $s_{2n}(\eta)$ were held invariant. Since the core parameters are a function of the asymmetry parameter, their theoretical values were taken from published tables [54]. The three PAC frequencies spacing were attributed to an asymmetry parameter $\eta = 0.24$. The fundamental frequency yielded to a quadrupole coupling constant $\omega_Q = 51.5 \pm 0.3$ Mrad/s. The quadrupole moment of $^{181}\text{Hf}(\text{Ta})$ intermediate level is $Q_{5/2} = 2.35 \cdot 10^{-28} \text{ m}^2$. Using Eq. (67) an EFG component $V_{zz} = 5.71 \cdot 10^{21} \text{ V/m}$ can be derived from the above values.

The PAC spectrum also exhibits an attenuation of the anisotropy which essentially is visible as broadening of the quadrupole frequencies in the Fourier spectrum. This is typically attributed to the presence of a nonstatic, fluctuating EFG. The effective anisotropy $A_{22,eff}$ was determined as $A_{22,eff} = -0.22$ for a detector distance of $d = 10$ cm. The PAC frequencies are in good agreement with the quadrupole coupling constants $\omega_Q = 50.9(7)$ Mrad/s and asymmetry $\eta = 0.24$ previously published for 99 % at. ^{181}Ta in HfZr alloy [39, 42].

6.3 Detector Start-Stop Efficiencies

So far the analog portion of this fully digital acquisition system has not yet been discussed much. The analog part of this apparatus consists mostly of the PMT and their high-voltage power supplies. As mentioned earlier there are several unpredictable sources for unwanted effects in PMTs. Thermal electrons randomly excite and multiply causing unwanted trigger events, which affect the efficiency of the system. Physical damage to the PMTs or their shields are additional sources for detector activity. For practical reasons it is important to know how well the PMT operate in this otherwise very deterministic environment.

The detector Start-Stop efficiencies have been extracted using the raw count rates $N(\theta, t)$ obtained by the measurements mentioned in the previous sections. The count rates were combined as described in Section 5.2 according to Eq. (91) and (92). For those measurements the elements of κ_{ij} for the current set of detectors were determined as

$$\kappa_{ij} = \begin{pmatrix} 1 & 0.722 & 1.075 & 0.836 \\ 1.39 & 1 & 1.484 & 1.145 \\ 0.948 & 0.677 & 1 & 0.784 \\ 1.202 & 0.876 & 1.284 & 1 \end{pmatrix} \quad (105)$$

This matrix shows, for instance, that detector 2 has overall the worst Start efficiency compared to all other detectors. All non-diagonal elements in column 2 are below an efficiency of 1. This represents that the efficiency of detector 2 as being a Start is lower than all the other detectors. All $\kappa_i|_{i \neq 2}$ are larger in magnitude than κ_2 . By definition of κ_{ij} the multiplication of all anti-diagonal elements must yield to 1, which is the case here.

7 Conclusion

The experiments conducted on the new spectrometer design verify that the acquisition system operates more than sufficiently for the intended purpose. Major differences to conventional PAC spectrometers can be described as follows. The setup cannot be classified into Slow-Fast or Fast-Fast systems anymore. The information about the time of arrival and γ -ray energy is always recorded simultaneously. There are no restrictions of which channel can act as the Start and which channel as the corresponding Stop. All channels are peer to each other. The small dead time allows the spectrometer to record any γ -ray that enters a detector, creating a snapshot of the nuclear decay over time. Any information about the radioactive probe seen by a detector is thus stored on the harddrive. An experiment can virtually be reconducted at any other time, allowing successive alterations to parameters.

The results from the experiments conducted on several samples validate the correct operation of the recording apparatus very well. All measurements show the reproducibility of the PAC frequencies in samples *a.)* – *d.)* with the new spectrometer setup. The few deviations in the results may mainly occur due to differences in the sample preparation methods. However, the results were all determined within feasible error margins. A careful determination of the relationship between anisotropy and distance was not main subject of interest in the thesis. The dependence of the effective anisotropy to the detector distance deviates strongly from the theoretical model. The few data points obtained through various test measurements express only roughly the tendency of an increasing anisotropy with increasing detector distance. Within the appointed distances they never quite reach the magnitude of the predicted value. Therefore, it must be concluded that additional attenuation values must contribute to the reduction of the effective anisotropy. It cannot be ruled out, that flaws during development of the new data reduction methods were responsible for inaccurate results. Further, it is not even clear that the ratio between the effective and the absolute anisotropy can be calculated that well.

As demonstrated by the test experiments the timing resolution of less than 400 ps of the digital recorderboards is outstanding in comparison to conventionally used analog Time-to-Amplitude converters. In the future the timing resolution may even increase when digitizers with sampling rates of 2 GHz or more are being employed. However, at this time the timing resolution limiting factor can clearly be attributed to the present γ -ray detector technology.

The new PAC spectrometer has advantages in many aspects. The design allows the expansion to basically any number of detector channels. The complexity of the component arrangement does not pose any limit on channel numbers. For convenient mathematical reasons, conventional PAC detector arrangements of 4 or 6 detectors are typically chosen with angles of 90° and 180° on all three spatial axes. With gaining spectra under any angles between detectors within one experiment, conventional analysis and data reduction methods are not necessarily applicable anymore. Therefore, new data reduction methods need to be developed for arbitrary detector setups.

The entire system is controlled by software which can in most cases be easily adjusted to certain needs. The calibration of the spectrometer is comparatively simple. A manual timing calibration of the system is basically not applicable due to the precise clock generators on the digital recorderboards. Because these sample clocks are programmable the spectrometer timing resolution can be adjusted individually by software. The γ -ray spectra are recorded continuously. Start and Stop windows can be set according to the spectra that are being stored while a measurement is running. This allows a calibration of the energy windows on-the-fly. For the future it is conceivable that these energy windows are being located automatically by software when the type of nucleus is chosen by the operator. Calibration parameters for each radioactive probe nuclei can be pulled out of a system database when needed.

There have also been advances in DSP technology since the first set of recorder boards for this work were acquired. More recent versions feature more on-board memory and higher sampling rates. The use of more memory would reduce dead times. Improvements are also expected from using a more recent-generation computer with fast PCI-Bus technology and higher processing speed. The slave computers remain, even during recording, mainly idle. Utilizing their computing power in a parallel computing environment, the coincidence check process could improve the throughput for high end data analysis.

The development of additional helper applications is in progress at the present time. For the operator, in regards to Ease-Of-Use, a World Wide Web interface will provide access to the spectrometer. It may allow to perform all the necessary adjustments. One can follow the course of the experiment remotely at any time as long as the spectrometers host computer is connected to the internet. The rather complex modality of extracting PAC frequencies from the data will be possible through a graphically based web interface, supported by a universal collection of PAC fitting libraries.

A Appendix

A.1 Parallel port pin assignment

Pin No (D-Type 25)	SPP signal	Direction	Register	Hardware inverted
1	/STROBE	Out	Control	Yes
2	DATA0	Out	Data	No
3	DATA1	Out	Data	No
4	DATA2	Out	Data	No
5	DATA3	Out	Data	No
6	DATA4	Out	Data	No
7	DATA5	Out	Data	No
8	DATA6	Out	Data	No
9	DATA7	Out	Data	No
10	/ACKN	In	Status	No
11	BUSY	In	Status	Yes
12	PAPER_OUT	In	Status	No
13	SELECT	In	Status	No
14	/AUTOFEED	In/Out	Control	Yes
15	/FAULT	In	Status	No
16	/INIT	In/Out	Control	No
17	/SELECT_IN	In/Out	Control	Yes
18-25	Ground	Gnd		

Table 7: Pin assignment of the D-Type 25 pin standard parallel port connector.

A.2 Parallel port I/O registers

Address	Name	Read/Write	Bit No.	Property
Base + 0	Data port	Write only	Bit 7	DATA 7
			Bit 6	DATA 6
		
		
			Bit 0	DATA 0
Address	Name	Read/Write	Bit No.	Property
Base + 1	Status port	Read only	Bit 7	BUSY
			Bit 6	/ACKN
			Bit 5	Paper Out
			Bit 4	Select In
			Bit 3	Error
			Bit 2	/Irq
			Bit 1	Reserved
			Bit 0	Reserved
Address	Name	Read/Write	Bit No.	Property
Base + 2	Control port	Read/Write	Bit 7	Unused
			Bit 6	Unused
			Bit 5	Enable Bi-Dir port
			Bit 4	Enable Irq
			Bit 3	Select printer
			Bit 2	Init printer
			Bit 1	Auto linefeed
			Bit 0	Strobe

Table 8: Bit assignment of the Standard Parallel Port I/O register [29].

A.3 Schematic diagrams

A.3.1 Wiring Plan

Figure A.3.1: Overview of the wiring between the spectrometer components.

A.3.2 Analog Multiplexer Module

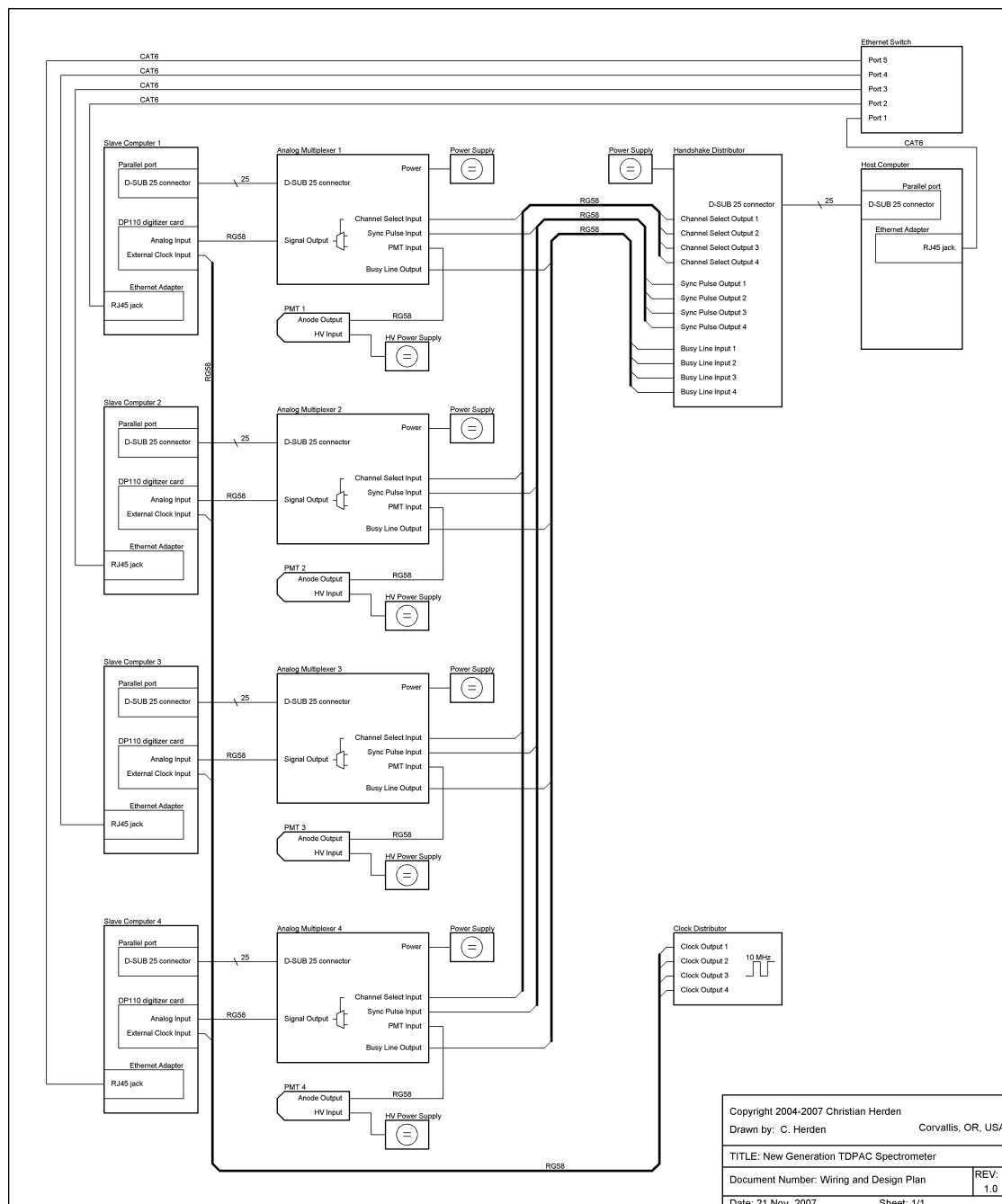
Figure A.3.2: Schematic diagram of the analog multiplexer module. The center piece is an integrated high-speed multiplexer circuit (U4) with 2 analog inputs. Its input IN2 is directly connected with the PMT signal output. IN1 is input to the synchronization pulse, which is directed through the derivative element (C6, R7, R11) from the logic trigger input at U2.

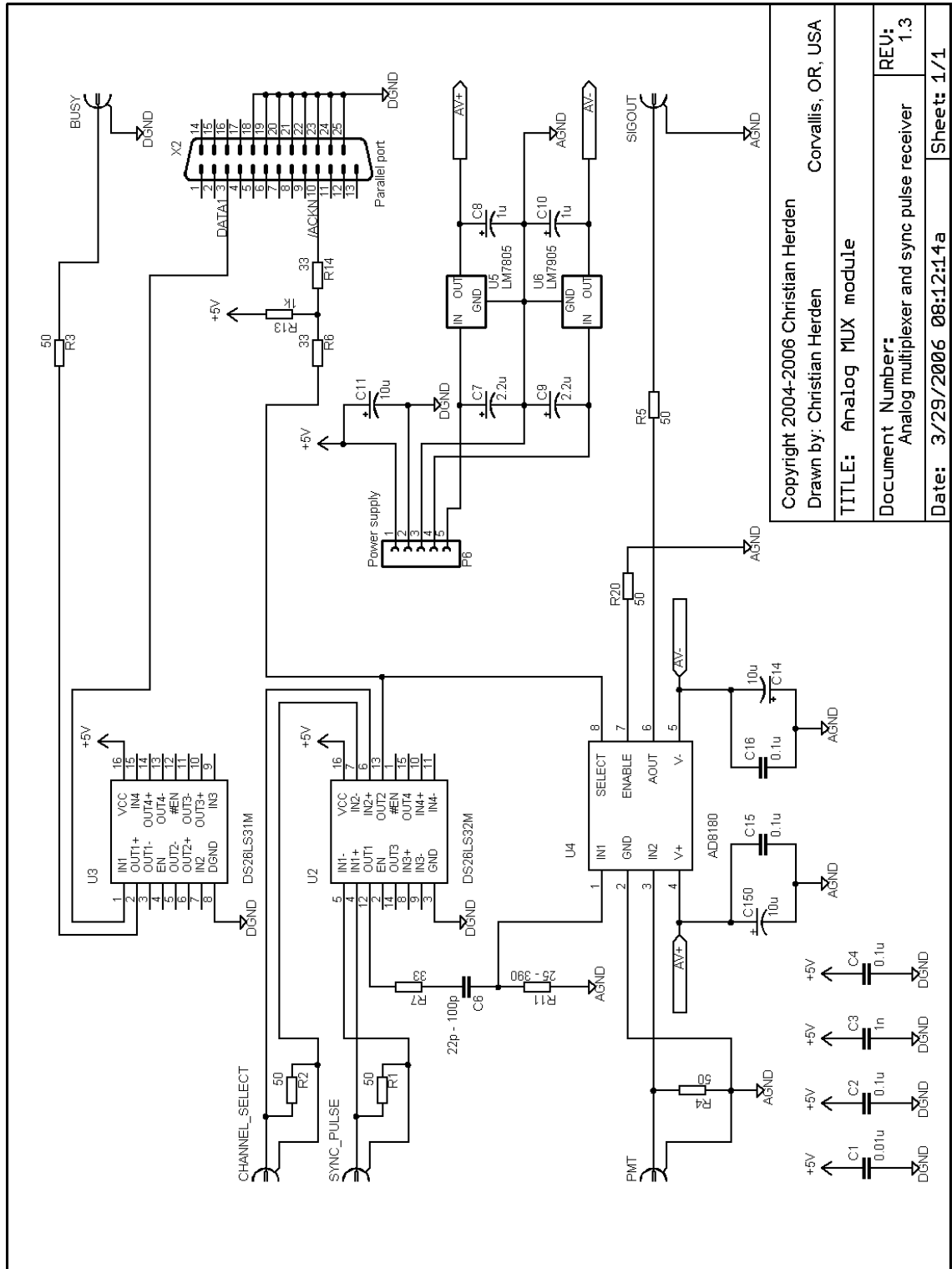
A.3.3 Synchronization and Channel Select Module

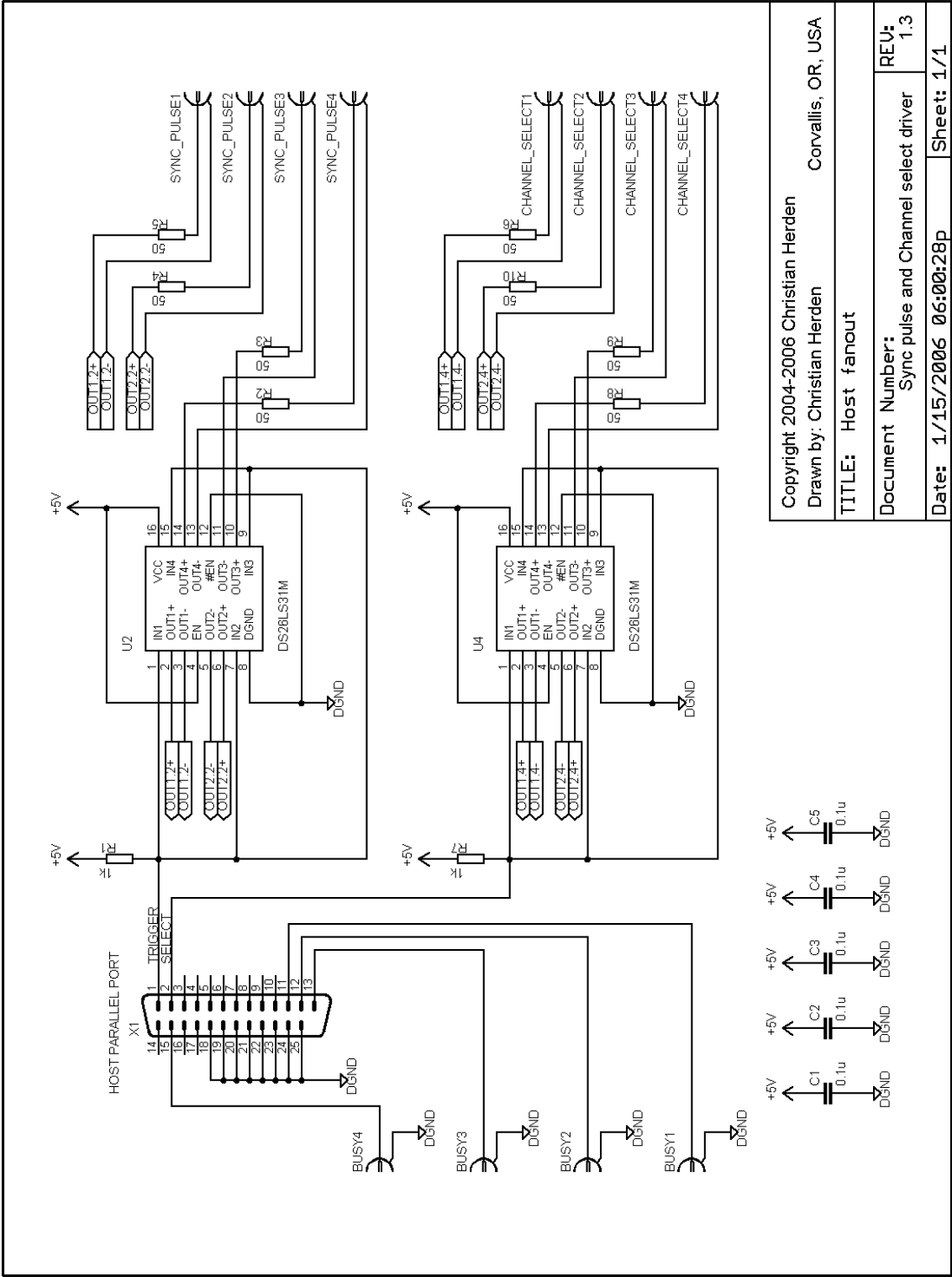
Figure A.3.3: Schematic diagram of the Synchronization and Channel Select fanout module. Two quadruple integrated $100\ \Omega$ line driver circuits provide the necessary impedance conversion from the logic TTL output to the BNC output.

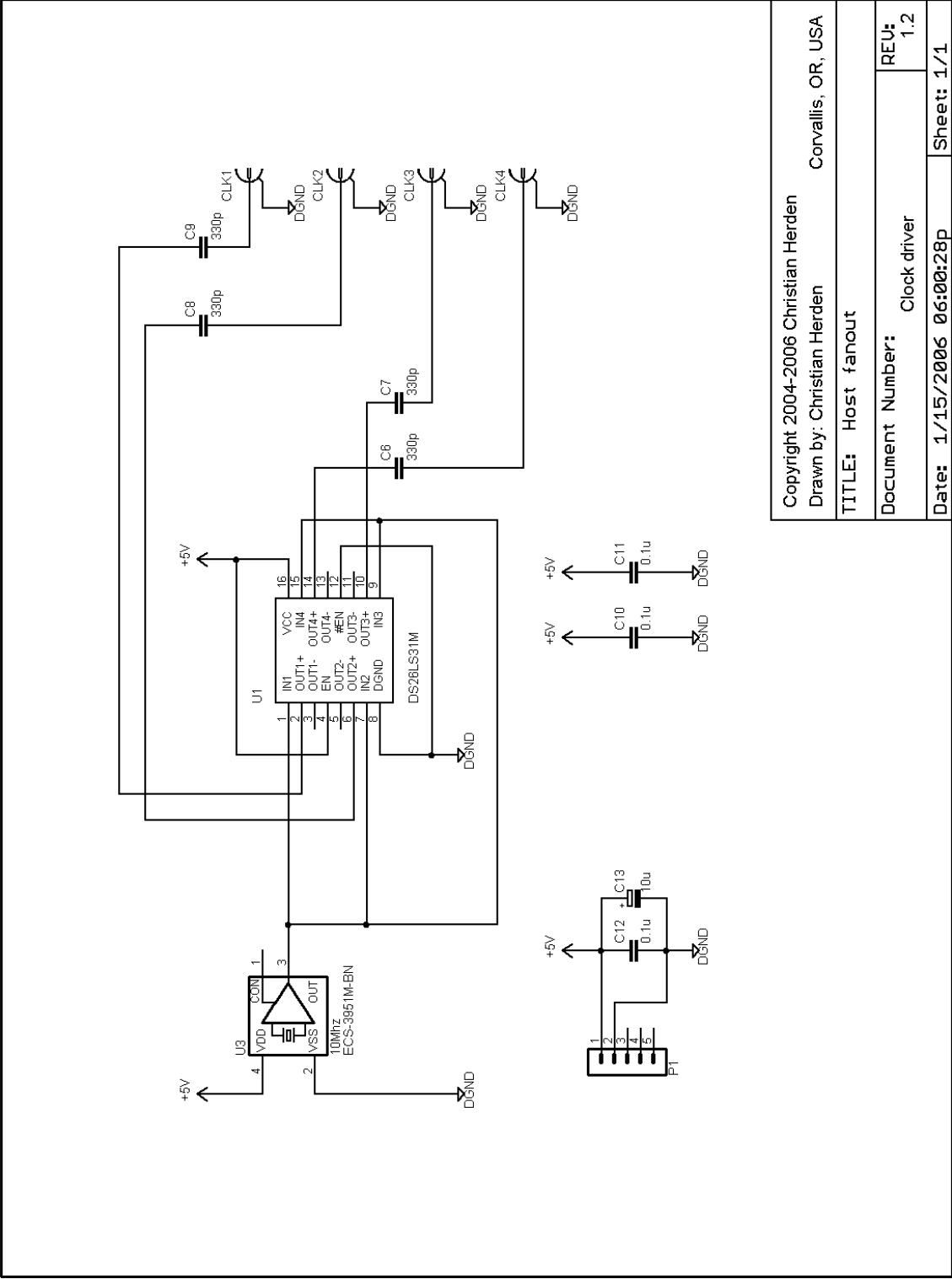
A.3.4 Reference clock module

Figure A.3.4: Schematic diagram of the Reference clock driver module. One integrated quad $100\ \Omega$ line driver converts the oscillators TTL output to a $50\ \Omega$ coaxial output.









A.4 Configuration files and Command line options

A.4.1 Pacslave

Usage: *pacslave* [*options*]

Options:

- a<n> 1 = anode, 0 = dynode
 PMT output polarity: 1 negative (anode signal)
 0 positive (dynode signal)
 Default is -a1
- b<n> 1 = Bind to socket, 0 = No socket
 Open TCP socket for network communication
 Default is -b1
- c<n> Number of channels participating in measurement
 Default is -c1234 all channels
 Example: -c24 only channels 2 and 4
- cfd Engage constant fraction discriminator
- d<n> Delay time of trigger in units of [s]
 Trigger point is shifted before or after signal crossing threshold
 Default is -d-20e-9 (= -20 ns)
- e<n> Down scaler for energy integral
 Default is -e4
 Example: -e5 would divide energy integral by a factor of 5
- f <lowerstart> <upperstart> <lowerstop> <upperstop>
 Energy windows thresholds
 Only save events with energies within lower and upper limits
 for start and stop
 Default is -f 0 8191 0 8191
- h Print this help
- i<n> Sample interval in units of [s]
 Default is -i1e-9 (= 1 ns sample interval)
- k<n> Set chi square value for sync pulse analysis
 Default is -k200

-n<n>	1 = good sync detection, 0 = save always Save waveforms and segments only if good sync was detected Default is -n1
-o<n>	Base line offset in [Volts] Default is -o0.09 (90mV)
-p<n>	Set process priority (see man process for details)
-r	Record a single sequence at once without binding to TCP socket and exit immediately
-s<n>	Number of samples per segment Default is -s1000
-S<n>	Number of segments per run Default is -s4000
-tl<n>	trigger level in % of full scale value Default is -tl30
-to<n>	1 = timeout when no events recorded 0 = no timeout Default is -to1
-ts<n>	1 = negative, 0 = positive Trigger slope Default is -ts1
-tw<n>	1 = trigger detected, 0 = no trigger detected Save waveforms and segments only when trigger was detected Default is -tw1
-v<n>	Full scale range in [Volts] Default is -v0.2 (200mV)
-w<n>	0 = save only segment entries after energy window check 1 = save waveform as ASCII data along with segment entries 2 = do not perform energy window check on data prior to saving b = save in binary format Default is -w0

A.4.2 Pacslave.conf

```
# pacslave config file
# Author: Christian Herden
# Date: 07 Sep 2004

# Channel number. This Slave is Ch 1.
channelNbr=1

# Relative or absolute path to data.
# This is where pacslave will store sequence files.
# Do not attach '/' to this path.
segPath=/home/data/<project name>

# Name attachment of energy histogram file.
outBinArray=energy.dat

# Reference file for identification of sync pulse.
syncPulse=./syncpulse.dat

# Default number of segments
nbrSegments=8000

# Default number of samples
nbrSamples=400

# Allow host IP address
hostIP=any

# Specify host port
hostPort=15000

# Bind pacslave program to the host.
# This options does not execute any measurement
# unless the host connects.
bindToSocket=1

# Anode or dynode signal of PMT
anodeSignal=1

# Default trigger slope: 1 negative, 0 positive
trigSlope=1
```

```
# Full scale in V: 256 bit resolution over a default of 200mV
fullScale=0.2

# Vertical offset +90mV
vertOffset=0.09

# Trigger level in % of full scale (25)
# trigLevel=26
trigLevel=25

# Energy scaler
energyScale=4

# Input coupling: 3 500hm DC, 1 1M0hm DC
inputCoupling=3

# trigger delay time in seconds
delayTime=-20e-9

# Energy window limitations are applied prior
# to storage
startWindowLower=0
startWindowUpper=8191
stopWindowLower=0
stopWindowUpper=8191

# CFD delay time in ns
cfdDelay=5
```

A.4.3 Pachost

Usage: *pachost* <firstsequence> <lastsequence> [*nsequence*] [*options*]
 or: *pachost* <command>

<firstsequence> Sequence number to start measurement with.
 <lastsequence> Sequence number to end measurement with.
 <nsequence> Number of sequences to record.
 Overwrites <lastsequence> with <firstsequence> + <nsequence>

Options to configure pacslave over a TCP/IP connection:

-e<n> Down scaler for energy integral
 Default is -e4
 Example: -e5 divides energy integral by a factor of 5

-n<n> 1 = good sync detection, 0 = save always
 Save waveforms and segments only if good sync was detected
 Default is -n1

-s<n> Number of samples per segment
 Default is -s1000

-S<n> Number of segments per run
 Default is -s4000

-tw<n> 1 = trigger detected, 0 = no trigger detected
 Save waveforms and segments only when trigger was detected
 Default is -tw1

-w<n> 0 = save only segment entries after energy window check
 1 = save waveform as ASCII data along with segment entries
 2 = do not perform energy window check on data prior to saving
 Default is -w0

-wb Save in binary format

-ws Save sync pulse after recording sequence

Measurement options:

-c<n>

- Number of channels participating in measurement
Default is -c1234 all channels
Example: -c24 only channels 2 and 4
- h Print this help
- k<n> 0 = do not send acquisition termination signal
 1 = send acquisition termination signal
 Default is -k0
- p<n> Set process priority (see man process for details)
- q Quiet mode
- tm Test mode will create pulses every 2 us to
 test performance of spectrometer

Commands:

- ct Create single sync pulse
 Triggers /STROBE signal
- cc Create sync pulse continuously
- cs Switch channel to SYNC
 Deasserts CHANNEL_SELECT
- cp Switch channel to PMT
 Asserts CHANNEL_SELECT

A.4.4 Pachost.conf

```
# pachost config file
# Author: Christian Herden
# Date: 07 Sep 2004

# IP addresses for computers for each PAC channel
ip1=192.168.1.1
ip2=192.168.1.2
ip3=192.168.1.3
ip4=192.168.1.4

# Port to open on PAC channel
hostPort=15000

# Number of PMT channels
nbrChannels=4

# Energy downscale factor
energyScale=2

# Destination project path
projectPath=data/2007.10.17-dummymessung

# Number of default segments per sequence
nbrSegments=8000

# Number of default samples per segment
nbrSamples=400

# Number of default starting sequence
startSequence=1

# Number of default ending sequence
endSequence=200000

# Name of pacmod device name
parportDevice=/dev/pac1
```

A.4.5 Cocheck

Usage: *cocheck* <firstsequence> <lastsequence> [*options*]

<firstsequence> Sequence number to start coincidence check with.
 <lastsequence> Sequence number to end coincidence check with.

Options:

- <n> <lowerstart> <upperstart> <lowerstop> <upperstop>
 Specifies energy windows for channel *n*.
 Default is -*n* 0 8191 0 8191 (Open Window Mode).
- C<configFile>
 Path to config file.
- c<n> Channels participating in coincidence check.
 Default is -c1234 (all 4 channels).
 Example -c24 (only channel 2 and 4).
- d<n> 1 = dump found coincidences into CIJ.DAT files.
 This option sorts coincidences in Open Window Mode and
 discards all events that are dispensible.
 Default is -d0.
- f<n> 1 = Fast search algorithm (Advanced analysis)
 0 = Slow search algorithm (Considered obsolete)
 Default is -f1.
- j<n> Force jitter in units of ps to be added to timestamp.
 Default is -j80.
- l<n> 1 = Start coincidence search on top of DIJ.DAT content.
 0 = Start coincidence search with empty bin arrays.
 This options loads DIJ.DAT content into bin arrays
 upon start up if selected.
 Default is -l1.
- o <l> <u>
 Specific lower <l> and upper <u> energy window limits
 for all channels at once.

- p<prjName>
Specify project name path to perform coincidence search on.
- r<n>
rest for <n> s if sequence file was not created yet.
Default is -r0 (no resting).
- s<n>
Evaluate only segments larger than <n> in *.SEQ file.
Default is -s1.
- S<n>
Evaluate only segments lower than <n> in *.SEQ file.
Default is -S8000.
- v<n>
0 = quiet mode.
1 = default mode with some messages.
2 = debug message mode.

Switches:

- cij
Reconstruction of dump files CIJ.DAT into DIJ.DAT files.
If this switch is set then operation of cocheck alters
from its normal behaviour. No sequence files are processed,
only dump files are being read in.
- cfd
Regard constant fraction discriminator result in timestamp.
Normal behaviour is not to add the CFD result to the timestamp.
- h
Print this help.
- O
force Open Window Mode on all channels.
- rm
remove *.SEQ files after coincidence search has been performed
on them.
- wb
Save in binary mode.

A.4.6 Cocheck.conf

```
# Path to data folder on Slaves.
# Usually this path information is preceded by
# /mnt/pacX (mount point of data folders)
projectPath=data/<project name>

# Energy windows
energyWindow1=1000 2927 2928 4500
energyWindow2=1000 2731 2732 4000
energyWindow3=1000 2574 2575 4000
energyWindow4=500 2600 4000 6000

# Time scaling factor in [ps].
timeScale=10

# t zero correction factor in [ps].
# Add to the timestamp of each Channel to account
# for signal propagation times.
tofCorrect1=0
tofCorrect2=0
tofCorrect3=0
tofCorrect4=0

# Artificial jitter to smoothen timestamp
# 1 = no jitter
# >1 = randomized integer is added to timestamp in units of [ps].
jitter=1

# Solid angle fraction
# Based on detector distance from sample d = 5 cm
# and scintillator crystal diameter of sc = 1.5 "
#solidAngleFraction=0.036
detectorDistance=0.05
crystalDiameter=0.0381

# Save time spectra only within this boundaries
# l=0 & r=7999 saves all
leftIndex=0
rightIndex=7999
```


References

- [1] J. D. Jackson, *Classical Electrodynamics*, (New York-London-Sydney-Toronto, 1962).
- [2] H. Frauenfelder, and R. M. Steffen, “Angular Distribution of Nuclear Radiations”, *Alpha, Beta, and Gamma-Ray Spectroscopy*, Volume **2**, (ed. K. Siegbahn, North Holland, Amsterdam, 1965) 997–1198.
- [3] G. Schatz, and A. Weidinger, *Nukleare Festkörperphysik*, (Teubner Studienbücher, Physik, Stuttgart, 1997).
- [4] K. S. Krane, *Los Alamos Scientific Laboratory Report*, (LA-4677, 1971).
- [5] A. J. Ferguson, *Angular Correlation Methods in Gamma-Ray Spectroscopy*, (Amsterdam, 1965).
- [6] H. C. Brinkmann, *Quantenmechanik der Multipolstrahlung*, (Noordhoff International Pub, 1965).
- [7] R. R. Kinsey et al., “The NUDAT/PCNUDAT Program for Nuclear Data”, *9th International Symposium of Capture-Gamma-Ray Spectroscopy and Related Topics*, (Budapest, Hungary, October 1996).
- [8] N. J. Stone, “Table of Nuclear Magnetic Dipole and Electric Quadrupole Moments”, *Atomic Data and Nuclear Data Tables* **90**(1) (2005) 75–176.
- [9] A. Messiah, *Quantum Mechanics*, Volume **1**, (North Holland Publishing Company, Amsterdam, 1961).
- [10] H. Fischer, and H. Kaul, *Mathematik für Physiker*, Band **1** (Teubner Studienbücher Mathematik).
- [11] McGraw, Hill, *Dictionary of Scientific and Technical Terms*, (McGraw-Hill Companies, Inc. 1974–2003, answers.com, 2003).
- [12] Wikipedia, *The Free Encyclopedia*, (www.wikipedia.org, 2003).
- [13] E. Matthias, W. Schneider, and R. M. Steffen, “Nuclear Level Splitting Caused by a Combined Electric Quadrupole and Magnetic Dipole Interaction”, *Phys. Rev.* **125** (1962) 261–268.
- [14] A. R. Edmonds, *Angular Momentum in Quantum Mechanics*, Chapter **3** and **6**, and tables, (Princeton University Press 1957) 125–132.
- [15] J. Lu, *Stochastic Models of Perturbed Angular Correlation due to Diffusion of Defects in Materials*, (PhD thesis, Brigham Young University, June 1995).
- [16] H. Jäger, J. A. Gardner, J. C. Haygarth, and R. L. Rasera, “Structural Characterization of High-Temperature Zirconia Ceramics by Perturbed Angular Correlation Spectroscopy”, *J. Am. Ceram. Soc.* **69** (1986) 458–463

-
- [17] H. Jäger, J. A. Gardner, H. T. Su, and R. L. Rasera, “Microcomputer-controlled perturbed angular correlation spectrometer”, *Rev. Sci. Instrum.* **58**(9) (1987) 1694–1698.
- [18] G. S. Collins (1981), unpublished, in ref [19], p. 172.
- [19] H. T. Su, *Perturbed Angular Correlation Spectroscopy of Oxide Ceramics at High Temperatures*, (PhD thesis, Oregon State University, 1990) 25ff
- [20] A. Böhm, *Measuring γ -ray emission time differences using direct photomultiplier tube transient recordings*, (Master thesis, Oregon State University, Fachhochschule Ravensburg Weingarten, 1997).
- [21] E. Metin, *Characterization and fitting of BaF_2 scintillator detector transients observed during γ -ray detection*, (Master thesis, Oregon State University, Fachhochschule Ravensburg Weingarten, 1997).
- [22] Acqiris, *Digitizers User Manual*, ZM020010C Rev. **B**, (Switzerland, Geneva) 2–4.
- [23] Analog Devices, “AD8180/AD8182 Switching Multiplexers”, *Datasheet*, Rev. **B**, (Norwood, MA, U.S.A.).
- [24] ECS, Inc. International, “3951M Series Clock Oscillators”, *Datasheet*, (Ridgeview, KS, U.S.A.).
- [25] National Semiconductors, “DS26LS31”, *Datasheet*, (Ridgeview, KS, U.S.A.).
- [26] Hamamatsu Photonics, “R2059”, *Datasheet*, (Hamamatsu City, Japan).
- [27] Ortec, “566 TAC”, *Datasheet*, (Oak Ridge, TN, USA).
- [28] Canberra Industries, “2145 TAC”, *Datasheet*, (Meriden, CT, USA).
- [29] J. Axelson, *Parallel Port Complete*, (Lakeview Research, 2000).
- [30] P. J. Salzman, *The Linux Kernel Module Programming Guide*, (Linux Documentation Project, www.tldp.org, 2001).
- [31] Linux Kernel Drivers, (The Linux Kernel Archives, www.kernel.org).
- [32] L. Bergmann, C. Schäfer, and H. Niedrig, *Lehrbuch der Experimentalphysik, Optik* **3** (deGruyter, 1993–2004).
- [33] S. Unterricker, M. Dietrich, G. Böhm, L. Pasemann, A. Möller, R. Vianden, M. Deicher, R. Magerle, A. Burchard, and W. Pfeiffer, “Quadrupole interaction in chalcopyrite-structure semiconductors”, *Hyperfine Interactions* (C) **1** (1996) 238–241.
- [34] S. Unterricker, M. Dietrich, A. Möller, R. Vianden, M. Deicher, R. Magerle, W. Pfeiffer, G. Böhm, and L. Pasemann, “PAC-investigation of ternary semiconductors with chalcopyrite structure”, *Cryst. Res. Technol.* **31** (1996) 761–768.

- [35] S. Unterricker, T. Butz, and W. Tröger, “TDPAC investigations of the ^{111}Cd quadrupole interaction in ternary chalcopyrite semiconductors”, *Hyperfine Interactions* **62**(4) (1991) 373–377.
- [36] S. Unterricker, and F. Schneider, “The EFG lattice structure dependence of Cd on A-sites in A(II)B(IV)C(V)2-semiconductors”, *Hyperfine Interactions* **15/16** (1983) 827–830.
- [37] S. Unterricker, V. Samokhvalov, F. Schneider, M. Dietrich, and THE ISOLDE COLLABORATION, “Magnetic Hyperfine Interaction of a Cubic Defect in α -Iron”, *Hyperfine Interactions* **158**(1–4) (2005) 229–233.
- [38] A. Möller, (Doktorarbeit, TU-Bergakademie Freiberg, 1997).
- [39] R. Vianden, “Electric field gradients in metals”, *Hyperfine Interactions* **16** (1983) 1081–1120.
- [40] M. O. Zacate, *A Microscopic Study of the Interaction Between Aliovalent Dopants and Native Defects in Group IV Oxides: Indium and Cadmium in Ceria and Zirconia*, (PhD Thesis, Oregon State University, 1997).
- [41] M. O. Zacate, by correspondence with author.
- [42] R. L. Rasera, T. Butz, A. Vasquez, H. Ernst, G. K. Shenoy, B. D. Dunlap, R. C. Reno, and G. Schmidt, “Strength, symmetry and distribution of electric quadrupole interactions at ^{181}Ta impurities in hafnium-zirconium alloys”, *J. Phys. F* **8** (1978) 1579–1589.
- [43] R. Hanada, “Oxidation of iron studied by PAC and CEMS”, *Hyperfine Interactions* **120/121** (1999) 539–544.
- [44] P. Wodniecki, B. Wodniecka, A. Kulinska, K. P. Lieb, M. Neubauer, and M. Uhrmacher, “Indium solubility in iron studied with perturbed angular correlations”, *Hyperfine Interactions* **120/121** (1999) 433–437.
- [45] M. Neubauer, K. P. Lieb, P. Schaaf, and M. Uhrmacher, “Ion-beam mixing of Ag/Fe and In/Fe layers studied by hyperfine techniques”, *Phys. Rev. B* **53** (1996) 10237–10243.
- [46] M. Uhrmacher, A. Kulinska, Yu. V. Baldokhin, V. V. Tcherdyntsev, S. D. Kaloshkin, A. Maddalena, and G. Principi, “Hyperfine Study on Mechanically Alloyed Fe-Mn Systems”, *Hyperfine Interactions* **136/137** (2001) 327–332.
- [47] J. Röder, C. Herden, J. A. Gardner, and K. D. Becker, “A Fully Digital Time Differential Perturbed Angular Correlation (TDPAC) Spectrometer”, submitted to *NIMA-S-07-00089*.
- [48] J. Christiansen, *Hyperfine Interactions of Radioactive Nuclei*, (Springer Verlag Berlin Heidelberg New York Tokyo 1983) 273ff.

-
- [49] H. Haas, and D. A. Shirley, “Nuclear quadrupole interaction studies by perturbed angular correlations”, *J. Chem. Phys.* **58**(8) (1973) 3339–3355.
- [50] W. B. Pearson, *The Crystal Chemistry and Physics of Metals and Alloys*, (Wiley-Interscience, New York, 1972).
- [51] J. A. H. da Jornada, E. R. Fraga, R. P. Livi, and F. C. Zawislak, “Pressure Dependence of the Electric Field Gradient on Cd in Zn and Sn hosts”, *Hyperfine Interactions* **4** (1978) 589–593.
- [52] M. Winter, *Webelements Scholar Edition*, (University of Sheffield, www.webelements.com, 2007).
- [53] V. B. Brudanin, “PAC spectrometer for condensed matter investigation”, *Nucl. Inst. Meth. A*, **547**(2–3) (2005) 389–399.
- [54] M. A. Alves, *The Dynamics of Oxygen Vacancies in Zirconia: An Analysis of PAC Data*, (PhD thesis, Oregon State University, June 2003).

Lebenslauf

Name	Christian Heinrich Otto Herden
Geburtsdatum	04. Februar 1971
Geburtsort	Ibbenbüren, Deutschland
Eltern	Brigitte Herden, geb. Stiegemeier und Werner Herden
Staatsangehörigkeit	deutsch
Familienstand	verheiratet, zwei Kinder

Schulische Bildung

1978 – 1981	Grundschule Westerkappeln
1981 – 1987	Realschule Westerkappeln
1987 – 1990	Fachgymnasium Technik Osnabrück
Mai 1993	Allgemeine Hochschulreife

Ausbildung

1990 – 1993	Deutsche Bundespost Telekom
Mai 1993	Kommunikationselektroniker

Studium

1993 – 2000	Studium der Physik an der Universität Osnabrück
Juni 1996	Diplomvorprüfung in Physik
Januar 1999 – Dezember 1999	Diplomarbeit in der Arbeitsgruppe Krätzig, Angewandte Optik
April 2000	Diplomhauptprüfung in Physik

Arbeitsverhältnisse

August 2000 – März 2001	Wissenschaftlicher Mitarbeiter am Institut für Physikalische und Theoretische Chemie der TU Braunschweig
seit April 2001	Computer Hardware Ingenieur bei ViewPlus Technologies, Corvallis, Oregon, USA

Veröffentlichungen

D. Kip, M. Wesner, C. Herden, and V. Shandarov, “Interaction of spatial photorefractive solitons in a planar waveguide”, *Appl. Phys. B* **68** (1999) 971–974.

M. Wesner, C. Herden, D. Kip, and P. Moretti, “Photorefractive steady-state solitons up to telecommunication wavelengths in planar SBN waveguides”, *Opt. Commun.* **188** (2001) 69–76.

M. Wesner, C. Herden, and D. Kip, “Electrical fixing of waveguide channels in strontium-barium niobate crystals”, *Appl. Phys. B* **72** (2001) 733–736.

M. Wesner, C. Herden, R. Pankrath, D. Kip, and P. Moretti, “Temporal development of photorefractive solitons up to telecommunication wavelengths in SBN”, *Phys. Rev. E* **64** (2001) 36613–36617.

D. Kip, C. Herden, and M. Wesner, “All-Optical Signal Routing Using Interaction of Mutual Incoherent Spatial Solitons”, *Ferroelectrics* **274** (2002) 135–142.

C. Herden, M. Alves, K. Becker, and J. Gardner, “A new generation TDPAC spectrometer”, *Hyperfine Interactions* **159**(1-4) (2004) 379–383.

J. A. Gardner, C. H. Herden, G. Herden, C. Dreyer, G. Bulatova, J. Sullivan, and P. Sullivan, “Simultaneous Braille, Tactile Graphics, and Ink with Tiger Ink Attachment and Duxbury”, *Proceedings of the 2004 CSUN International Conference on Technology and Persons with Disabilities*, (Los Angeles, CA, March 2004).

J. A. Gardner, C. H. Herden, G. Herden, A. Neeley, C. Dreyer, H. Stowell, V. Bulatov, G. Bulatova, L. Ungier, and Y. Sun, “Viewplus EmPrint, Ink Pro, Formatter, and Designer: Seeing and Feeling is Believing!”, *Proceedings of the 2005 CSUN International Conference on Technology and Persons with Disabilities*, (Los Angeles, CA, March, 2005).

J. Röder, C. H. Herden, J. A. Gardner, and K. D. Becker, “Fully Digital Time Differential Perturbed Angular Correlation (TDPAC) Spectrometer”, submitted to *Nuclear Instruments and Methods Section A* NIMA-S-07-00089.

J. Röder, C. H. Herden, J. A. Gardner, K. D. Becker, M. Uhrmacher, and H. Hofsäss, “Actual Concepts of Digital PAC-Spectroscopy”, submitted to XIV. International Conference on Hyperfine Interactions, (Iguazu, Brazil, August 2007).

Konferenzbeiträge

C. H. Herden, M. Alves, K. D. Becker, and J. A. Gardner, “A new generation TD-PAC spectrometer”, (XIII. International Conference on Hyperfine Interactions, Bonn, Germany, 23.-27. August 2004), Poster.

J. Röder, C. H. Herden, J. A. Gardner, K. D. Becker, M. Uhrmacher, and H. Hofsäss, “Actual Concepts of Digital PAC-Spectroscopy”, (XIV. International Conference on Hyperfine Interactions, Iguazu, Brazil, August 2007), Poster.

Fortlaufende Projekte

NSF DMI-0422218 “SBIR Phase II Accessible Scalable Vector Graphic Authoring and Editing Applications”, Rolle: Beteiligter Wissenschaftler, 15. August 2004 - 31. Juli 2006, Phase IIB 1. August 2006 - 31. Juli 2008.

NIH 2R44EY015968-02 “SBIR Phase II; High Speed Tactile Graphics and Braille Embosser”, Rolle: Federführender Wissenschaftler, 1. Juni 2006- 31. Mai 2008.

Subcontract on NIH 1R21EY016799-01 “Penn State-Phase 1 - Testing Polymer Braille Display Properties”, Rolle: Teilnehmer, 1. August 2005 - 31. Juli 2007.

Abgeschlossene Projekte

NIH 2R44EY014481-01 “SBIR Phase I: The Accessible Graphics Reader for Blind People”, Rolle: Beteiligter Wissenschaftler, September 30, 2002 - March 29, 2003

NIH R43EY015968-01 “SBIR Phase I; High Speed Tactile Graphics and Braille Embosser”, Rolle: Federführender Wissenschaftler, 1. September 2004 - 28. Februar 2005.

NSF DMI-0231691 “SBIR Phase I Accessible Scalable Vector Graphic Authoring and Editing Applications”, Rolle: Beteiligt, 1. Januar 2003 - 30. September 2003.

NIH 2R44EY014481-02 “SBIR Phase II: The Accessible Graphics Reader for Blind People”, Rolle: Beteiligt, 1. Dezember 2003 - 30. November 2005.

NIH 1R43EY017238-01 “SBIR Phase I: Accessible Graphical Display for Numerical Data”, Rolle: Beteiligt, 1. April 2006 - 31. März 2007.